Master's thesis

NTNU
Norwegian University of Science and Technology
Faculty of Natural Sciences
Department of Physics

Anders Hagen Jarmund

Cerebral Hemodynamics in Normal Neonates During Tilt

Computer Modelling and Experiments

Master's thesis in Applied Physics and Mathematics
Supervisor: Rita de Sousa Dias / Hans Torp
June 2019

Photo by Frida J. Krüger

NTNU
Norwegian University of
Science and Technology

Anders Hagen Jarmund

Cerebral Hemodynamics in Normal Neonates During Tilt

Computer Modelling and Experiments

Master's thesis in Applied Physics and Mathematics
Supervisor: Rita de Sousa Dias / Hans Torp
June 2019

Norwegian University of Science and Technology
Faculty of Natural Sciences
Department of Physics

NTNU
Norwegian University of
Science and Technology

Til mine foreldre, besteforeldre og tante Ragnhild

Summary

Newborns are vulnerable to altered cerebral blood flow that in worst case terminates in brain injury and death or life-lasting disabilities. An ultrasound system named NeoDoppler has recently been invented to offer continuous surveillance of the cerebral blood flow in neonates. However, the hemodynamics of normal neonates is not yet fully understood.

In this project, a lumped multi-compartment model was developed in MATLAB to simulate cerebral blood flow in neonates during a 90° head-up tilt. Regulation of heart rate, peripheral resistance and cerebral resistance was implemented. Different combinations of the three regulatory mechanisms were simulated to assess their individual and combined effects. NeoDoppler recordings from two newborns participating in tilt experiments were used to adjust and validate the model.

The model was able to reproduce several of the features observed in the experimental recordings. The different combinations of active regulatory mechanisms yielded a variety of responses, in line with the diversity of responses reported in earlier studies. Simulations using all three regulatory mechanisms provided the best fit to the two NeoDoppler recordings. It seems that the model may be a promising point of departure for later studies, but further development and validation against experimental data are required.

Sammendrag

Nyfødte barn er sårbare for å få forstyrret blodstrømmen i hjernen. I verste fall kan forstyrrelsen føre til hjerneskader og ende med død eller livsvarige funksjonsnedsettelser. Et ultralyd-system kalt NeoDoppler har nylig blitt utviklet for å overvåke den cerebrale blodstrømmen kontinuerlig over tid. Samtidig er det slik at mye ved normale nyfødtes hemodynamikk er lite forstått.

I dette prosjektet ble det utviklet en konsentrert (eng. *lumped*) modell i MATLAB for å simulere den cerebrale blodstrømmen hos nyfødte ved $90°$ vipping med hodet oppover. Det ble implementert reguleringsmekanismer for hjertefrekvens og perifer og cerebral karmotstand. Ulike kombinasjoner av de tre reguleringsmekanismene ble brukt for å undersøke hvilken effekt de hadde alene og sammen med hverandre. NeoDoppler-opptak av to nyfødte som gjennomgikk en eksperimentell vippe-test ble brukt for å tilpasse og validere modellen.

Modellen var i stand til å gjenskape mange av trekkene som ble observert i den eksperimentelle vippe-testen. De ulike kombinasjonene av reguleringsmekanismer gav resultater som gjenspeilte noe av variasjonen i vippe-responsen funnet i tidligere studier. Overensstemmelsen med dataene fra de to nyfødte var best med alle reguleringsmekanismene aktivert. Det ser ut til at modellen kan være et lovende utgangspunkt for senere studier, men den bør utvikles videre og valideres med ytterligere eksperimentelle data.

Preface

This master thesis finishes a five year master's degree programme in applied physics and mathematics at the Department of Physics in collaboration with the Department of Circulation and Medical Imaging, both at the Norwegian University of Science and Technology (NTNU). The slogan of the programme is "Give life to the equations!" [1] and this project is an example par excellence of how equations and physical modelling can be applied to investigate some of the mysterious mechanisms making life possible. Although my work has been purely theoretical, the closeness to the clinic and its patients has been ubiquitous. Infants are, literally, those who are not able to speak [2], and yet they tell enthralling stories about adaptment, dependence and vulnerability in the face of extrauterine life, leaving us in wonder and awe. I wish to thank the clinicians Siv Steinsmo Ødegård, Siri Ann Nyrnes and Martin Leth-Olsen at St. Olavs hospital for their support and contributions, and the parents who kindly have allowed their newborns to participate in the NeoDoppler project.

I would also like to express my sincere gratitude to professor Hans Torp who has supervised this project and allowed me to work with his group. His continuous advice and feedback, support and positive attitude, throughout the semester, have been invaluable. Associate professor Rita de Sousa Dias has also supervised, and I am proud that she agreed to guide me through this project. Finally, I want to thank my research partner Thanh Q. Nguyen for interesting discussions and enjoyable company in late evenings. It has indeed been a tiresome yet pleasurable time.

Trondheim, June 2019
Anders Hagen Jarmund

Contents

List of Tables

List of Figures

List of Abbreviations and Symbols

τ	Time constant
a	Used for both radius and fractional blackflow duration
C	Compliance/capacitance
k	Steepness/sensitivity parameter
L	Inductance/inertia
q	Flow rate
R	Resistance
t_c	Duration of a cardiac cycle
t_s	Duration of systole
bpm	Beats Per Minute
bw	Birth Weight
CBF	Cerebral Blood Flow
CO	Cardiac Output
CrCP	Critical Closure Pressure
DBP	Diastolic Blood Pressure
HUT	Head-Up Til
LBNP	Lower Body Negative Pressure
LVEDV	Left Ventricle End-Diastolic Volume
LVET	Left Ventricular Ejection Time

LVO	Left Ventricular Output
MAP	Mean Arterial (Blood) Pressure
MCP	Mean Cerebral Blood Pressure
PEP	Pre-Ejection Period
PRF	Pulse Repetition Frequency
PW	Pulse-Waved
SBP	Systolic Blood Pressure
SV	Stroke Volume
TPR	Total Peripheral Resistance
US	Ultrasound

Chapter 1

Introduction

> There is no such thing as an infant. [...] whenever one finds an infant one finds maternal care, and without maternal care there would be no infant.
>
> Winnicott [3, p. 586]

1.1 Motivation

Being born is one of the most dramatic events in a human's life, and enormous adaptations are made in almost every organ as one is separated from the mother and rendered an individual [4]. But being born is also a dangerous project. Today, in Norway, 1.4 of 1000 neonates dies within the first four weeks of life, compared to 11.0 in 1967 [5]. Worldwide, 3% of living newborns dies within their first four weeks of life [6], of which 36% dies during the first day, and 73% during the first week [7]. In absolute numbers, about two less-than-a-day old neonates dies every minute. Another million develop neurodevelopmental disorders due to hypoxic brain injuries [8]. Mortality increases for lower gestational age, being over 50% at gestational age 23 weeks in Norway, and dropping to below 5% at gestational age 28–31 weeks [9].

Prematurity, severe infections and asphyxia each contribute to about a fourth of neonatal mortality [10]. A common mechanism to death and disability in these conditions is brain injury due to cerebral hypo- or hyperperfusion or hypoxia [11–14]. Detection of altered cerebral blood flow may therefore provide a route of diagnosing underlying pathology at an early stage so that suitable medical interventions can be supplied.

NeoDoppler is an ultrasound device for continuous surveillance of cerebral blood flow developed at the Department of Circulation and Medical Imaging, NTNU [15, 16]. A small ultrasound transducer is fixed to the anterior fontanelle of the infant and the blood flow velocity at various depths is recorded. Several parameters, such as short- and long-

term variations in perfusion and pulsatility, can be calculated and continuously assessed and used as an aid in deciding proper medical treatment.

Currently, the knowledge concerning neonatal cerebral autoregulation is scarce [17]. Autoregulation is a set of physiological mechanisms that seek to keep cerebral blood flow constant at a satisfying level across varying blood pressures [18]. It is likely that the autoregulatory mechanisms may be underdeveloped in some preterm infant, leaving them vulnerable to altered cerebral blood flow.

Hence, it is of significant interest to investigate normal and abnormal cerebral blood flow patterns in the infant, both in steady-state and as the autoregulation is challenged during stress. Tilting is a simple way of inducing mild hemodynamic stress. The introduction of a difference in height between heart and brain is accompanied with a hydrostatic pressure that has to be compensated. Head-up tilting has been found to elicit a range of responses in the infant, including in blood pressure [eg. 19–22], heart rate [eg. 20–23], and cerebral blood flow velocity [eg. 24]. Computer simulation has shown to be a fruitful approach to study the cardiovascular system due to its complexity and since many of the variables are challenging to inquire experimentally [25, 26].

In this project, a lumped model is developed to explore the dynamics of a 90° tilt in the neonate. Autoregulation and a simple baroreceptor reflex is implemented to study how resistance and compliance respond to the postural change. The effects of the tilt on cerebral circulation and blood pressure are of special interest. Experimental data from NeoDoppler recordings of term neonates are used to develop and validate the model.

1.2 Aim and Scope

This project is part of a larger research project on NeoDoppler at the Department of Circulation and Medical Imaging, NTNU, in which NeoDoppler recordings of tilt experiments have been collected. The focus of this project is on model development, and the experimental data will not be subjected to comprehensive analysis.

The aim of this project is to develop a lumped model that can reproduce key features of the blood circulation of a neonate, with emphasis on the cerebral circulation, and how regulatory and autoregulatory mechanisms respond to a 90° tilt. The model will be validated by experimental measurements, including NeoDoppler recordings. In addition will existing studies on neonates undergoing tilt test be reviewed.

1.3 Contributions

This project was supervised by professor Hans Torp at the Department of Circulation and Medical Imaging, NTNU, and associate professor Rita de Sousa Dias at the Department of Physics, NTNU. Important contributions have been provided from others at the Department of Circulation and Medical Imaging and St. Olav's University Hospital: Siv Steinsmo Ødegård have conducted tilt experiments as a part of an ongoing study. She has kindly provided NeoDoppler recordings and blood pressure measurements. Martin Leth-Olsen provided Doppler measurements for a premature infant from several anatomical locations. Siri Ann Nyrnes has provided knowledge and expertise regarding neonatal

physiology.

Master student Thanh Q. Nguyen has worked on a project on modelling neonatal circulation during closure of the ductus arteriosus [27]. Both this and his project have used a model by Garcia-Canadilla et al. [28] as basis and the same software for simulation, but different adaptions and modifications have been made.

Two recent master theses have addressed related topics. Tran [29] devised a lumped model to simulate cerebral bloodflow in neonates with open ductus arteriosus. A linear model was compared to a non-linear model, and validated with Doppler recordings of neonates and an experiment involving arm position in adults. Wisløff [30] used a lumped model to investigate whether pressure-dependent or pressure-independent resistance provided most accurate blood flow patterns, and compared recordings of peripheral blood flow in healthy and diabetic volunteers.

Some overlap exists among the mentioned master projects and this project, in terms of equipment used for experimental recording and simulation software, but the projects have dealt with separate subjects, utilised different data sets, and developed unique models.

1.4 Outline of the Report

This thesis is divided into five chapters followed by references and an appendix. The remaining part of the introductory chapter will provide a review of relevant literature and necessary theory. First is an overview of anatomy related to the project and unique features of the neonate. Thereafter follows a brief description of the cardiovascular system, including some cardiac physiology and blood pressure regulation. The section finishes with an account of the tilt test and how newborns have been found to respond to tilt in earlier studies. The next section introduces basic principles for ultrasound and the NeoDoppler technology utilised to acquire the experimental data used in this project. The last section derives how an electrical circuit can be used to model blood circulation.

Next is Chapter 2 on methods, which first describes the acquisition of experimental data, then the development of a model for steady-state circulation, and lastly how the steady-state model was elaborated to simulate a tilt experiment. Results are presented in Chapter 3, organised in three sections corresponding to the method chapter, and discussed in Chapter 4 alongside limitations of the model and suggested improvements.

Finally, Chapter 5 offers concluding remarks. The appendix houses source code for the regulation of resistance and the generation of input signal to the model, and some additional results.

> Keep your heart with all diligence,
> for out of it is the wellspring of life.
>
> Proverbs 4:23 [31]

1.5 The Neonate

The first half of this section provides an overview of selected topics of neonatal anatomy and physiology that are important for this project. The latter part of this section offers a review of circulatory (auto-)regulation and the tilt test. Selected studies are presented that shed some light on the neonate's response to tilt.

1.5.1 Anatomy and Physiology

Anatomy

Oxygenated blood is ejected from the left ventricle (*ventriculus sinister*) through the aortic valve (*valva aortae*), into the ascending aorta (*aorta ascendens*) [32]. A small amount enters the coronary arteries (*aa. coronariae*), providing blood to the heart itself. Most of the blood follows *aorta ascendens* which bends and becomes the aortic arch (*arcus aortae*). Three arteries leave the aortic arch; first the brachiocephalic trunk (*truncus brachiocephalicus*), then the left common carotid artery (*a. carotis communis sinistra*), and finally the left subclavian artery (*a. subclavia sinistra*. The aortic arch itself bends downwards, becoming the descending aorta (*aorta descendens*), providing blood to the lower part of the body, which is of less interest in this project. The brachiocephalic trunk divides into the right subclavian artery (*a. subclavia dextra*) and the right common carotid artery (*a. carotis communis dextra*). The subclavian arteries supply blood to the upper extremities, as seen in Figure 1.1a, where the left-right-asymmetry can also be spotted. Figure 1.1b shows how the right common carotid artery ascends towards the head and splits into an external (*a. carotis externa*) and an internal part (*a. carotis interna*). The point of division is the bifurcation (*bifurcatio caroditis*), which houses the carotid body (*glomus caroticum*) which consists of neural cells detecting pH and hypoxia. The carotid artery widens around the bifurcation (*sinus caroticus*), and the vessel wall contains pressure sensors (baroreceptors). The left common carotid artery follows the same course.

The brain receives most of its blood from the internal carotid arteries, although some blood is also provided through the vertebral arteries (*aa. vertebrales*) that arise from the subclavian arteries as illustrated in Figure 1.1b. The two vertebral arteries join at the pons and create the basilar artery (*a. basilaris*) as seen in Figure 1.1c, which supplies blood to the cerebellum and pons, and also the posterior portions of the brain as the posterior cerebral arteries (*a. cerebri posterior*). The internal carotid arteries enter the skull through *canalis caroticus* and later become the medial cerebral arteries (*a. cerebri media*). Figure 1.1c also shows how an anastomosis named the Circle of Willis (*circulus arteriosus cerebri*) connects the carotid and vertebrobasilar blood flow. The anterior cerebral artery arises from this circle and provide blood to the anterior parts of the brain, as demonstrated in Figure 1.1d. Both the anterior and the medial cerebral artery receive their blood from the internal carotid artery.

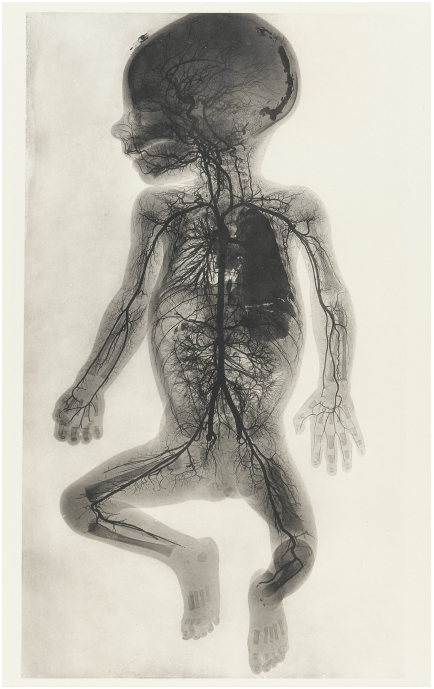

(a) The arterial system of a 9 month old foetus.

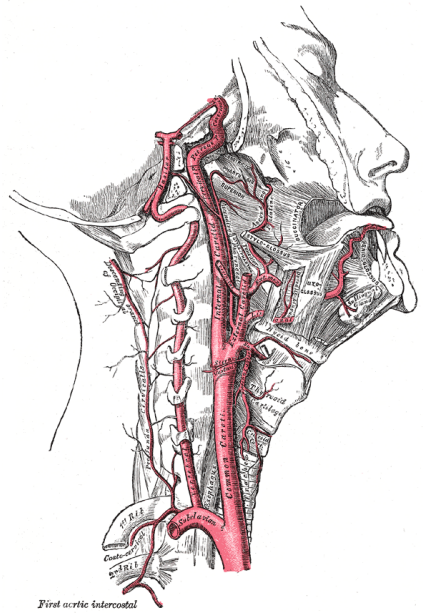

(b) Overview of the arteries of the neck.

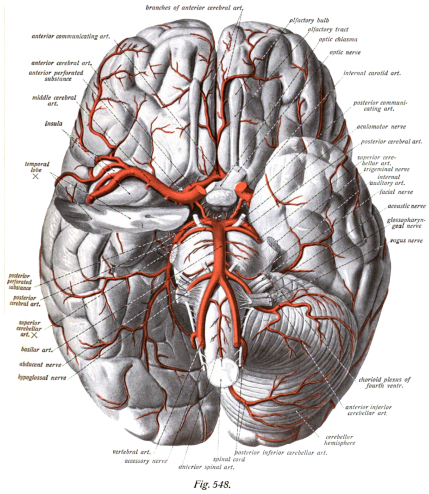

(c) Caudal view of cerebral arteries.

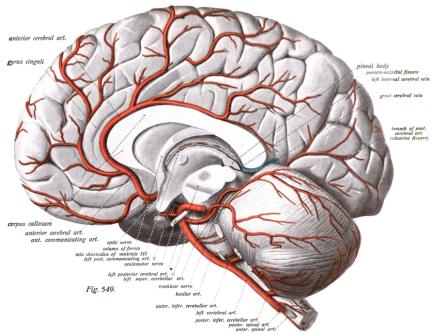

(d) Lateral view of cerebral arteries.

Figure 1.1: The brain receives its blood from the internal carotid arteries and the basilar artery. The arteries' path can be tracked down to their origin from the aorta. All the images are released to the public domain, **(a)** after Römmler, Leopold and Leisewitz [33], **(b)** after Carter, Gray and Book [34], and **(c, d)** after Sobotta [35, 36].

The Circle of Willis is subject to considerable anatomical variation in the population, with some variants shown in Figure 1.2. Absent or hypoplastic parts of the circle may render the individual vulnerable to disease. It has been found that complete circles are more frequent in preterm than in term infants, leaving the compelling possibility that stressed or endangered foetuses utilise the circle, through mechanisms still unknown, as a strategy to reduce the risk of cerebral damage [37].

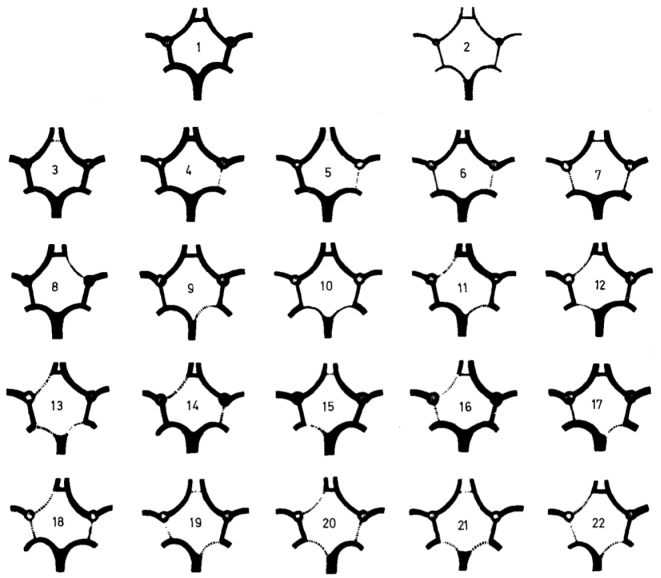

Figure 1.2: Several variations of the Circle of Willis (*circulus arteriosus cerebri*) are found in the population. Types 1, 3 and 6 are most frequent [38]. The Circle of Willis is also displayed in Figure 1.1c representing type 1 (one communicating artery is hidden behind the optic nerve). The single incoming vessel at the bottom of Type 1 is the basilar artery that divides into the left and right posterior cerebral artery. Communicating arteris connect these to the left and right internal carotid artery that becomes the middle cerebral artery. A branch emerges from the left and right internal carotid artery that sling forward and is named the anterior cerebral artery. The right and left anterior cerebral artery is joined in Type 1 by a communicating artery. Figure by Lazorthes et al. [38], reprinted with permission from Springer Nature.

The brain is enclosed in three membranes (*meninges*); the outer *dura mater*, then the *arachnoidea mater*, and finally the inner *pia mater* [32]. The cerebral arteries are confined to the subarachnoid space, i.e. external to the *pia mater*.

Unique anatomical features of the neonate

The foetus receives oxygenated blood from the placenta whereas after birth gaseous exchange will happen in the lungs [39, Ch. 16]. Two main differences are found between the circulation in adults and foetuses,

- the left and right ventricles of the foetus pump in parallel, not in series,

- the foetus has three shunts leading blood from the pulmonary circulation to the placental circulation.

The three shunts are shown in Figure 1.3. These are reviewed as they often remain open for some time after birth.

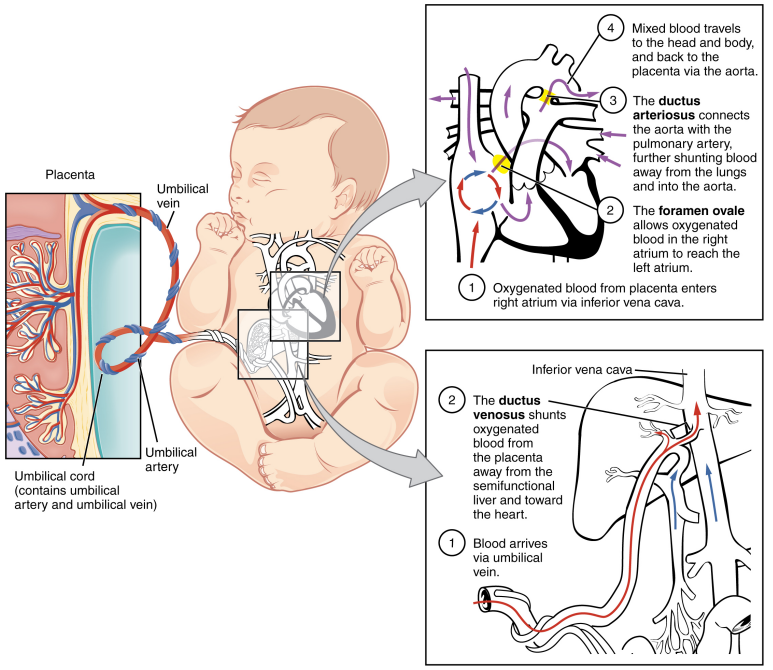

Figure 1.3: The foetus receives oxygenated blood from the placenta, and uses three shunts to distribute the blood efficiently. The image is made by OpenStax College [40] and is licensed under CC BY 3.0.

The first shunt, *ductus venosus*, carries oxygenated blood from the placenta directly into the *vena cava inferior*, bypassing the liver. Kiserud, Rasmussen and Skulstad [41] found that only 20–30% of the blood is shunted whereas the rest is directed to the fetal liver. Ductus venosus loses its function as the umbilical chord is clamped [39, Ch. 16]. It is usually closed within three months of birth.

The second shunt is the *foramen ovale*, connecting the right and left atria of the heart [39, Ch. 16]. As the pulmonal resistance is high prior to birth, most of the blood is shunted from the right atrium to the left atrium. At birth, when umbilical inflow ceases and pulmonary resistance drops, the pressure in the right ventricle drops and the pressure in the left atrium rises, so that blood is no longer shunted. A flap prevents blood flow from the left atrium to the right atrium. The foramen ovale disappears slowly, and remains in about 10% of the adult population.

The final shunt is the *ductus arteriosus*, a channel bridging the pulmonary artery to the aorta [39, Ch. 16]. The direction of flow through the ductus arteriosus is determined by the pressure difference. *In utero*, the pulmonary resistance is high, shunting blood from

the pulmonary artery into the aorta (right-to-left shunting). After birth, the flow direction is usually reversed as the systemic resistance exceeds the pulmonary resistance. In term neonates, ductus arteriosus usually closes spontaneously about 27 hours after birth in boys and 45 hours after birth in girls [42]. Cesarean delivery seems to delay the closure in both sexes.

A patent ductus arteriosus may be problematic, especially in preterm infants [43, Ch. 10]. Apnoea and bradychardia can occur as well as hypoxia, increased pulse pressure, audible systolic murmur, prominent precordial impulse, and, in severe cases, heart failure.

Vasculature

Blood vessels are divided into arteries, arterioles, capillaries, venules and veins depending on their size and structure [44, Ch. 19]. Some structural differences and physiological properties are highlighted in Figure 1.4. All vessels have three layered walls; the intima, the media, and the adventitia; except the capillaries that only have the intima layer. The arteries can be divided into elastic and muscular arteries. The latter have walls with several layers of smooth muscles, making them resistant to increasing pressures so that their diameter does not change significantly. Elastic arteries, such as the aorta, have less smooth muscles and are more compliant.

The arterioles contribute most to systemic resistance, and the pressure drop is greatest here. The vessel walls contain smooth muscles permitting vasodilatation and -constriction. Although the capillaries have higher individual resistance, the number of capillaries in parallel lowers their contribution (see section 1.7.2 and Figure 1.4b) as the total cross-sectional area increases. The capillaries lack smooth muscle cells, and are often leaky so that nutrition, oxygen and other substances can extravasate into the tissue.

The venules and veins are thin walled, elastic vessels that can act as blood reservoirs. The venous blood pressure is very low, as shown in Figure 1.4b, and the flow is mainly driven by gravity or the contraction of surrounding muscles. Back-flow is prevented by valves. Often the veins are located close to pulsating arteries so that some motion is transferred.

The Heart

The heart (*cor*) acts as the pump of the circulatory system. The cardiac cycle is commonly divided into four phases, as demonstrated in Figure 1.5; isovolumic contraction, ejection, isovolumic relaxation, and filling phase (divided into several stages in the figure). The cycle starts in systole as all the valves are closed, the ventricles are filled with blood and start contracting (isovolumic contraction) [47, p. 190]. When the ventricular pressure exceeds the aortic and pulmonary pressure, the aortic and pulmonary valves (the semilunar valves) opens and blood is ejected into the aorta and pulmonary artery (ejection phase). The ejection becomes gradually slower, and towards the end of the ejection phase a small retrograde flow is observed, and the ventricular pressures have dropped below the pressure in the corresponding arteries. Due to inertia, the semilunar valves are not closed immediately as the pressure gradient changes [44, Ch. 22]. The diastole begins as all valves again are closed, but the ventricles no longer filled with blood [47, p. 190]. The ventricles relax and the ventricular pressure continues to fall (isovolumic relaxation). A small increase in

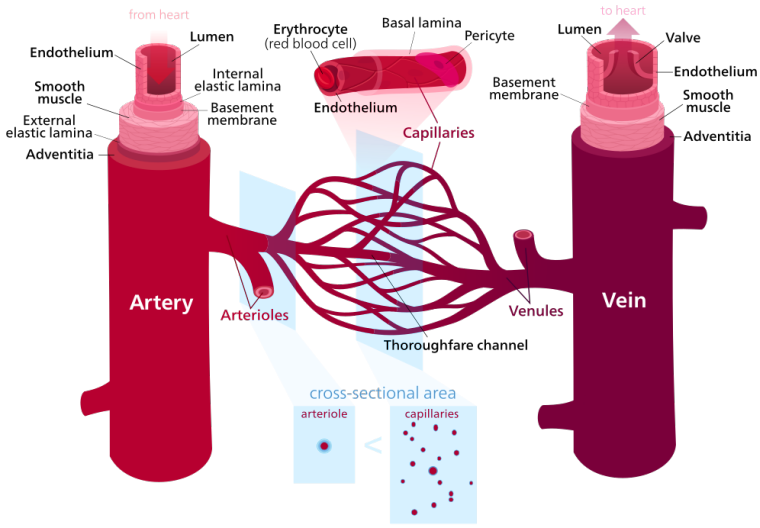

(a) Image by Kelvinsong [45], licensed under CC BY-SA 3.0.

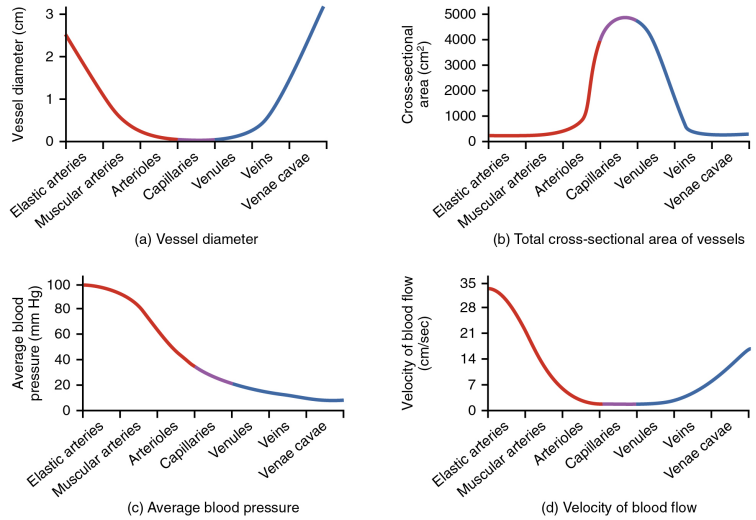

(b) Image by Rice University [46], licensed under CC BY 4.0.

Figure 1.4: Blood vessels are categorised into arteries, arterioles, capillaries, venules, and veins. The different vessels have specific properties.

aortic pressure is seen as the aortic valve closes, creating a small peak termed the dicrotic notch or incisura as shown in Figure 1.5 [44, Ch. 22]. It is also argued that pressure wave reflections may be involved in the creationof the dicrotic notch [48]. The atria were filled with blood during ejection, as the valve plane was lowered, creating a suction effect [47, p. 190]. When the ventricular pressures become lower than the atrial, the mitral and tricuspid

valves opens and the ventricles are filled with blood (filling phase). The filling is mostly passive, with the ventricles filled 80% in the first quarter of diastole, followed by a slower filling (diastasis). Normally, the atria contract to fill the ventricles maximally, a subphase referred to as atrial systole.

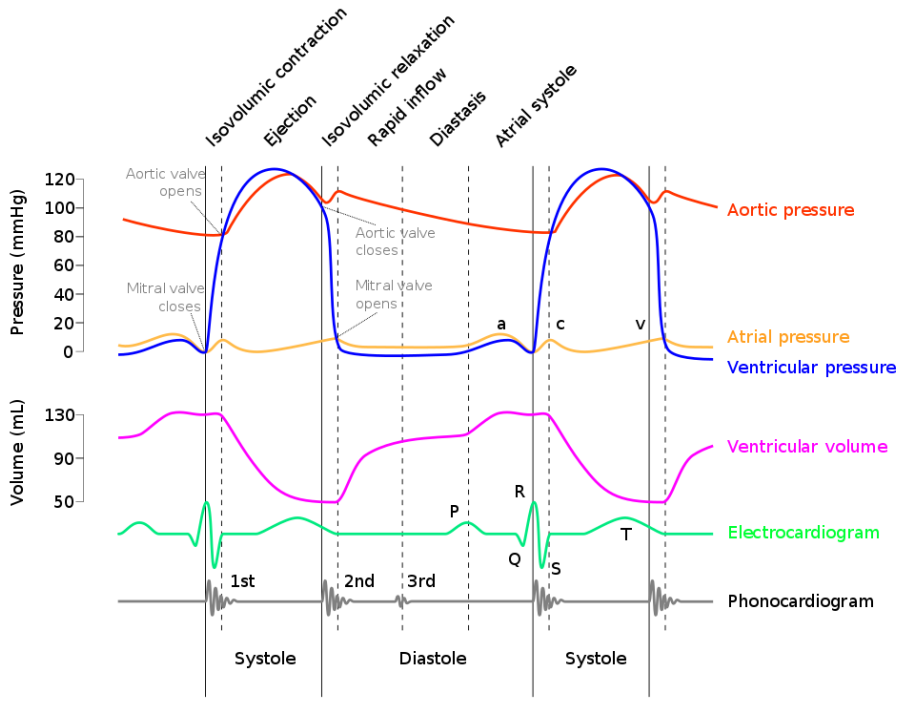

Figure 1.5: A Wiggers diagram showing the important events during a cardiac cycle. Details in the text. Image by xavax, adh30 and DanielChangMD [49], licensed under CC BY-SA 3.0.

In the clinic, the heart phases are identified and assessed using auscultation with a stethoscope or electrocardiogram (ECG). Figure 1.5 show how the ECG and heart sounds relate to the cardiac cycle, but details regarding these are beyond the scope of this texts [see eg. 44, Ch. 21–22]. Doppler US can be used to qualitatively and quantitatively evaluate flow patterns during the the different phases.

Cardiac output (CO) describes how much blood that is ejected from either the left or the right ventricle per minute. In the neonate, left and right cardiac output may not be equal, and as the pulmonary circulation is not considered in this project, CO will refer to the output from the left ventricle (LVO). Similarly, stroke volume (SV) will denote the volume of blood ejected from the left ventricle per cardiac cycle. The relation between CO and SV is

$$\mathrm{CO} = \mathrm{HR} \cdot \mathrm{SV}, \tag{1.1}$$

where HR is heart rate in beats per minute (bpm). Hudson et al. [50] measured CO in 20 healthy, 2–7 days old neonates (gestational age 37–41 weeks, weight 2380–4020 g),

and found a normal range 154–308 $\mathrm{mL\,kg^{-1}\,min^{-1}}$ with mean 231 $\mathrm{mL\,kg^{-1}\,min^{-1}}$, in concordance with both earlier [eg. 51] and later estimates [eg. 52]. To assess SV, Walther, Siassi and Wu [53] used Doppler US on 112 healthy neonates (gestational age 27–42 weeks, weight 780–5350 g) and found SV to be 1.77 $\mathrm{mL\,kg^{-1}}$ (SD 0.28 $\mathrm{mL\,kg^{-1}}$). Heart rate in the neonate is typically 110–145 bpm (median 127 bpm) [54], compared to 60–80 in adults [47, p. 190].

Historically one has thought that the regulation of CO in the neonate was dominated by heart rate, whereas SV was kept fixed. Newer studies have nuanced this position [55]. For example, Gullberg, Winberg and Selldén [56] found that neonates were able to change CO by at least 15% due to change in SV. As heart rate increases, less time is available for filling, and end-diatolic volume decreases [44, Ch. 23]. On the other hand, increased heart rate also increases contractility and thereby reducing the end-systolic volume. As SV is the difference between end-diastolic and end-systolic volume, the total effect on SV is not readily predictable. Kenny et al. [57] studied cardiac functioning in human foetuses, and found that SV declined with heart rate (HR) as SV $[\mathrm{mL}] = 7.11 - 0.02 \cdot \text{HR [bpm]}$. If one assumes this relationship holds true across birth, an estimate for the newborn is

$$\text{SV } [\mathrm{mL}] = \frac{-0.02 \cdot \text{HR [bpm]} + 7.11}{-0.02 \cdot 120 + 7.11} \cdot 1.77 \cdot \text{bw } [\mathrm{kg}], \tag{1.2}$$

where bw is birth weight, yielding a CO of 220 $\mathrm{mL\,kg^{-1}\,min^{-1}}$ at heart rate 130 bpm, well within the reported normal range [50–52]. In Eq. (1.2), SV has been set to equal the typical value 1.77 $\mathrm{mL\,kg^{-1}}$ at heart rate 120 bpm [53].

The duration of a cardiac cycle t_c is the inverse of heart rate and can be divided into a systolic, t_s, and diastolic, t_d, period, as described above. t_c decreases as heart rate increases, mainly due to a decrease in t_d [47, p. 190]. Technically, the systolic duration is composed of a left ventricle ejection time and a short pre-ejection period (PEP) representing a delay from ventricular depolarisation until the ventricular ejection begins [58]. Lindner et al. [59] found left ventricular ejection time (LVET) to be approximately

$$\text{LVET } [\mathrm{ms}] = 286 - 0.80 \cdot \text{HR [bpm]}$$

for neonates 24–30 hours after birth. In terms of flow rates, the PEP can be ignored as the aortic valve is still closed, and the duration of systole can be expressed as a fraction of the duration of the total cardiac cycle,

$$\frac{t_s}{t_c}[\%] = \frac{48 \cdot \text{HR} - 0.133 \cdot \text{HR}^2}{100}. \tag{1.3}$$

Although the LVET depends on age, the variation in t_s/t_c the first month is negligible for a given heart rate [58]. t_s/t_c for different ages is shown in Figure 1.6. Others have studied older children finding similar results [60], whereas some find the average systole-to-diastole ratio to surpass 1.0 after a few months of age [61].

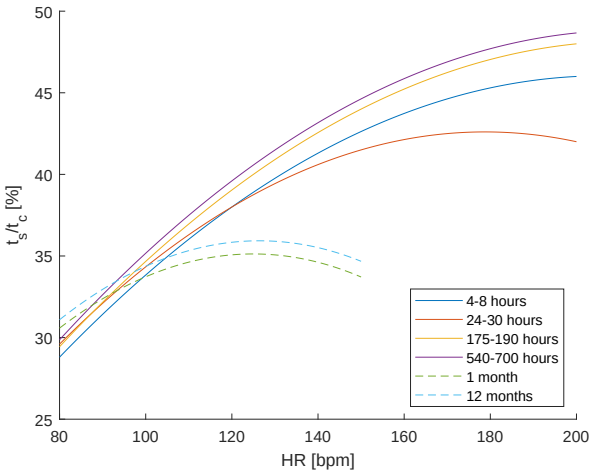

Figure 1.6: Length of systole (t_s when PEP is ignored) relative to the total cardiac cycle t_c at different ages. Hassan and Turner [58] (—) studied newborns, whereas Golde David and Burstin Luis [60] (- - -) studied children up to 13 years of age and with lower mean heart rate (thus plotted with a shorter range).

1.5.2 Blood Pressure Regulation and Autoregulation

The blood pressure varies throughout the day as one moves or changes position. The tissues, however, need reliable supply of nutrition and oxygen, and the possibility to remove waste and toxic products. Neural tissue is especially vulnerable to failing perfusion as it is highly oxygen-dependent, in charge of 20% of the body's total oxygen consumption, despite constituting only 2% of the body weight (in adults) [62, Ch. 23]. Hypotension can cause global cerebral ischemia. The body has evolved a range of mechanisms to counteract deviations in blood pressure and ensure perfusion within a satisfactory range. Both hypo- and hyperperfusion can be detrimental to the neonate through a range of mechanisms [18]. Figure 1.7 shows how different mechanisms interact to stabilise blood pressure after a postural change, such as standing up from a sitting position.

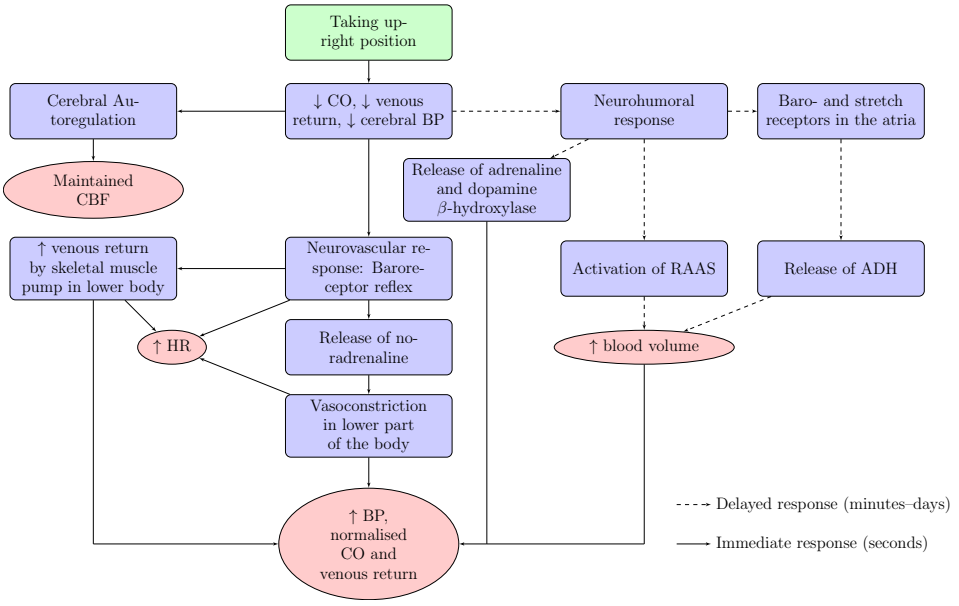

Figure 1.7: Schematic representation of mechanisms evoked by changing from supine to upright position. Abbreviations: HR, heart rate; CO, cardiac output; CBF, cerebral blood flow; RAAS, renin–angiotensin–aldosterone system; ADH, Antidiuretic hormone (vasopressin). Inspired by Perlmuter et al. [63].

In the neonate, the brain receives about 17% of CO, and accounts for about 17% of the body weight [18]. Cerebral autoregulation in humans becomes increasingly more functional from week 23 to 33 of gestation, but pressure reactivity and autoregulation in response to systolic blood pressure and MAP is not observed prior to week 26–28. Preterm neonates are thus extremely vulnerable to disturbed cerebral blood flow.

The aim of cerebral autoregulation is to maintain a satisfactory blood flow despite varying blood pressure, as illustrated in Figure 1.8. Within a blood pressure range, the vessel radius changes and compensate for the pressure change so that the flow is kept constant. If the pressure gets too high or too low, the autoregulatory mechanisms can

no longer keep track, and the vessel radius passively follows increases or decreases with the pressure. Lower and upper limit to autoregulation is individual for each neonate, and can shift during progressing pathology or treatment [18]. An exact range has been hard to establish in infants, but some studies suggest a lower limit of autoregulation of about $30\,\mathrm{mmHg}$ [17]. In adults, the lower limit is about 50–$60\,\mathrm{mmHg}$ and the upper limit about 150–$160\,\mathrm{mmHg}$ [64]. Mean arterial blood pressure (MAP) below the gestational age in weeks is often defined as hypotension at the first day of life [18]. There is also a critical closure pressure below which cerebral perfusion ceases. It is thought to be about 22–$33\,\mathrm{mmHg}$ in neonates.

Cerebral pulsations have been known for a long time, and Fog [65] reported changes in cerebral vessel diameter as response to blood pressure drop in 1934, although the idea had been proposed as early as 1900. He used an experimental setup devised ten years earlier, where a window was made in the skull of a cat so that the vessels in the *pia mater* could be observed [66].

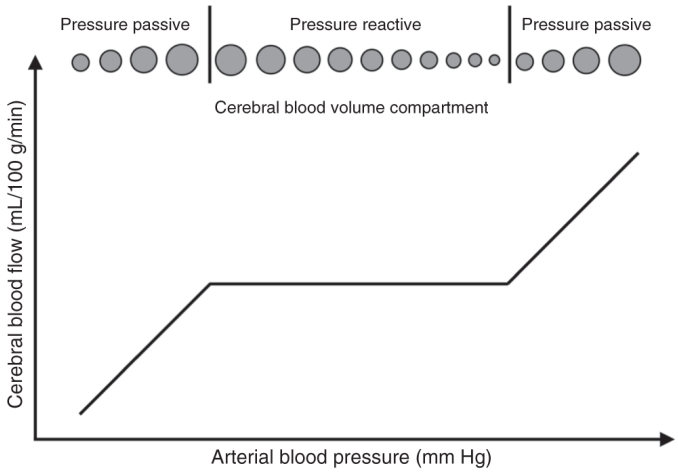

Figure 1.8: Cerebral autoregulation enables the brain to maintain stable blood flow within a limited blood pressure range by adjusting the vessel radius. Outside this range the vessel radius is passively controlled by blood pressure, and the perfusion varies correspondingly. The flow-pressure relation is not as linear as depicted, and flow rate is related to vessel radius squared. Figure by Rhee et al. [18], reprinted with permission from Springer Nature.

At least three different, and not mutually exclusive, theories exist for which mechanisms constitute autoregulation [64],

1. the myogenic mechanism, where changes in pressure and flow alter the membrane potential in smooth muscle cells around the vessel so that they contract or dilate;
2. the metabolic mechanism, where venous CO_2, and likely other substances as well, from the metabolism diffuses to arterioles that respond with either dilatation or constriction; and
3. the neurogenic and endothelial cell-related factor mechanism, where activated brain areas communicate their increased demand for nutrition and oxygen to the nearby

vessels through neural signalling and biochemical signals along different cell types and the endothelium in the brain. This is often termed neurovascular coupling.

In this project, the cerebral autoregulation is not described at the level of individual mechanisms, but only as a total effect.

1.5.3 The Tilt Test

When a child is tilted with the head upwards, as illustrated in Figure 1.9, a height difference occurs between the heart and the brain. This introduces a pressure due to gravity,

$$P_g(h)[\mathrm{mmHg}] = \rho h g k_c^{-1} = 0.77\,\mathrm{mmHg\,cm^{-1}} \cdot h, \tag{1.4}$$

where $\rho = 1.05\,\mathrm{kg\,L^{-1}}$ is the density of foetal whole blood [28], h the difference in height between the heart and the brain, $g \approx 9.81\,\mathrm{m\,s^{-2}}$ is specific gravity, and $k_c \approx 133.3\,\mathrm{Pa\,mmHg^{-1}}$ is a converting factor [67]. Similarly, a pressure gradient is created along the entire body of the infant, and blood may tend to pool up on the venous side in the lower body, reducing venous return and thus CO. The effect of venous pooling is well known in the adult [see eg. 68–70]. For the infant, however, the importance of venous pooling seems not to be known in detail. Murat et al. [71] found that children younger than 8 years did not experience a change in systolic blood pressure in response to extradural anaesthesia. One explanation may be that younger children have a smaller relative blood volume in the lower body compared to adults, and also that younger children have a lower level of systemic resistance at rest [71, 72]. The lack of peripheral blood volume redistribution is suggested to explain the stability of left ventricular end-diastolic volume (LVEDV) and SV during tilt [73].

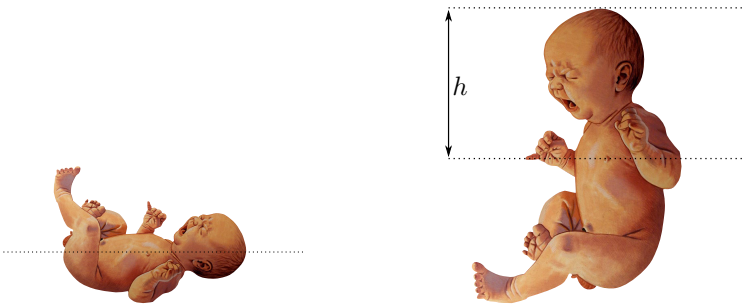

(a) An infant in supine position with the heart and the head in the same height.

(b) The upright position introduces a hydrostatic pressure.

Figure 1.9: When an infant is tilted 90° from the supine position, the height difference h between the heart and the brain creates a pressure gradient due to gravity. This leads to a drop in blood flow to the brain in the absence of regulatory mechanisms. Adapted from a painting by Szabolcs [74], licensed under CC BY-SA 3.0.

An intriguing study by Seymour and Arndt [75] explored how blood pooling and head-to-heart hydrostatic pressure both contributed to cardiovascular response to tilt in snakes. By tilting the whole snake or only segments of it, they found that the vertical distance

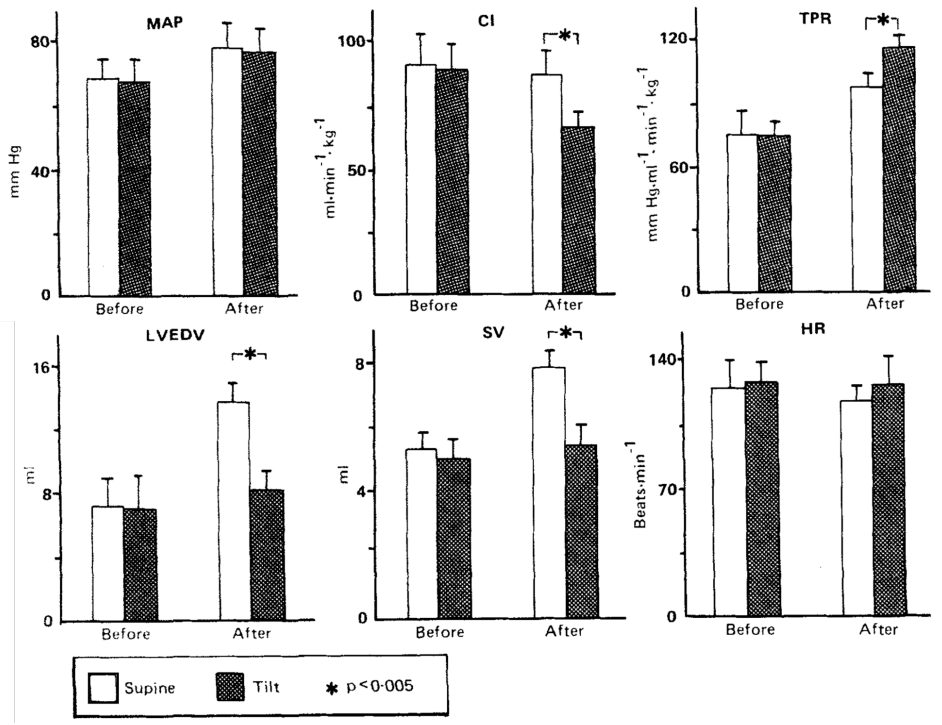

Figure 1.10: Response to a 90° tilt before and after acquiring the ability of maintaining upright position in 14 male infants. Abbreviations: MAP, mean arterial blood pressure; CI, cardiac index (CO divided by body weight); TPR, total peripheral resistance; LVEDV, left ventricle end-diastolic volume; SV, stroke volume; HR, heart rate. Adapted from Magrini et al. [73], reprinted with permission from Oxford University Press.

between head and heart influenced head blood pressure 2–4 times more than blood pooling. In humans, a negative pressure can be applied to the lower body to investigate the effects of shift in blood volume towards the lower body [76]. It has been found that the physiological response differs between head-up tilt (HUT) and lower body negative pressure (LBNP), with cerebral blood flow velocity less reduced during LBNP vs HUT from 3 minutes and onward [77].

Magrini et al. [73] examined the response to a 90° tilt in 14 male infants before (at 6 months) and after (at about 18 months) they had learnt to maintain erect position. The main results are shown in Figure 1.10. At the first tilt test, none of the assessed parameters (SV, cardiac output, total peripheral resistance (TPR), MAP, heart rate and LVEDV) were significantly altered. After acquiring erect position, LVEDV fell significantly, as did SV, and despite a small increased heart rate, a decrease in CO was observed. Increased TPR compensated for lowered CO so that MAP was kept stable. It is also noted that the urinary excretion decreases in the same period of life, indicating maturation of mechanisms regulating blood volume.

Regulatory mechanisms have to be evoked to prevent loss of blood flow to the brain,

as in the case of standing up. Most tilt experiments focus on the change in heart rate and blood pressure as these are easily measured. Figure 1.11 summarises the tilt response in blood pressure and heart rate in newborns and children in different studies. References for the figure, special condition (if present) of the group studied, and basal values are found in Table A.1.

The tilt response shows large diversity between individuals, but also in the same individual over time. Figure 1.12 demonstrates the variety in a small group of pre-term and term neonates [78]. The variability was higher in the preterm infants, and they showed in average a smaller initial response to $45°$ head-up tilt than term infants. In both groups, some infants responded with an increase in blood pressure or heart rate, whereas others responded with a decrease. Hänninen, Peltonen and Hirvonen [19] followed premature infants for several days after birth and measured the blood pressure before and after a $30°$ HUT. The measured response of four different infants is shown in Figure 1.13 as they aged. Again, a remarkable diversity is revealed. During the first week of life, all four newborns have displayed both increase and decrease in blood pressure in response to tilt.

The response in heart rate is similarly varied. Five characteristic responses (profiles) have been described [23, 79],

P1 Sustained bradycardia (decreased heart rate),

P2 Sustained tachycardia (increased heart rate),

P3 Initial bradycardia with subsequent increase,

P4 Initial tachycardia with subsequent decrease, and

P5 No change in heart rate.

Edner et al. [79] found that 88% of healthy infants responded as P2 or P4 compared to 55% in infants with an apparent life threatening event, and hypothesised that this may be a manifestation of underlying autonomic dysfunction in the latter group. The study group was small consisting of only 12 infants. Galland et al. [80] studied 60 infants with only 15% characterised as P1, P2 or P5, and these were typically younger infants. They also found sleep state (active vs quiet sleep) to be associated with the strength of the tilt response. Figure 1.14 demonstrates how sleep state affects tilt response in another study. Mazursky et al. [81] reported a gradual increase in heart rate in premature infants as response to tilting. Heart rate increased with postnatal age with regression coefficient $0.45(12)$ bpm/week. Table A.1 and Figure 1.11 summarise responses reported in the literature. Maternal smoking status seems not to affect the heart rate response to tilt [80, 82].

SV and CO are reported to decrease in response to tilt in adults [84–87]. Some studies find a peak in heart rate immediately after the tilt, causing a temporary peaking in CO [84], but the peak is not observed in all studies [86]. Invasive measurements were performed in a dog [88]. SV was found to decrease with a corresponding increase in heart rate, leading to a not significant change in CO. Li et al. [89] studied children (mean age 11 years) experiencing vasovagal syncope and found a decrease in CO and increase in periperal resistance after a $60°$ HUT. Nevertheless, Shekhawat, Sasidharan and Lewis [90] did not find any significant changes in neither SV nor CO during $30°$ and $60°$ tilts in infants born

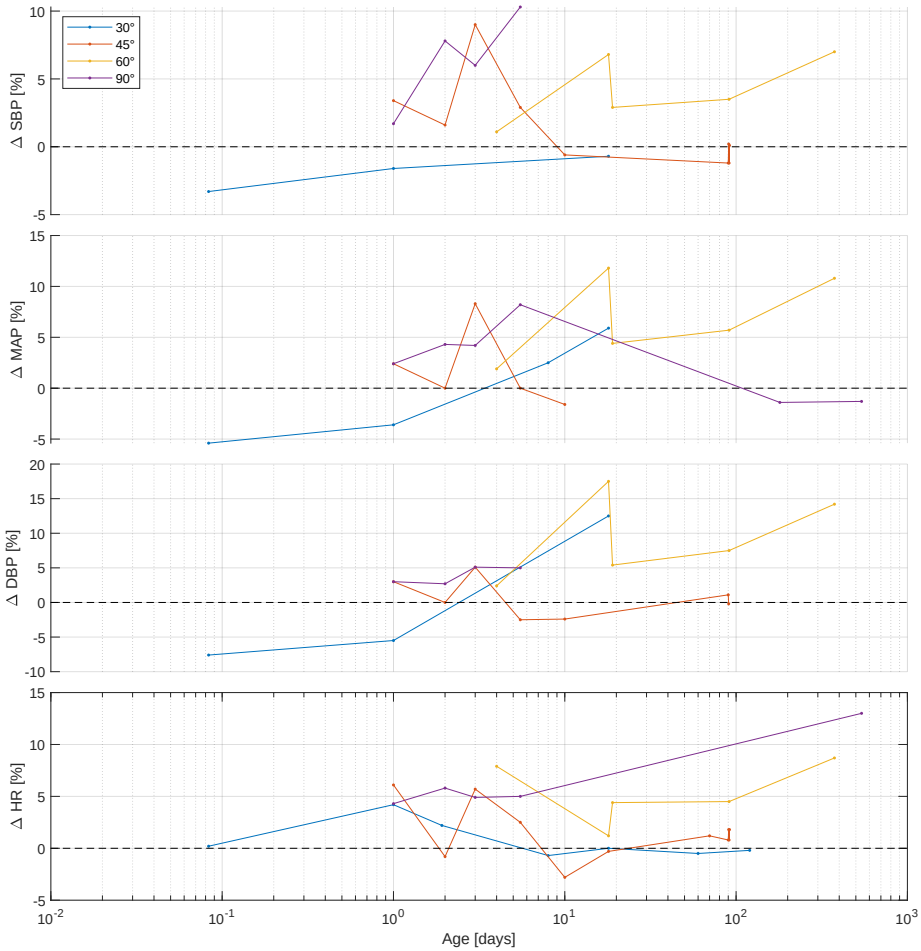

Figure 1.11: Several studies have investigated how infants of different age respond to tilts at different angles given by the different colours, as indicated. The plot shows the relative change in the systolic (SBP), the mean arterial (MAP) and the diastolic (DBP) blood pressure, as well as the heart rate (HR), as the child is tilted. References and details are found in Table A.1.

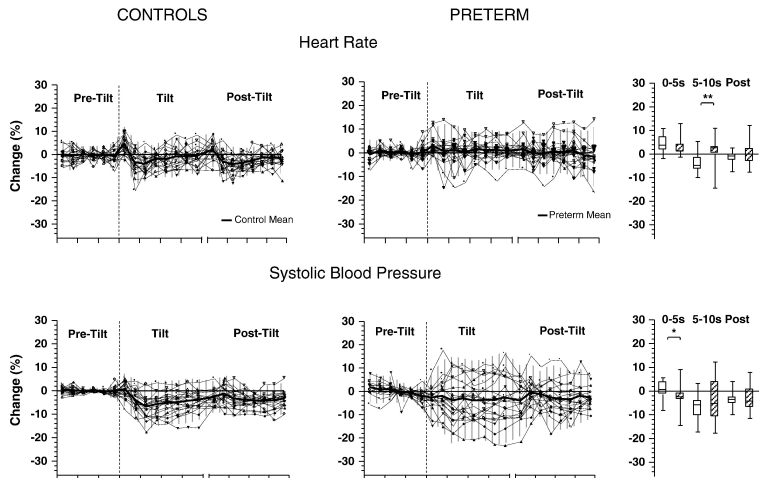

Figure 1.12: Pre-term infants were tilted 45° with the head up. The control group consisted of term infants and the measurements were conducted 12 weeks after birth. Adapted from Viskari-Lähdeoja et al. [78], and reprinted with permission from Elsevier.

at gestational age 24–36 weeks. Nor did Magrini et al. [73] find any change in SV, left ventricle end-diastolic volume, total peripheral resistance or CO per body weight (cardiac index) after a 90° tilt. Change in SV, CO and systemic resistance has been observed in left-lateral position compared to supine, and decreased SV observed in prone position [91].

The influence of tilt on cerebral blood flow (CBF) has also been investigated. Anthony, Evans and Levene [24] identified four typical responses to a 20° tilt with head up or down. The experimental setup resembled NeoDoppler, using a button-sized ultrasound transducer fixated to the temporal bone of 60 neonates of gestational age 24–41 weeks and less than 7 days old. The responses observed were categorised as

R1 Equivocal/cycling, where CBF cycled both before and after the tilt, concealing the response (if any),

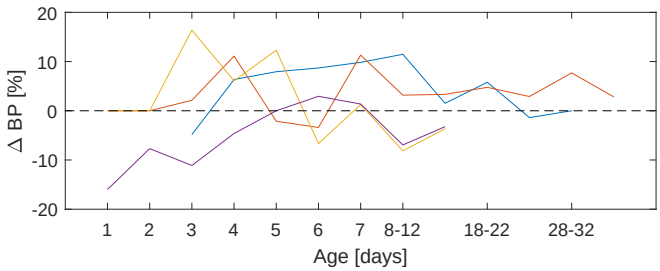

Figure 1.13: Premature infants were exposed to a 30° head-up tilt on several consecutive days after birth, and the change in blood pressure (BP) recorded. The plot shows four individual infants. Data from Hänninen, Peltonen and Hirvonen [19].

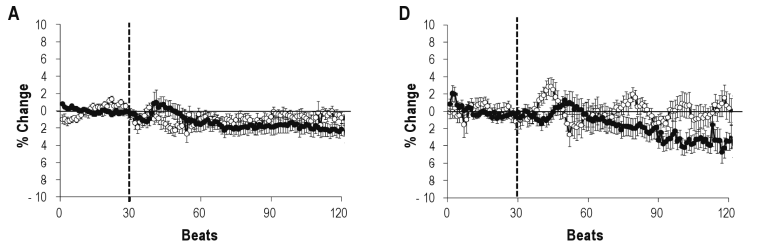

Figure 1.14: Beat-to-beat change in systolic blood pressure (closed circles, •) and heart rate (open circles, ○) in response to a $15°$ tilt (dotted line) in 2–4 weeks old infants. The left panels show the response during quiet sleep, while the right panels show the response during active sleep. Adapted from Yiallourou et al. [83], and reprinted with permission of the Oxford University Press.

R2 No response, where CBF seemed undisturbed by the tilt,

R3 Uniphasic, where a sudden shift in CBF was observed within $5\,\mathrm{s}$ of the tilt, but with no second change within $20\,\mathrm{s}$ of the first,

R4 Biphasic, as R3 but with a second change occurring within $20\,\mathrm{s}$ of the first change.

It was observed that the proportion of infants responding as R4 increased with gestational age. Most of the infants in the study were preterm and in intensive care. R3 and R4 responses were observed in epochs independently of mean arterial blood pressure and arterial carbon dioxide tension. It was suggested that R2 responses were observed due to the tilting being too slow, as not all mattresses had the same tilt mechanism. Only systolic velocity was analysed. Pichler et al. [92] found a change in cerebral blood volume in the range -123 to $67\,\mu\mathrm{L}/100\mathrm{g\,brain}$ (median -25) in term neonates, compared to -169 to $126\,\mu\mathrm{L}/100\mathrm{g\,brain}$ (median -31) in preterms. The tilt was $20°$, and the mean age of the infants was 13 days.

> But you don't dissect a bird to find the origins of its song.
>
> Brodskij [93, p. 356]

1.6 Ultrasound and NeoDoppler

Despite its short history, the importance of ultrasound (US) in obstetrics and perinatology cannot be overstated [94]. The first US images of a foetus is reportedly by Donald, Macvicar and Brown [95], shown in Figure 1.15, published in the Lancet in 1958 [94]. A few years later, Doppler US recorded foetal heart movements [96]. Since then, considerable advances have been made and US quickly became an invaluable part of the neonatal intensive care units [97]. Here, only a brief overview of the principles and technology of Doppler US is given. The section is based on the works of Angelsen [98] and Webb and Flower [99, Ch. 6] if other sources are not cited.

Figure 1.15: One of the first published foetal US images, showing the breeches of twins. Image by Donald, Macvicar and Brown [95], reprinted with permission from Elsevier.

1.6.1 Ultrasound

An ultrasound pulse starts as an electrical (voltage) sine wave with centre frequency f_0 produced by a signal generator. The signal is amplified and applied to one or more transducer elements consisting of a piezoelectrical crystal, a backing material and a matching layer. The crystal changes thickness in response to the applied voltage, creating a longitudinal pressure wave when the transducer is brought in contact with the tissue.

An acoustic wave propagating through a medium will move with a wave speed c_0. The

medium's acoustic impedance (or characteristic mechanical impedance) is defined as

$$Z = 1/(\kappa c) = \rho c = \sqrt{\frac{\rho}{\kappa}} \tag{1.5}$$

whereρ is mass density and κ compressibility. If the acoustic impedance changes at an interface from Z to Z_1, a proportion of the wave's energy will be reflected, r^2, and a proportion transmitted, $1 - r^2$, through the interface,

$$r = \frac{p_r}{p_i} = \frac{Z_1 \cos\theta_i - Z \cos\theta_t}{Z \cos\theta_t + Z_1 \cos\theta_i}, \quad \text{(1.6a)} \qquad t = \frac{p_t}{p_i} = \frac{2Z_1 \cos\theta_i}{Z \cos\theta_t + Z_1 \cos\theta_i}, \quad \text{(1.6b)}$$

where θ_i and θ_t are the angle between a normal to the interface, and the direction of incoming and transmitted wave fronts, respectively. p_i, p_t and p_r are incoming, transmitted and reflected pressure. The echo reflected can be detected by receiver elements containing piezoelectrical crystals, amplified, converted to a digital signal, processed, filtered, and being used to create a map of the medium.

The signal will be altered at several stages of the process. Mechanical properties of the probe determines how the voltage signal is transformed to a pressure wave and vica versa, and the tissue further modifies the wave through frequency dependent absorption and scattering.

Doppler ultrasound

The Doppler effect was first described by Christian Doppler [100] in 1842 to account for the colour of binary stars. At that time, attempts had already been made to map the ocean floor using echo-sounding [101]. After the second world war, the research into diagnostic US flourished, and the Doppler effect was soon exploited to give information about flow velocity.

Continuous-Waved Doppler

Assume a stationary source and an observer moving with velocity $\mathbf{v}(t)$. The source is emitting continuous waves with frequency f_0 along the unit vector $\mathbf{e}_t$ in a medium with wave velocity c_0. The wave length is $\lambda_0 = c_0/f_0$. The wave front needs the time $\lambda_0/c_0 = 1/f_0$ to travel this distance, and in that time, the observer has moved approximately a distance d away from the wave front. If $1/f_0$ is small compared to $|\frac{\mathrm{d}\mathbf{v}}{\mathrm{d}t}|$, the velocity $\mathbf{v}(t)$ is close to constant,

$$d = \int_0^{1/f_0} \mathbf{v}(t) \cdot \mathbf{e}_t \, \mathrm{d}t \approx \mathbf{v} \cdot \mathbf{e}_t / f_0 \tag{1.7}$$

Hence, a delay $\Delta t = d/c_0 = \mathbf{v}\cdot\mathbf{e}_t/(c_0 f_0)$ is introduced. The observed frequency becomes $f' = 1/(1/f_0 + \Delta t)$, and the shift is

$$f_s = f' - f_0 = f_0\Big(\frac{c_0}{c_0 + \mathbf{v} \cdot \mathbf{e}_t} - 1\Big) = f_0 \frac{\mathbf{v} \cdot \mathbf{e}_t}{c_0 - \mathbf{v} \cdot \mathbf{e}_t} \approx f_0 \frac{\mathbf{v} \cdot \mathbf{e}_t}{c_0}, \tag{1.8}$$

where the approximation holds when $|\mathbf{v}| \ll c_0$. In US, the signal has to be echoed to a receiver. The analysis is similar to the one above, with the observer now acting as a source

and the receiver as the observer. A second shift f_s appears, yielding the general Doppler shift [102]

$$f_D = \frac{f_0}{c_0}(\mathbf{e}_t + \mathbf{e}_r) \cdot \mathbf{v}, \tag{1.9}$$

where $\mathbf{e}_t$ and $\mathbf{e}_r$ are normal vectors to the transducer and the receiver surfaces, respectively. The transducer and the receiver will create an overlapping area, and only scatterers moving in this region are measured.

To successfully calculate the velocity v from Eq. (1.9), the angles between $\mathbf{e}_t$, $\mathbf{e}_r$ and $\mathbf{v}$ have to be known. Uncertainty in the angles will contribute to a large uncertainty in v when the angles are close to $90°$, and the Doppler shift disappears if the emitter and receiver are parallel and the scatterer is moving normal to the wave propagation.

Usually, the probe contains both sender and receiver elements so that $\mathbf{e}_t$ and $\mathbf{e}_r$ are close to parallel with an angle θ to $\mathbf{v}$. Hence Eq. (1.9) can be simplified to

$$f_D = \frac{2f_0 v \cos\theta}{c_0},$$

or equivalently

$$v = \frac{f_D c_0}{2f_0 \cos\theta}. \tag{1.10}$$

Pulse-Waved Doppler

Pulse-waved Doppler (PW Doppler) can be used when depth resolution is desired in addition to information regarding velocity and movement. In PW Doppler, a train of short wave pulses (typically a few cycles long) with center frequency f_0 emitted with pulse repetition frequency (PRF) is used. The same probe elements are often used as both transducer and receiver. Figure 1.16 contains a calculated example.

The wave pulse travels at speed c_0, hits the scatterer in distance d after a time $\Delta t/2 = d/c_0$, the wave is scattered back and returns at the receiver a time Δt after the pulse was sent. This is the echo return time. The process repeats with PRF, with the distance increasing or decreasing for each repetition. Assuming that $|\mathbf{v}| \ll c_0$ and $\mathbf{v}$ is constant in the period 1/PRF, the scatterer moves a distance $\mathbf{v} \cdot \mathbf{e}_t/\text{PRF}$ in between the pulse wave emissions. Assume for simplicity constant velocity $\mathbf{v}$. The echo return time thus becomes a function of scatterer velocity, pulse wave direction, and PRF, according to

$$\Delta t_i = \frac{2d_0}{c_0} + 2i\frac{\mathbf{v} \cdot \mathbf{e}_t}{\text{PRF} \cdot c_0}, \tag{1.11}$$

where i denotes the number of the pulse in a series and d_0 the initial distance to the scatterer. The factor 2 is needed as the wave travels both ways. Hence a phase shift ϕ is introduced to the received signal s_r,

$$\begin{aligned} s_r(t) &= g(t)\sin(2\pi f_0(t + \Delta t_i)) = g(t)\sin(2\pi f_0 t + \phi_i), \\ \phi_i &= 2\pi f_0 \Delta t_i = \frac{4\pi f_0}{c_0}\Big(d_0 + i\frac{\mathbf{v} \cdot \mathbf{e}_t}{\text{PRF}}\Big) = 2\pi f' i/\text{PRF}, \\ f_D &= 2\frac{f_0}{c_0}\Big(d_0 + \mathbf{v} \cdot \mathbf{e}_t\Big), \end{aligned}$$

where $g(t)$ accounts for the pulsing of the wave, and ϕ becomes a signal sampled at a frequency PRF, as illustrated in Figure 1.16a. If θ is the angle between the wave propagation direction and the scatterer's velocity, and the initial phase shift is corrected, an expression similar to Eq. (1.10) appears,

$$v = \frac{f_D c_0}{2 f_0 \cos\theta}. \tag{1.12}$$

f_D can then be found from the Fourier spectrum of $\sin(\phi_i)$ as shown in Figure 1.16b. Eq. (1.12) is similar to Eq. (1.10) as the time delay of the signal depends on the movement of the scatterer in relation to the probe in both cases, and thus results in the same shift in frequency.

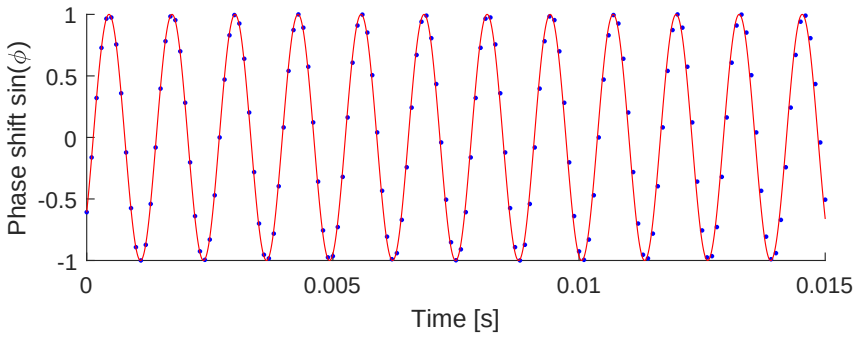

(a) The blue dots shows sine of the phase shift sampled with PRF, and red curve is $\sin(2\pi f' t)$. Details in the text.

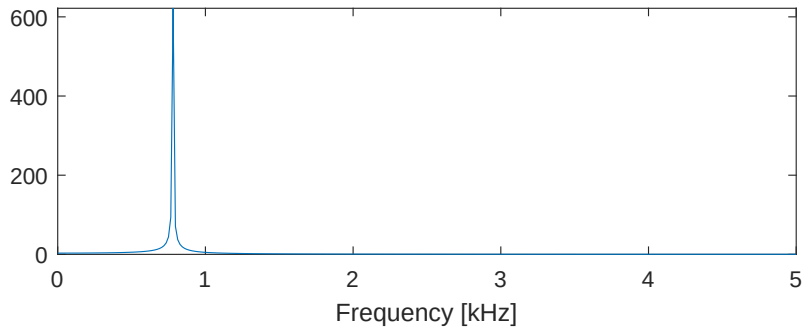

(b) Positive half of the Fourier spectrum of Figure 1.16a, with a clear peak at $f = 781\,\mathrm{Hz}$. This can be used to calculate the scatterer's speed from Eq. (1.12), yielding $v = 20\,\mathrm{cm\,s^{-1}}$.

Figure 1.16: Demonstration of important events in PW Doppler. Here, a scatterer with initial distance $d_0 = 1\,\mathrm{mm}$ moves away from the probe with speed $20\,\mathrm{cm\,s^{-1}}$, in a medium with wave propagation speed $c_0 = 1540\,\mathrm{m\,s^{-1}}$. PRF and f_0 are set to 10 kHz and 3 MHz, respectively.

Some observations can be made. According to the Nyquist–Shannon sampling theorem, the sampling frequency of a signal has to be at least twice the highest frequency of interest in the signal. If a lower sampling frequency is used, aliasing occurs. In terms of

PW Doppler, this implies that PRF sets a limit to the maximal velocity measurable, v_{Nyquist}. Since PRF is the sampling frequency, the highest frequency available in the sampled signal is PRF$/2$ which can be substituted into Eq. (1.12), that is,

$$v_{\text{Nyquist}} = \frac{c_0 \cdot \text{PRF}}{4f_0} = 38.5[\text{cm s}^{-1}]\frac{\text{PRF [kHz]}}{f_0[\text{MHz}]},$$

in tissue with $c_0 = 1540\,\text{m s}^{-1}$. Figure 1.4b shows typical blood flow velocities averaged over a cardiac cycle in different vessels. Systolic peak velocity into the ascending aorta can exceed $120\,\text{cm s}^{-1}$ in healthy adults [103], and $80\,\text{cm s}^{-1}$ in healthy neonates, although values up to $180\,\text{cm s}^{-1}$ have been reported in children [104, 105]. In the presence of pathology, turbulent jets can arise with velocities above $500\,\text{cm s}^{-1}$ [106]. Despite the high peak systolic flow velocity in the aorta, mean flow velocity calculated as aggregated flow divided by cross-section is in the range 20–$35\,\text{cm s}^{-1}$ [44, 46]. Typical blood flow velocities in the anterior and middle cerebral arteries are shown in Figure 1.17.

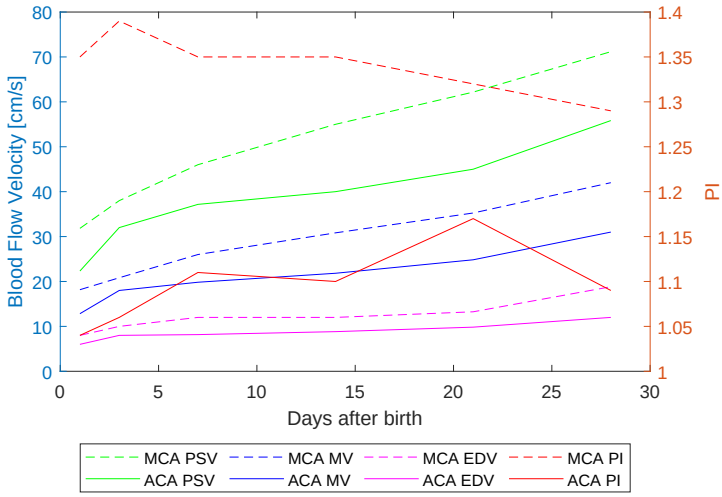

Figure 1.17: Peak systolic (PSV), mean (MV) and end-diastolic (EDV) blood flow velocity in the anterior (ACA) and middle (MCA) cerebral artery the first month after birth for neonates with gestational age > 32 weeks. Pulsatility index (PI) is defined Eq. 1.13. Median values acquired from a study by Pezzati et al. [107].

To prevent range ambiguity, a new pulse can only be sent after receiving the echo from the previous pulse. PRF is thus limited by the depth of the object of interest, and cannot exceed echo return time inverse, defined as

$$\text{PRF} \leq \frac{c_0}{2d_{max}} = \frac{770[\text{kHz mm}]}{d_{max}[\text{mm}]},$$

in tissue with $c_0 = 1540\,\text{m s}^{-1}$. The axial (depth) resolution l, on the other hand, is

derived from the pulse duration τ,

$$l = \frac{c_0 \tau}{2}.$$

As the scatterer moves beyond the observable depth, the observation time of the scatterer is limited. This broadens the frequency spectrum in Figure 1.16b, and an uncertainty in measured velocity arises in form of spectrum broadening, creating the rims in Figure 1.18.

B mode images have to be acquired during the procedure to visualise where in the tissue the velocities are measured. This adds another compromise to be made between frame rate and resolution.

In practise, the process is more complicated. Technical limitations and specific requirements in terms of frame rate and resolution make it necessary to customise equipment, setup and signal processing to fit the intended use. Examples of Doppler spectra in a healthy child are shown in Figure 1.18.

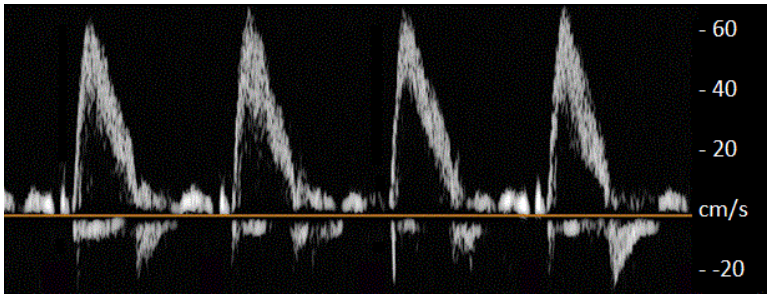

(a) Left ventricular outflow tract.

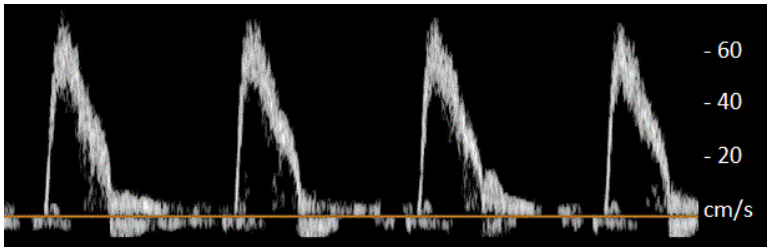

(b) Ascending aorta.

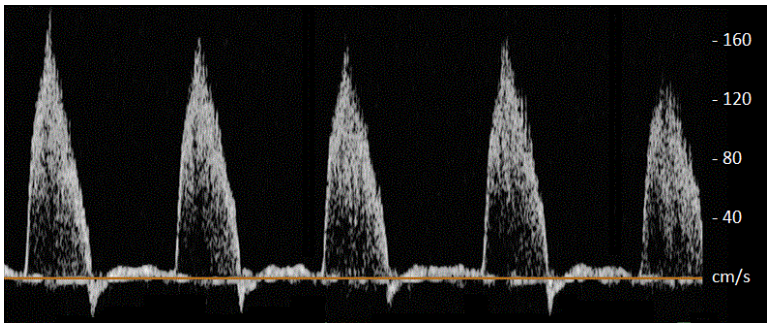

(c) Descending aorta.

Figure 1.18: Typical Doppler spectra obtained from a healthy child. Adapted from Hofbeck, Deeg and Rupprecht [105] and reused with permission from Springer Nature.

1.6.2 NeoDoppler

Fenton, Evans and Levene [108] engineered 'a small, lightweight probe and cable that are attached to the infant's skin to record cerebral blood flow velocity from the middle cerebral artery over a period of hours' in the late 1980's. This concept has recently been revitalised as NeoDoppler by the Ultrasound Research Group at NTNU in a project led by professor Hans Torp [16]. Using a coin sized probe fixed over the anterior fontanelle as demonstrated in Figure 1.20, Doppler US offers the opportunity of continuous surveillance of cerebral blood flow velocities. The working principles of Doppler US is described above.

Hardware

The NeoDoppler equipment consist of a single-element probe, a scanner (*Manus EIM-A*, Aurotech Ultrasound AS, Tydal, Norway), and an interface with display, as schematically depicted in Figure 1.19. The probe is circular with a diameter of $1\,\mathrm{cm}$, and has a depth range of 3–$35\,\mathrm{mm}$ [15]. The emitted pulse waves have a central frequency of $7.8\,\mathrm{MHz}$.

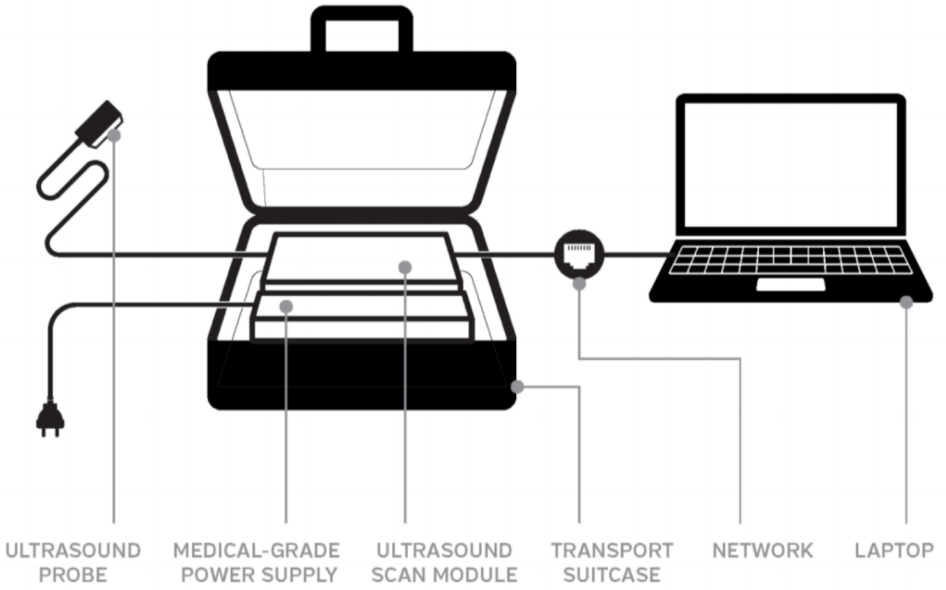

Figure 1.19: Main components of the NeoDoppler set-up. Figure by Hergum [109], reprinted with permission.

The probe is fixed on the anterior fontanelle as demonstrated in Figure 1.20. It is not necessary to identify the vessel of observation as the flow in both the anterior and middle cerebral arteries, as well as right and left great vessels, are highly correlated [15]. In this project, it is assumed that the anterior cerebral artery is recorded.

Software

The accompanying software EarlyBird has been made for NeoDoppler. The program processes raw data from the probe and scanner, and presents it as a Doppler spectrum. In addition, the depth of interest can be adjusted so that different vessels can be chosen. Gain is also adjustable, as well as parameters used for filtering. In this project, all these settings were optimised by the test technician.

The software also allows for velocity tracing and heart beat extraction. An example of trace extraction and heart beat detection is shown in Figure 1.21. Heart beats are identified by detecting the sharp increase in systolic velocity.

Finally, the software calculates several averages parameters from the recordings, such as HR, resistivity index, pulsatility index (PI), and mean velocity. PI is a frequently used

(a) Photo kindly provided by Frida J. Krüger and printed with permission.

(b) From an animation by NTNU TTO [110], used with permission.

Figure 1.20: The NeoDoppler probe is attached over the anterior fontanelle in a specially designed cap **(a)** to survey the blood flow velocity in the anterior cerebral artery **(b)**.

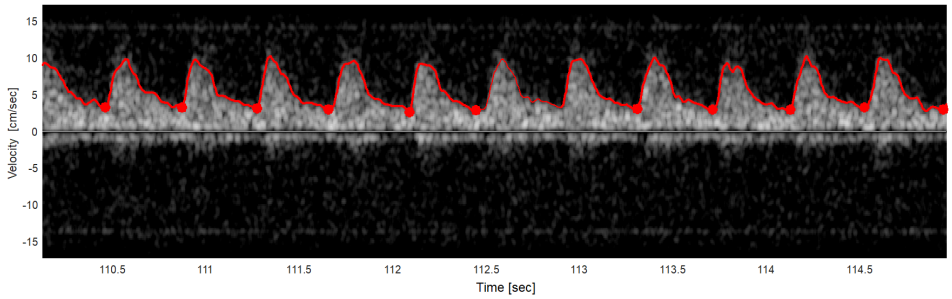

Figure 1.21: A Doppler spectrum was acquired using the NeoDoppler equipment, and processed by the EarlyBird software. A velocity trace is shown in red, with dots indicating the beginning of a heart cycle. One beat is skipped by the algorithm.

measure of pulsatility, defined as

$$\mathrm{PI} = \frac{q_{\text{systole}} - q_{\text{diastole}}}{\bar{q}} = \frac{v_{\text{systole}} - v_{\text{diastole}}}{\bar{v}}, \tag{1.13}$$

where q_{systole} and q_{diastole} are the flow rates in systole and diastole, respectively, and $\bar{q}$ the average flow rate. Similar definitions apply for flow velocity v. In this project, the parameters are calculated outside the EarlyBird software, using only the velocity trace. Customised interfaces have been made for special application, for example if the probe is used for other measurements than the cerebral blood flow.

1.7 Modelling of Blood Circulation

The NeoDoppler equipment described in Section 1.6.2 makes the continuous surveillance of cerebral blood flow feasible. To fully exploit the information carried in the signal, variations in blood flow and features of the wave profile could be correlated to physiological mechanisms such as the autoregulatory capacity. This section provides an overview of how blood circulation can be described mathematically and modelled. It finishes by introducing a model of foetal circulation, which is developed to fit the neonate in section 2.2, and briefly presenting simulation software used.

1.7.1 Basic Hemodynamics

Blood is a fluid consisting of protein-rich plasma, red and white blood cells, and platelets [44, Ch. 18]. It is distributed through the body in vessels driven by a pressure gradient created by the heart, as described in Sections 1.5.1 and 1.5.1. In general, the behaviour of an incompressible fluid with constant density ρ and viscosity μ in the gravitational field $\mathbf{g}$ is governed by the Naiver-Stokes equation for momentum,

$$\rho\frac{\mathrm{d}\mathbf{V}}{\mathrm{d}t} = \rho\mathbf{g} - \boldsymbol{\nabla}p + \mu\boldsymbol{\nabla}^2\mathbf{V}, \tag{1.14}$$

and the continuity equation,

$$\boldsymbol{\nabla}\cdot\mathbf{V} = 0, \tag{1.15}$$

where $\mathbf{V}(\mathbf{r}_0, t) = [V_x(x, y, z, t), V_y(x, y, z, t), V_z(x, y, z, t)]$ is a velocity field [111, Ch. 4]. When looking at tubes, as in the case with blood vessels, cylindrical coordinates are useful [112, Ch. 2]. Introducing the familiar coordinates

$$\begin{aligned} x &= r\cos\theta, \\ y &= r\sin\theta, \\ z &= z, \end{aligned}$$

yields

$$\boldsymbol{\nabla}\psi(r,\theta,z) = \frac{\partial\psi}{\partial r}\mathbf{e}_r + \frac{1}{r}\frac{\partial\psi}{\partial\theta}\mathbf{e}_\theta + \frac{\partial\psi}{\partial z}\mathbf{e}_z, \tag{1.16}$$

$$\boldsymbol{\nabla}\cdot\boldsymbol{\psi} = \frac{1}{r}\frac{\partial}{\partial r}(r\psi_r) + \frac{1}{r}\frac{\partial\psi_\theta}{\partial\theta} + \frac{\partial\psi_z}{\partial z}, \tag{1.17}$$

$$\boldsymbol{\nabla}^2\psi(r,\theta,z) = \frac{\partial^2\psi}{\partial r^2} + \frac{1}{r}\frac{\partial\psi}{\partial r} + \frac{1}{r^2}\frac{\partial^2\psi}{\partial\theta^2} + \frac{\partial^2\psi}{\partial z^2}, \tag{1.18}$$

with $\boldsymbol{\psi} = \psi_r\mathbf{e}_r + \psi_\theta\mathbf{e}_\theta + \psi_z\mathbf{e}_z$, where $\mathbf{e}$ is a unit vector [113].

When a fluid moves along a surface, fluid in contact with the surface will have the same velocity as the surface itself [111, Ch. 2]. This is commonly referred to as the *no-slip* condition. As blood is comparted within vessels, and the vessels are stationary and (for the moment treated as) rigid, there will be an outermost cylindrical layer of blood that does not move ($\mathbf{V} = 0$ for $|\mathbf{r}| = a$, where a is the radius of a tube coaxial to $\mathbf{e}_z$). A new cylindrical layer lies immediately central to stationary layer, moving slowly with the stationary layer

as lubricant [112, Ch. 2]. This repeats towards the central axis, where the fastest moving fluid is found. The cylindrical layers shear each other, instead of slipping or sliding. The cylindrical symmetry implies that there is no angular variations (i.e. $\frac{\partial \mathbf{V}}{\partial \theta} = \frac{\partial p}{\partial \theta} = 0$).

If the flow is laminar (that is, all fluid elements flow along the main flow direction, $V_\theta = 0$) and the flow is allowed to fully develop, a flow velocity profile emerges inside the tube. In other words, the cross-sectional velocity distribution will be equal along these parts of the tube (i.e. $\frac{\partial \mathbf{V}}{\partial z} = 0$). One can assume that the flow in many parts of the vascular tree is close to fully developed [112, p. 52]. Under these assumptions, the velocity field $\mathbf{V}$ is only varying along $\mathbf{e}_r$. From Eq. (1.15) it can now be found that the radial component of $\mathbf{V}$ is zero ($V_r = 0$). Looking at only this component of Eq. (1.14),

$$\rho \frac{\mathrm{d}V_r}{\mathrm{d}t} = \rho g_r - \frac{\partial p}{\partial r} + \mu \frac{\partial^2 V_r}{\partial r^2} + \mu \frac{1}{r} \frac{\partial V_r}{\partial r},$$
$$\frac{\partial p}{\partial r} = \rho g_r \approx 0,$$

as the vessels are too narrow for gravity to have a significant effect. Hence, the pressure p is only a function of z and t.

By assuming a steady flow ($\frac{\mathrm{d}\mathbf{V}}{\mathrm{d}t} = \frac{\partial p}{\partial t} = 0$), Eq. (1.14) (along $\mathbf{e}_z$) can be further simplified,

$$\frac{\mathrm{d}p}{\mathrm{d}z} = \rho g_z + \mu \frac{\mathrm{d}^2 V_z}{\mathrm{d}r^2} + \mu \frac{1}{r} \frac{\mathrm{d}V_z}{\mathrm{d}r}. \tag{1.19}$$

As the left and right side of Eq. (1.19) is differentiated with respect to separate variables, both sides have to equal a constant, c. The contribution from g_z depends on the position of z relative to the gravitational field and is considered zero for the moment. Starting with the left hand side, $\frac{\mathrm{d}p}{\mathrm{d}z} = c$ is solved by $p(z) = (c + \rho g_z)z + p(0)$. Looking at a segment of the vessel of length l, starting in $z = 0$, the pressure gradient along the vessel is $c = (p(l) - p(0))/l$. The right hand side becomes

$$\frac{c}{\mu} = \frac{\mathrm{d}^2 V_z}{\mathrm{d}r^2} + \frac{1}{r} \frac{\mathrm{d}V_z}{\mathrm{d}r},$$

which has the solution $V_z(r) = \frac{c}{4\mu} r^2 + A \ln r + B$, where A and B are constants arising from the integration. $A = 0$ as $V_z(0) \neq \infty$, and utilising the no-slip condition, $V_z(a) = \frac{cA^2}{4\mu} + B = 0$, yields $B = -\frac{c}{4\mu} a^2$. Thus,

$$V_z(r) = \frac{\Delta p}{4l\mu}(a^2 - r^2), \tag{1.20}$$

where $\Delta p = p(0) - p(l)$. Such flow is commonly referred to as *Poiseuille Flow* [112, p. 60]. Radially, the flow velocity takes the shape of a parabola. By integrating over the cross-section, the total volumetric flow rate q is found,

$$q = 2\pi \int_0^a r V_z(r)\, \mathrm{d}r = \frac{\Delta p \pi}{8l\mu} a^4 = \frac{V_z(0)}{2} \pi a^2. \tag{1.21}$$

The latter relation demonstrates that the average velocity is half of the maximum velocity. This relation is important when estimating flow rates from Doppler velocity measurements.

In the case of human circulation, the flow is pulsatile and the tube is not rigid. Zamir [112] provides a comprehensive discussion of the mechanics of such pulsatile flow in elastic tubes. Eqs. (1.14) and (1.15) can no longer be simplified to the same extent as neither $\frac{\mathrm{d}\mathbf{V}}{\mathrm{d}t}$ nor the radial components equal zero. The most important consequence of this is the creation of wave motions. The pressure waves will tend to become more pulsatile as they move more distally from the aorta, although the mean arterial pressure will decrease [44, Ch. 22]. Typical blood flow velocities in different vessels are shown in Figure 1.4b. One may also note that the blood flow velocity, typically below $1\,\mathrm{m\,s^{-1}}$, is far lower than the wave propagation velocity, which can be estimated to be about $10\,\mathrm{m\,s^{-1}}$ [112, Ch. 5.2].

To account for gravity, the term $\rho(\mathbf{g}\cdot\mathbf{e}_z)l$ can be added to Δp.

1.7.2 Electrical Analogy

The complexity of the blood flows in the body is overwhelming, with static and dynamic components and regulatory mechanisms intertwined and orchestrated. Section 1.7.1 developed important relations between flow and pressure under the assumptions of

- an incompressible fluid with constant density ρ and viscosity μ,
- no-slip condition,
- gravity plays a negligible role,
- a steady, fully-developed flow, in a
- rigid tube.

Despite these simplifications, the relations have been found to be useful for studying blood flow [112]. Here, the theory will be applied to show the analogies to electrical components, including the effects of inertia and wall elasticity through inductance and compliance, respectively.

When introducing an electrical analogy, the vasculature can be represented by discrete compartments with electrical components accounting for properties like resistance, inertia and compliance. In sum, this offers a way of breaking down a complex system into lumped part, hence the term *lumped model*.

Resistance

Electrical resistance, R_e, is the ratio of voltage, V_e to current, I_e, that is $R_e = V_e/I_e$. This is a direct analogy to Eq. (1.21) that established a relationship between flow rate q and the pressure drop Δp along a vessel of length l,

$$\Delta p = Rq, \tag{1.22}$$

$$R = \frac{8\mu l}{\pi a^4}, \tag{1.23}$$

where μ is blood viscosity, ρ is blood density, and a the vessel radius. The resistance of a vessel is thus proportional to blood viscosity and vessel length, and reciprocal to vessel

radius to the fourth power. In other words, a small change in radius will have a tremendous effect on vessel resistance.

Several important observations can be made. In a circuit with only resistors driven by a current source (an inflow), the voltage (or pressure) is determined by the total resistance. Figure 1.22 shows a simple circuit. The flow q will be distributed among the parallel resistors R_{par},

$$q_{par,j} = \frac{1/R_{par,j}}{\sum_{i=1}^{n} 1/R_{par,i}} q = \frac{R_{par,tot}}{R_{par,j}} q, \tag{1.24}$$

$$R_{par,tot} = \frac{1}{\sum_{i=1}^{n} 1/R_{par,i}}. \tag{1.25}$$

The voltage, however, is equal across all the parallel resistors, and the voltage p will be

$$p = (R_{ser} + R_{par,tot})q. \tag{1.26}$$

Similarly, the distribution of blood flow follows the same pattern as $q_{par,j}$. Increasing the resistance of a compartment relative to the others, will decrease the flow rate entering that compartment. The systemic blood pressure can be estimated from Eq. (1.26), as

$$\text{MAP} = \text{TPR} \cdot \text{CO}, \tag{1.27}$$

where MAP is mean arterial pressure, TPR is the total peripheral resistance, and CO the cardiac output. Systemic arteries have a large diameter compared to peripheral arterioles and capillaries, and their contribution to the total resistance is thus negligible.

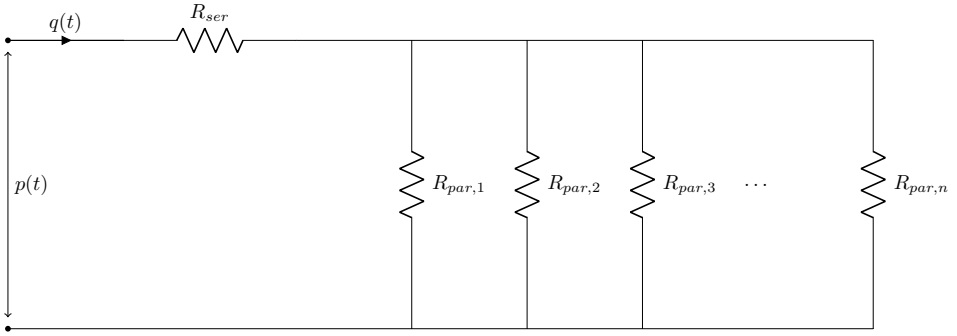

Figure 1.22: A simple circuit with resistors in parallel and series.

One can also notice that if all n parallel resistors have equal resistance, R', Eq. (1.25) simplifies to $R_{par,tot} = R'/n$. In other words, a high number of parallel resistors will in sum contribute with only a small resistance, even if the resistance of each individual resistor is high. This explains why capillaries do not dominate the systemic resistance, despite their small radii. It is estimated that the greater arteries contribute with 19% to TPR, the arterioles with 47%, the capillaries with 27%, and the venous system with about 7%, in adults [47, p. 189].

It should also be noted that *in vivo* resistance is non-linear in relation to pressure [44, Ch. 19]. Figure 1.23 demonstrates such non-linear relationships. High pressure causes the vessel walls to distend, increasing the radius and decreasing the resistance. If the driving pressure falls towards zero, the resistance increases and approaches infinity. Sympathetic stimulation further modifies the non-linear pressure-resistance/flow relationship. The viscosity of blood depends on vessel radius and decreases rapidly in small vessels, an effect called the Fahraeus-Lindqvist phenomenon [44, Ch. 18]. In adults, the blood viscosity falls from about $3\,\mathrm{mPa\,s}$ in vessels with radius above $1\,\mathrm{mm}$ to about $2.8\,\mathrm{mPa\,s}$ at $0.5\,\mathrm{mm}$ and about $2.6\,\mathrm{mPa\,s}$ at $0.25\,\mathrm{mm}$. This phenomenon is neglected in this project.

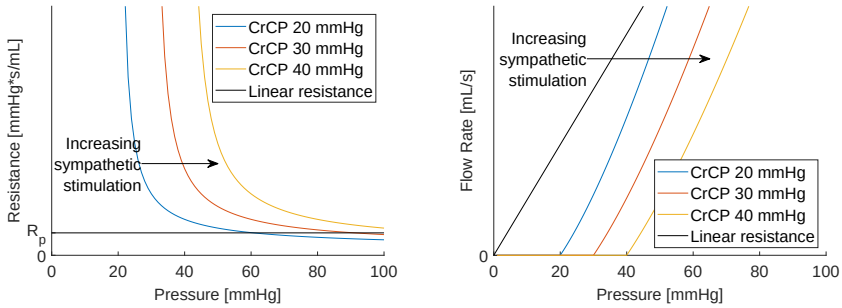

(a) Pressure-resistance relation.

(b) Pressure-flow relation.

Figure 1.23: The relationship between pressure and resistance and flow is non-linear *in vivo*. The black line shows a constant resistance as used in this project. Sympathetic stimulation increases the resistance for a given pressure, and also increases the critical closing pressure (CrCP). The vessel collapses when driving pressure falls below CrCP and there will be no flow. Inspired by Boron and Boulpaep [44, Ch. 19] and Tran [29].

Inertia

Inertia, L, describes the reluctance of a mass of fluid to acceleration or deceleration in time [112, Ch. 8.5]. A bolus with length l of fluid with density ρ in a tube of radius a has a mass

$$m = \pi a^2 l \rho.$$

The bulk of fluid moves with velocity u in response to a pressure difference ΔP_l through the tube. By relating velocity to volumetric flow rate through Eq. (1.21), Newton's law of motion takes the form

$$\pi a^2 l \rho \frac{\mathrm{d}}{\mathrm{d}t}\left(\frac{q}{\pi a^2}\right) = \Delta P_l \pi a^2,$$

which can be rewritten as

$$\Delta P_l = \left(\frac{\rho l}{\pi a^2}\right)\frac{\mathrm{d}q}{\mathrm{d}t} \equiv L\frac{\mathrm{d}q}{\mathrm{d}t},$$

where

$$L = \frac{\rho l}{\pi a^2} \tag{1.28}$$

is the inertia. Eq. (1.28) is analogous to the electrical inductance which opposes the change in current in response to a voltage change. L is proportional to the vessel segment's length, as the bolus of fluid increases in volume. To move a constant volume of fluid, the pressure has to increase if the tube becomes narrower because an increased mean velocity must compensate a smaller cross-section. This explains why L increases for decreasing a.

Compliance

The elasticity of blood vessels introduces *compliance*, i.e. the possibility of change in the total volume of fluid contained in a vessel when pressure changes [112, Ch. 8.6]. The compliance of a vessel thus describes its ability to alter its volume in response to a change in transmural pressure Δp (i.e. pressure over the vessel wall),

$$C = \frac{\Delta V}{\Delta p}$$

or equivalently

$$\Delta p = \frac{1}{C}\Delta V. \tag{1.29}$$

As long as the pressure outside the vessel, p_o, is kept constant, a change in blood pressure, for example along a vessel, is paralleled by a similar change in transmural pressure. Laplace's law states that [114]

$$\Delta p = \frac{h}{a}\tau = \frac{h}{a}\frac{E}{1-\sigma^2}\frac{a-a_0}{a_0}, \tag{1.30}$$

where τ is the circumferential (hoop) stress, a and a_0 are radii with and without an applied transmural pressure, respectively, and h is vessel thickness, E is the Young's modulus, and σ the Poisson ratio. The applicability of Laplace's law to biological systems is debated as it assumes that $h/a \ll \Delta p/p_o$ [115]. In adults, $\Delta p/p_o \approx 0.13$ [115], whereas vessel thickness is assumed to be 15% of a in this project [28].

A change in cylindrical volume is by definition $\Delta V = \pi l(a^2 - a_0^2) = \pi l(a-a_0)(a+a_0)$, or $a - a_0 = \Delta V/\pi l(a+a_0)$ which can be substituted into Eq. (1.30). The resulting expression can be rewritten in the form of Eq. (1.29),

$$\begin{aligned}\Delta p &= \frac{h}{a}\frac{E}{1-\sigma^2}\frac{\Delta V}{a_0\pi l(a+a_0)} = \frac{1}{C}\Delta V,\\ C &= \frac{\pi a a_0(a+a_0)(1-\sigma^2)l}{Eh}.\end{aligned} \tag{1.31}$$

Eq. (1.31) can be applied as it is or further simplified by assuming that the change in radius is small ($a \approx a_0$). Ryu, Hu and Shadden [114] found that this approximation yields less realistic pressure magnitudes and wave forms, and produce a wave propagation speed inconsistent with the theory in a 1D model. Nevertheless, the approximation is often used, also in this project. The estimated compliance is then

$$C = \frac{2\pi a^3(1-\sigma^2)l}{Eh} = \frac{3\pi a^3 l}{2Eh}, \tag{1.32}$$

where σ is assumed to be 1/2 [28, 116].

Compliance finds its analogue in the capacitor, where charge can be stored and current moves into or out of the capacitor as

$$I = \frac{\mathrm{d}V}{\mathrm{d}t} \tag{1.33}$$

where V is voltage across the capacitor [117, Ch. 4]. As the current flows into the capacitor, the voltage across it declines so that less current enters it. This is similar to a vessel that is steadily stretched until the vessel wall stress equals the force applied by the pressure. If the pressure changes, a new equilibrium has to be reached. Figure 1.24 shows a simple RLC circuit. A high-frequent sinusoidal input current q will direct most of the current towards the capacitor and only a constant term will contribute to current through R. In other words, the circuit in Figure 1.24 acts as a low-pass filter if L is small enough to be neglected [117, Ch. 8.6]. If one assumes that the conductor is connected to ground, the circuit acts as a resonant circuit with resonant frequency [117, Ch. 8.12]

$$f_0 = \frac{1}{2\pi}\sqrt{\frac{1}{LC} - \frac{R^2}{L^2}}. \tag{1.34}$$

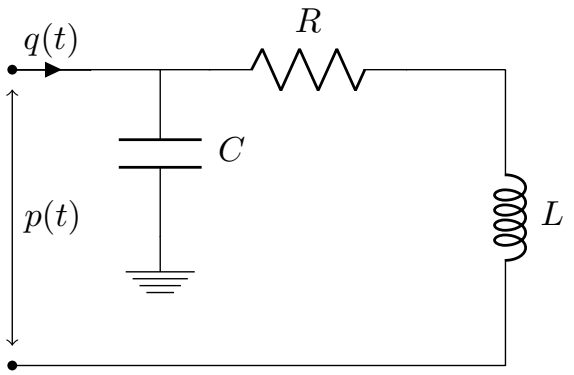

Figure 1.24: A simple RLC circuit.

Zamir [112] offers a thorough review of the complex behaviour arising from R, L and C in combination with physiological pressure wave forms.

Units

The literature houses a range of units for resistance, inductance and compliance. As blood pressures are given in mmHg, flow velocity in $\mathrm{cm\,s^{-1}}$ and flow rate in $\mathrm{mL\,s^{-1}}$, the unit convention used in this paper will be

$$[R] = \mathrm{mmHg\,s\,mL^{-1}},$$
$$[L] = \mathrm{mmHg\,s^2\,mL^{-1}},$$
$$[C] = \mathrm{mL\,mmHg^{-1}}.$$

The relationship $1\,\mathrm{mmHg} \approx 133.3\,\mathrm{Pa}$ can be used to arrive at SI units [67]. This conversion is also made when using Eqs. (1.22), (1.28) and (1.32) to estimate resistance, inertia and compliance.

1.7.3 Lumped Models

The cardiovascular system can be modelled at various levels of detail. Common divisions are between single- and multicompartment models, and 0D, 1D, 2D and 3D models [25]. 3D models are most exhaustive, and can give detailed information about flow and pressure patterns in all positions in a vessel. It is most commonly used for complex situations such as bifurcations, heart valves or the inside of a ventricle. Flow and pressure along a vessel and their axial distribution can be assessed in 2D models. 1D models only describe flow and pressure through the length of the blood vessel and also wave reflections, whereas 0D models treats the vessel as one single entity with no spatial distribution so that only incoming or outgoing pressure and flow can be surveyed. Models of different dimensions can be combined [eg. 118]. Whereas a single-compartments model portrays the vascular system of interest as a single block, multi-compartment models divides it into several segments.

This project utilises a multi-compartment lumped model, i.e. a 0D model, where the physical properties of a vessel are collected in a single electrical element; vessel resistance is represented by a resistor, vessel compliance is represented by a capacitor, and blood inertia is represented by an inductor. The lumped model approach has a long history and has provided important insights into the functioning of the cardiovascular system.

The Windkessel Model

It is said that Reverend Stephan Hales in 1733 was the first to put forward a model taking into account artery elasticity to describe pressure variations [25], when investigating a mare. He writes [quoted in 119]

> by which curious artifice of nature, the blood is carried on in the finer capillaries, with an almost even tenor of velocity, in the same manner as the spouting water of some fire-engines, is contrived to flow with a more even velocity, notwithstanding the alternate systoles and diastoles of the rising and falling embolus or force; and this by the means of a large inverted globe, wherein the compressed air alternately dilating or contracting, in conformity to the workings to and fro of the embolus, and thereby impelling the water more equably than the embolus alone would do, pushes it out in a more nearly equal spout.

The model got the name Windkessel (German for "air chamber") after the inverted globe containing air used in fire-engine pumps at that time.

Otto Frank offered a mathematical formulation of the theory in 1899 [119]. The capacitor in Figure 1.25a – or the analogous elastic arteries – is filled during systole and acts as a reservoir during diastole [120]. Eq. (1.33) can be solved in terms of pressure instead of current, and predict a diastolic blood pressure

$$\mathrm{DBP}(t) = \mathrm{SBP}_{\mathrm{end}} e^{-t/R_p C_p},$$

as decaying from end-systolic blood pressure (SBP_{end}) with a time constant RC. Frank was able to use measure the RC constant experimentally, and estimated C from pule wave velocity in the aorta. Thus, he was able to calculate cardiac output from Eq. (1.27).

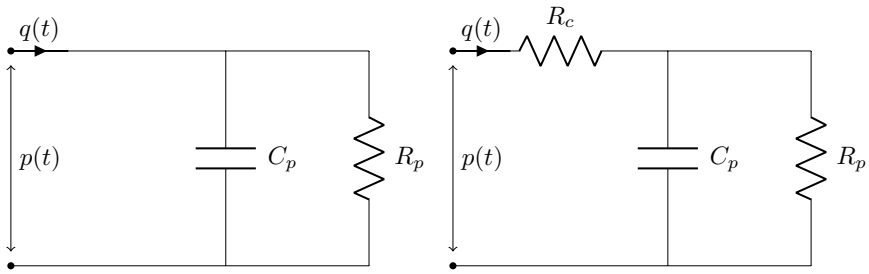

(a) 2-element Windkessel model. **(b)** 3-element Windkessel model.

Figure 1.25: Electrical representation of a 2- and 3-element Windkessel model with central and peripheral resistances R_c and R_p, respectively, and peripheral compliance C_p. Either an inflow $q(t)$ or a driving pressure $p(t)$ can be used as input.

Later, simultaneous flow and pressure measurements became available, showing that the 2-element Windkessel model had significant shortcomings in terms of impedance [120]. In the 2-element Windkessel model, the phase shift between pressure and flow quickly approached a plateau of $-90°$ for increasing frequencies, whereas the measured phase shift only had a temporary decrease in phase, as illustrated in Figure 1.26. This was compensated by adding a characteristic resistance R_c to the model as shown in Figure 1.25b to match the impedance observed in the proximal aorta.

Figure 1.26 demonstrates that the addition of a third element improved the fit to measured values but leaves some high-frequency features unaccounted for [120]. Despite this the modelled wave forms are close to the ones measured. Some of the mismatch may be attributed to the measuring methods used. Several interpretations of R_c in Figure 1.25b exist, as some interprets it as the resistance of conduit arteries whereas others treat it as an impedance (and not a resistor in strict terms).

The addition of R_c caused a larger error in impedance at low frequency, as shown in Figure 1.26 [120]. The effect of inertia can be modelled as an inductor as described above, and adding an inductor as a fourth element has been tried to compensate for the error introduced with R_c. However, inertance is difficult to estimate and some argue that the 3-element Windkessel model is preferable.

Modelling of Tilt

Lumped models have been used to investigate cardiovascular consequences of postural changes and tilt. Mader, Olufsen and Mahdi [121] used a simple mechanical model to simulate sitting-to-standing transition in a young and an elderly person. Four parameters were used to predict cerebral blood flow from the arterial blood pressure, and to compare to Doppler blood flow velocity recorded from the middle cerebral artery. The model was able to recreate several features of the recorded data, and showed a nonlinear relation

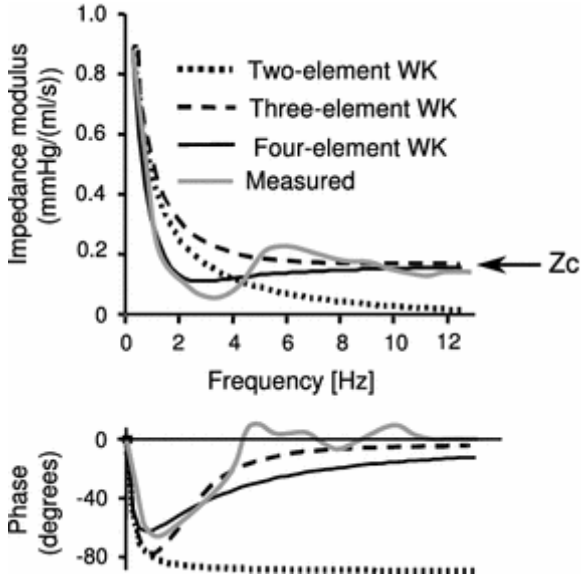

Figure 1.26: 2-, 3- and 4-element Windkessel (WK) models behave different in terms of impedance and phase. Figure by Westerhof, Lankhaar and Westerhof [120], licensed under CC BY-NC 3.0.

between arterial blood pressure and cerebral blood flow. The model did not faithfully predict the observed pulse widening in cerebral blood flow velocity immediately after changing position, which was especially pronounced in the young subject.

Electrical models have also been used. Olufsen, Nadim and Lipsitz [122] used a three-element Windkessel model to assess cerebral resistance during a sitting-to-standing transition. The cerebral resistance was found to initially increase, but decline after approximately 10 seconds. Also this model used arterial blood pressure as input. A widening of the cerebral blood flow velocity pulses was observed after standing up, and it was found to disappear if the initial increase in cerebral resistance was dampened. The model was later developed into a multi-compartment model, including a heart compartment, that did not require pressure as input [123]. Resistance and compliance were governed by pressure dependent differential equations to mimic regulatory mechanisms. Cerebral resistance was calculated separately. The approach is also used in this project, and is further described in section 2.3. The cerebral resistance was found to initially decreas efor 10 seconds, followed by an increase for 5 seconds, and a new steep decrease. It was suggested that the first increase results from autonomic regulation whereas the following decrease is caused by cerebral autoregulation.

The response to graded tilt was modelled by Lim et al. [124]. A steady but nonlinear decrease in cardiac output was found for increasing tilt angles, to about 40% decrease at $90°$ tilt. Heart rate showed the opposite pattern, increasing to about 30% at $90°$ tilt. MAP had a maximal increase at $45°$ of about $4.2\,\mathrm{mmHg}$. High tilt angles contributed to high transmural pressures in the lower body, reducing the compliance and limiting the blood pooling. Cardiopulmonary baroreceptor reflexes contributed at low tilt angles by

increasing systemic resistance. Local responses in the lower body contributed to a higher resistance, redistributing blood away from the lower body, but did not alter global hemodynamics. Despite vaso- and venoconstriction, the splanchnic circulation was seen to fill during upright position.

Modelling of Perinatal Circulation

The unique features of foetal circulation and its transition at birth were reviewed in Section 1.5.1. Specific attention is granted to a model by Garcia-Canadilla et al. [28], described below in Section 1.7.3. Foetal circulation was also modelled by Pennati, Bellotti and Fumero [125], who found good correspondance to Doppler measurements. In the following is a selection of studies investigating perinatal circulation.

Sá Couto et al. [126] published a hydraulic model to investigate cardiovascular pathophysiology in the neonate. Some errors in software implementation were later detected and the model had to be improved [127]. The corrected model was later used to assess the cardiovascular transition during birth and the first few hours of life, and its main results are given in Figure 1.27 [128]. Systemic blood pressure increased while pulmonary blood pressure decreased as the ductus arteriosus closed. Blood flow in the pulmonary artery increased rapidly the first minutes after birth. Only a slight increase in systemic resistance was observed.

The consequence of pulmonary atresia before and after birth was explored by Sanchez-Posada, Torres and Triana [129]. Maldevelopment of the pulmonary valve makes the infant dependent on flow through the ductus arteriosus to connect pulmonary and systemic circulation. Lack of blood pressure measurements and data relating to pulmonary atresia made the validation of the model difficult.

Sudden PDA closure was studied by Soleymani et al. [130] using a multi-compartment lumped model. Left ventricular output was increased immediately following DA closure, with an accompanying increase in systemic blood pressure. A regulatory mechanism was implemented to compensate for the increased blood pressure, lowering heart rate and systemic vascular resistance.

Jennekens et al. [131] developed a simple multi-compartment model to investigate the baroreflex in a preterm infant. Baroreflex regulation was borrowed from a model by Ursino [132] and rescaled for infants. An increase in heart rate was observed experimentally, as well as a decrease in heart rate variability, after atropine administration. This was recreated in the model by blocking parasympathetic activity.

Lampe et al. [133] employed a hierarchical cerebrovascular model to explore autoregulation in the preterm. The cerebral vasculature was divided into 19 compartments representing vessels of different size and coupled through equations under the assumption of Hagen-Poisseuille flow. Autoregulation was implemented with inspiration from Ursino [132], but the results were not experimentally validated.

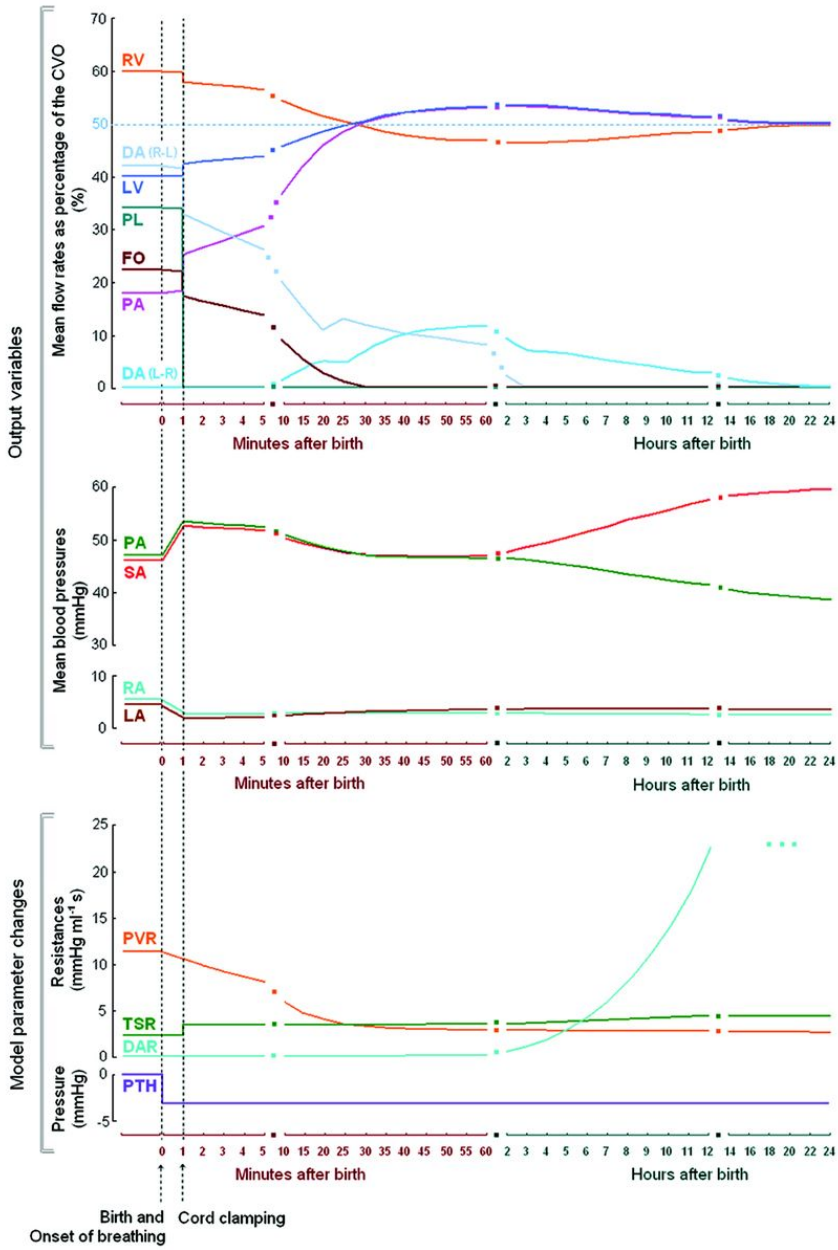

Figure 1.27: The hemodynamic transition at birth and the first hours of life was simulated using an hydraulic model. Abbreviations: RV, right ventricle; DA (R-L), ductus arteriosus (right to left flow); LV, left ventricle; PL, placenta; FO, foramen ovale; PA, pulmonary arterial; DA (L-R), ductus arteriosus (left to right flow); SA, systemic arterial; RA, right atrium; LA, left atrium; PVR, pulmonary vascular resistance; TSR, total systemic resistance; DAR, ductus arteriosus resistance; PTH, mean intrathoracic pressure. Figure by Sá-Couto et al. [128], reprinted with permission from Springer Nature.

A Model for Foetal Circulation

Garcia-Canadilla et al. [28] devised a lumped model to investigate blood redistribution in foetuses with intrauterine growth restriction. The model is shown in Figure 1.28 and consists of 22 compartments, where 14 represent (central) arterial segments and eight (peripheral) vascular beds. The central compartments consisted of a resistor, an inductor and a capacitor as shown in Figure 1.24. Peripheral compartments were equal to the three-element Windkessel model shown in Figure 1.25b. The coronary artery was implemented as a simple resistor. Venous pressure was set to zero so that all the peripheral compartments were connected to ground.

For the central components, resistance was calculated from Eq. (1.22), inductance from Eq. (1.28) and compliance from Eq. (1.32). Values for vessel length, radius and Young's modulus, blood viscosity and density were estimated from literature as a function of gestational age. Wall thickness was assumed to be 15% of vessel radius.

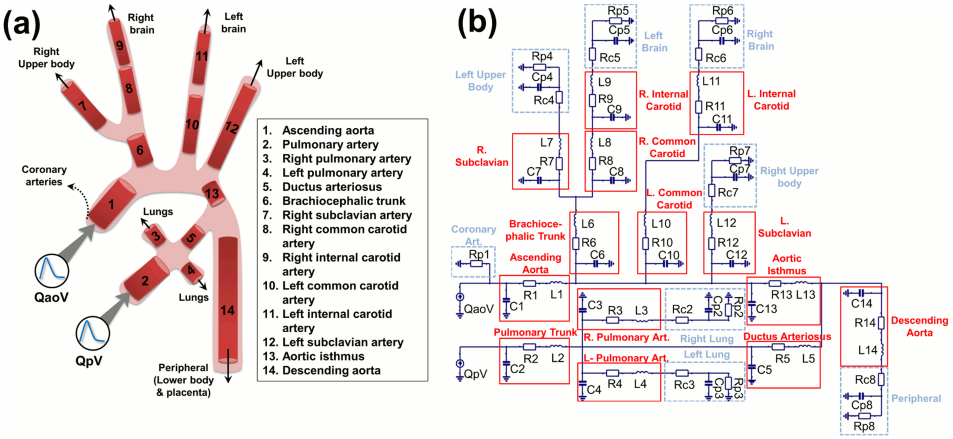

Figure 1.28: A 22 lumped multi-compartments model for foetal circulation. Panel **(a)** shows the anatomical analogues of each compartment shown in panel **(b)**. Central compartments (red) are made of blocks similar to Figure 1.24, whereas the peripheral compartments (dotted blue) are equal to Figure 1.25b. The coronary artery was implemented as a simple resistor. Figure by Garcia-Canadilla et al. [28], licensed under CC BY 4.0.

As the peripheral compartments represents more complex structures, resistance and compliance cannot be calculated as for the central compartments. Resistances were found by first determining the total resistance necessary to reach a MAP of $40\,\mathrm{mmHg}$, corresponding to a 33.2 week old foetus, and adjusting R_p for each compartment so that the amount of blood flow relative to combined cardiac output matched values from the literature. Characteristic resistances, the R_c, were chosen to match the characteristic impedance of the downstream compartment at high frequencies to avoid reflections. Compliance, C_p, was found using an optimisation algorithm minimising the difference between measured and simulated PI in the aorta and cerebral arteries.

The model used blood flow through the pulmonary and aortic valve as inputs, estimated from Doppler measurements. Inflows and simulated wave profiles for several com-

partments, including a pressure wave, are shown in Figure 1.29.

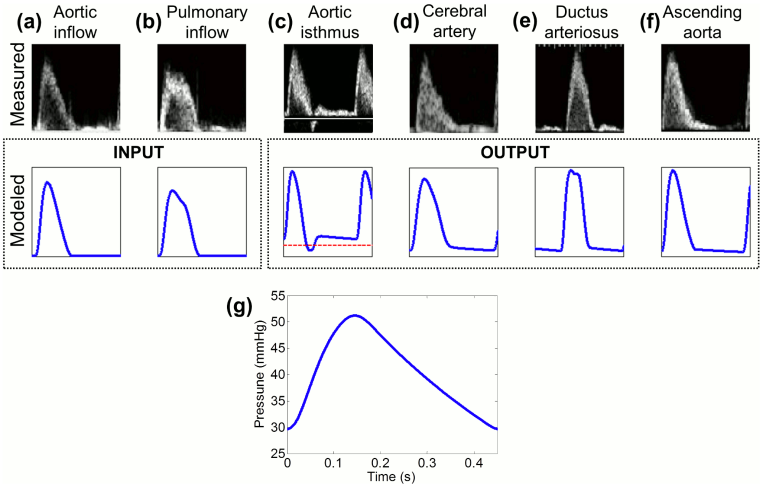

Figure 1.29: The model for foetal circulation used aortic and pulmonary inflows as input (panels **(a)**-**(b)**). Simulation outputs are shown in panels **(c)**-**(f)**. Doppler spectra from the corresponding anatomical locations are shown above. Panel **(g)** shows a simulated pressure wave in the aorta. Figure by Garcia-Canadilla et al. [28], licensed under CC BY 4.0.

A similar model had earlier been used to explore resistance and compliance in relation to Doppler findings in foetuses with intrauterine growth restriction [26].

1.7.4 Simulink and Simscape

Simulink by MathWorks is a programming environment aimed at multidomain modelling and simulation [134]. Simscape is an add-on to Simulink specially designed for the simulation of physical systems [135]. Pre-made blocks, such as electrical components, can be graphically connected into a complex system. The behaviour of standard blocks are already defined, but custom MATLAB functions can also be integrated into the system. A variable resistor can get its time-dependent resistance as a column vector from the MATLAB workspace, or as the output of a custom function. The latter can be used to design a resistance that changes with voltage (or the analogous pressure) upstream or downstream. Voltage and current can be read at both poles of all components, and exported to the MATLAB workspace for further processing and analysis.

A Simscape simulation has six steps [136]. First, the constructed model is validated. This include checking that all components are connected in a meaningful way. Secondly, Simscape constructs a physical network that is used in step three to construct a set of equation to describe the network. The equations contain dynamic and algebraic variables. The first are integral to the time development of the system as the time derivatives of these variables appear in the equations. The latter have no time derivatives but typically arise from conservation laws. Fourth, the initial conditions are computed at simulation time $t = 0$. The initial conditions are prioritised, and if the software is unable to find a

solution for all the high-priority conditions, a warning is issued but the simulation carries on with approximate solutions. Next, “transient initialisation” state and “transient solve” state alternate between calculating temporary sets of initial conditions and how the system of equations develop under these conditions. New initial conditions have to be calculated in the event of a discontinuity or zero crossing. A Solver Configuration block has to be connected to the circuit. Here, parameters related to the solving of differential equations are managed.

Chapter 2

Methods

2.1 Experimental Measurements

A tilt test was performed on newborns at St. Olav's University Hospital in Trondheim, Norway at two consecutive days by trained health care workers. The time course of the test is summarised in Figure 2.1. A NeoDoppler transducer was attached to the infant's head, as illustrated in Figure 1.20a, and the child was observed for 40 seconds before it was lifted by the tester and kept in an upright position into the chest of the tester. After 200 new seconds, the child was laid down and recorded for another 60 seconds. Blood pressure was measured immediately before the experiment and 80 seconds into the tilt ($t = 120\,\mathrm{s}$). Intellivue MP40 Patient Monitor (Phillips) connected to a non-invasive blood pressure measuring module with cuffs of adequate size was used to measure blood pressure. Distance between the head and the heart was measured from the left nipple (*papilla mammaria*) to the top of the head as illustrated in Figure 1.9b.

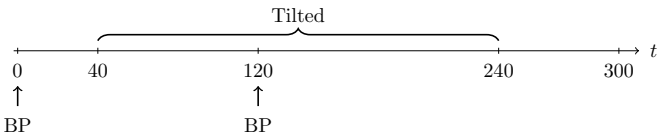

Figure 2.1: Each tilt test consisted of a 300 seconds long NeoDoppler recording. The neonate was tilted after 40 seconds and kept in upright position for 200 seconds. Blood pressure was measured at the beginning of the experiment and after 120 seconds.

Two participants with high-quality recordings were selected for further analysis, and will be referred to as "Joakim" and "Ida." Their birth data are given in Table 3.1.

In addition, Doppler velocity recordings of "Sebastian" were acquired from several locations, including the aortic valve, ascending aorta, and the abdominal aorta. Sebastian was prematurely born at about 28 weeks of gestation, and had an open ductus arteriosus at the time of the recordings. The state of the ductus was not known for Joakim and Ida.

Velocity traces were exported from EarlyBird. Figure 1.21 demonstrates the relation between the Doppler spectrum and the velocity trace. EarlyBird also provided time stamps for the beginning of each heart cycle, which were later used to separate each heart beat for beat-to-beat analysis. HR was calculated as

$$\mathrm{HR}(t_{i,\mathrm{mean}}) = \frac{1}{t_{i,\mathrm{end}} - t_{i,\mathrm{beg.}}},$$

where $t_{i,\mathrm{beg.}}$ and $t_{i,\mathrm{end}}$ are the times of the beginning and end of heart beat number i, and $t_{i,\mathrm{mean}} = (t_{i,\mathrm{beg.}} + t_{i,\mathrm{end}})/2$. PI was found by subtracting the minimum velocity from the maximum velocity within each beat and dividing by the mean velocity of that beat. A moving average over 20 beats was then calculated to avoid distracting beat-to-beat variations.

2.2 Model 1: Steady State Blood Flow in a Neonate

2.2.1 Outline of the Model

The model made by Garcia-Canadilla et al. [28] for foetal circulation, described in section 1.7.3, was adapted to model neonatal circulation. The ductus arteriosus (DA) usually contracts 15 hours after birth [137], and often closes 10–30 hours thereafter [42]. The DA is assumed closed in this projet, thus the pulmonary circulation is isolated from the systemic so that the pulmonary compartments, including the (closed) DA, can be removed without affecting the systemic circulation. This simplified model is shown in Figure 2.3 and was implemented in SIMULINK version 9.1 (R2018a) by MathWorks using the Simscape library (version 4.4).

2.2.2 Inputs

Three different inflows were tested; a sine-shaped inflow q_s, a sine-shaped inflow q_b with backflow, and a inflow q_m based on Doppler measurements. The three wave shapes are shown in Figure 2.2. The first inflow was predefined as a sine-shaped wave in the systole and zero flow in the diastole, that is

$$q_s = \begin{cases} q_s \sin\left(\frac{\pi}{t_s} t\right), & 0 \leq t \leq t_s, \\ 0, & t_s < t < t_c, \end{cases} \tag{2.1}$$

where t_s and t_c are the duration of systole and the total cardiac cycle, respectively. q_s represents peak systolic flow rate, and was scaled to yield targeted stroke volume.

The second inflow was equal to q_s but with the addition of a small sine-shaped backflow at the beginning of diastole as shown in Figure 2.2. The backflow is often observed using Doppler ultrasound as described in section 1.5.1, and was assumed to have a duration at_s, scaled to provide a smooth (i.e. differentiable) transition from positive flow,

$$q_b = \begin{cases} q_{b,1} \sin\left(\frac{\pi}{t_s} t\right), & 0 \leq t \leq t_s, \\ q_{b,2} \sin\left(\frac{\pi}{at_s} t\right), & t_s < t \leq t_s + at_s, \\ 0, & t_s + at_s < t < t_c, \end{cases} \tag{2.2}$$

where t_s and t_c are the duration of systole and one cardiac cycle as before, and $q_{b,1}$ and $q_{b,2} = -aq_{b,1}/\cos(\pi/a)$ are peak flows. Here, fractional backflow duration $a = 1/6$ was used, yielding $q_{b,2} = -0.17q_{b,1}$. This is the same fractional duration and approximately the same amplitude as used by Politi et al. [48], who thought these were probably overestimates. In the lack of data for neonates, their values were used unaltered.

The final inflow q_m was found by extracting a single heart beat from Doppler measurements of the blood flow velocity through the aortic valve of the pre-term infant Sebastian introduced in the previous section. The measurements were performed by Martin Leth-Olsen using a Vivid E9 ultrasound system (GE Vingmed Ultrasound), and the wave profile extracted using the software Cardiac Work (made by H. Torp). Drift correction was applied by subtracting a linearisation of the difference between the end and the beginning of

the signal. In addition, the diastolic part of the signal was set to zero, and the heart beat was stretched to a duration $t_c = 1/\text{HR}$. The signal was rescaled as one entity, so that the relative length of systole and diastole was kept unaltered. The first two inflow signals, q_s and q_b, were not directly based on measurements, hence the relative systolic duration was calculated from Eq. (1.3).

All inflows were scaled so that the stroke volume

$$\text{SV} = \int_0^{t_c} q \, \mathrm{d}t$$

matched reference values (See Table 3.2). For q_s and q_b this yield

$$q_s = \frac{\text{SV} \cdot \pi}{2t_s}, \tag{2.3}$$

$$q_{b,1} = \frac{\text{SV} \cdot \pi}{2(1-a^2)t_s}. \tag{2.4}$$

The single beats shown in Figure 2.2 were repeated to form an input signal of the length of the simulation, $t_{sim} = 60\,\text{s}$.

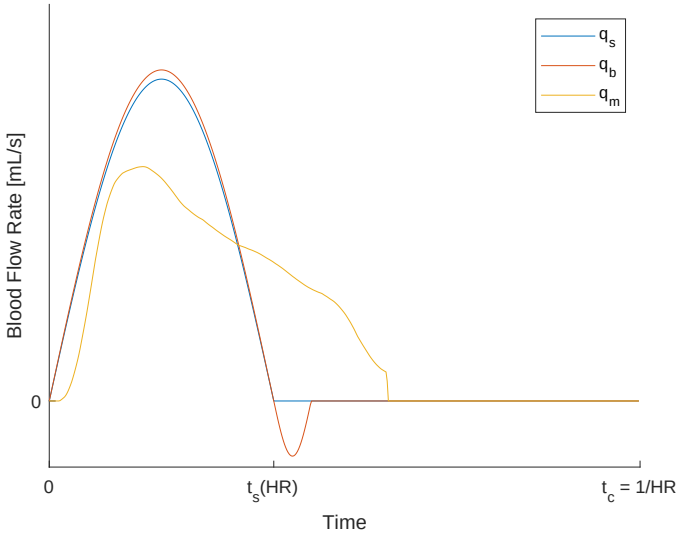

Figure 2.2: Three different inputs were used; a sine-shaped wave (q_s) defined in Eq. (2.1), a wave with backflow (q_b) defined in Eq. (2.2), and a wave found from Doppler velocity measurement of the aortic valve (q_m). All the inflows have been scaled to yield an adequate stroke volume. The duration of systole relative to the total cardiac cycle, t_s/t_c, for q_s and q_b was calculated from Eq. (1.3), and the backflow in q_b spans 1/6 of t_s. For q_m, the relative length of systole was kept as measured.

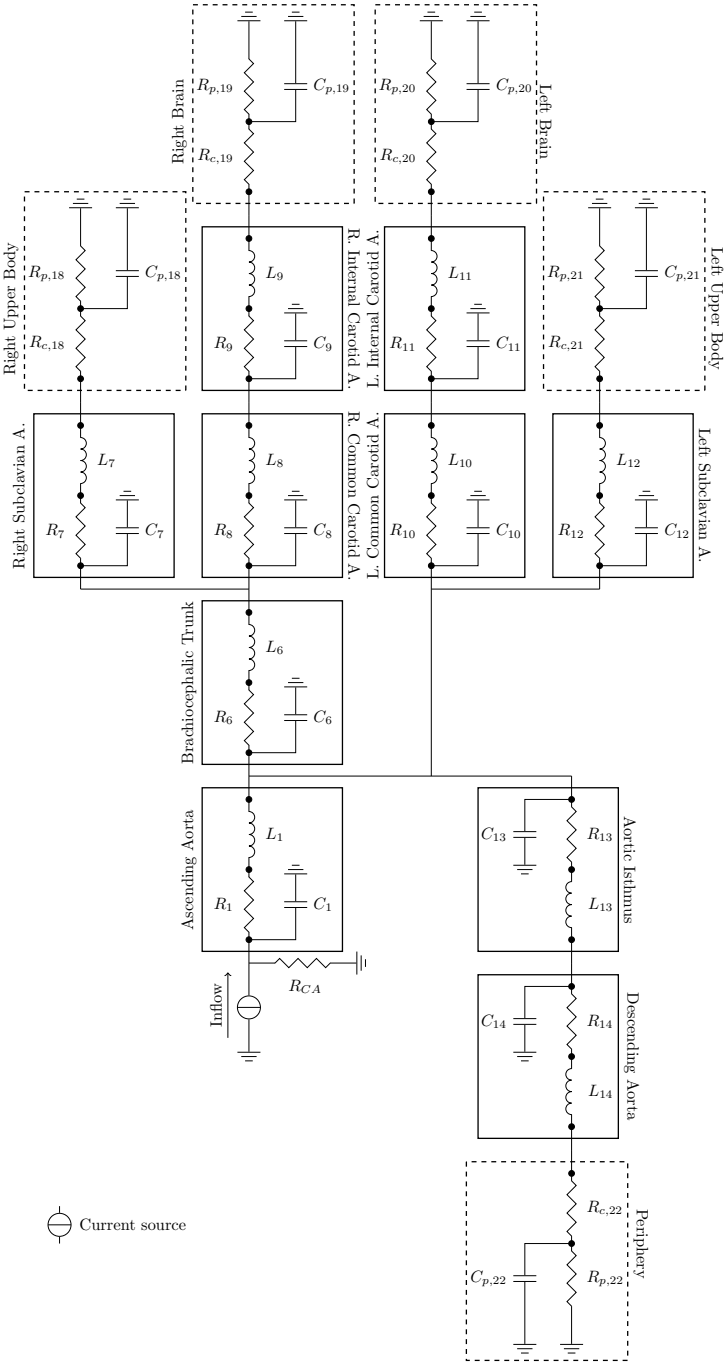

Figure 2.3: A lumped model with 15 compartmens, adapted from a model of foetal circulation [28]. Central compartments consist of a resistor R, inductor L and capacitor C, whereas the peripheral compartments have two resistors and a capacitor.

2.2.3 Parameter Estimation

Resistance, inductance and compliance in central compartments were calculated for a foetus at 41 weeks of gestation using the estimates by Garcia-Canadilla et al. [28]. The equations are derived in section 1.7.1. The central compartments were working as resonance circuits, producing oscillations as predicted by Eq. (1.34). To remove the oscillations, all Ls were decreased by a factor 1000. This solution was also applied by Garcia-Canadilla et al. [28] (Patricia Garcia-Cañadilla, personal communication, April 4, 2019). Other parameters were scaled to reach targeted pressure, flow distribution and cerebral PI from the tilt experiment. q_b was used as input when the parameters were estimated, and the parameters are listed in Table 2.1 next to the values provided by Garcia-Canadilla et al. [28].

2.2.4 Analysis

Flow rates were read through R in central compartments and over R_c in peripheral compartments. Pressures were extracted from the same components, and measured as the proximal end relative to ground.

All statistics were calculated from the second half of the simulation time to ensure that only steady-state results were included. Figure 2.4 demonstrates that the simulation reached steady-state after about $4\,\mathrm{s}$. Maximum and minimum pressures in the ascending aorta were regarded as systolic and diastolic pressure, respectively. Cardiac output (CO) was calculated as

$$\mathrm{CO} = \mathrm{SV} \cdot \mathrm{HR}, \tag{2.5}$$

where SV is stroke volume and HR is heart rate, and blood flow distribution was found by dividing mean flow rate in a compartment by CO.

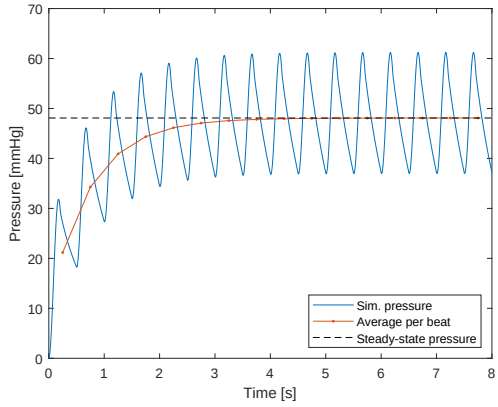

Figure 2.4: The first few seconds of the simulation are used to reach steady-state pressure and flow. Averaged arterial pressure per heart beat reaches the steady-state pressure after approximately 4 seconds. q_b is used as inflow, but the trend is similar for the other inflows.

2.2.5 Simscape Settings

Simscape offers several settings related to the simulation. These are set in the Configuration Parameters menu. The automatic solver selection was used instead of specifying a particular method to solve the differential equations. Variable-step was chosen instead of fixed-step. Absolute and relative tolerance were 1×10^{-3} and 1×10^{-6}, respectively. "Auto scale absolute tolerance" was checked. "Log simulation data" was set to all, and the no limit was set to the number of data points.

Standard settings were used for the Solver Configuration Block. That includes a consistency tolerance of 1×10^{-9}, applying filtering at 1-D/3-D connections when needed, delay memory budget of 1024 kB, and a filtering time constant of 0.001. Other options were not applied.

Table 2.1: Component values for each compartments in the circuit shown in Figure 2.3. The original values from Garcia-Canadilla et al. [28] have been adapted to fit measured data from Joakim as described in the text. R in $\mathrm{mmHg\,s\,mL^{-1}}$, L in $\mathrm{mmHg\,s^2\,mL^{-1}}$, and C in $\mathrm{mL\,mmHg^{-1}}$.

Compartment	Adapted to Joakim			Garcia-Canadilla et al. [28]		
	R	L	C	R	L	C
Ascending Aorta	1.76×10^{-2}	2.50×10^{-5}	5.47×10^{-2}	5.48×10^{-3}	3.42×10^{-3}	3.09×10^{-2}
Brachiocephalic Trunk	2.47×10^{-2}	1.91×10^{-5}	1.30×10^{-2}	1.42×10^{-2}	3.46×10^{-3}	4.74×10^{-3}
R. subclavian artery	1.36×10^{-1}	1.01×10^{-4}	1.02×10^{-3}	1.07×10^{-1}	1.13×10^{-2}	2.47×10^{-3}
R. Common Carotid artery	3.30×10^{-1}	1.42×10^{-4}	2.41×10^{-3}	1.93×10^{-1}	2.68×10^{-2}	9.84×10^{-3}
R. Internal Carotid Artery	2.23	4.67×10^{-4}	2.46×10^{-3}	5.24×10^{-1}	4.40×10^{-2}	3.99×10^{-3}
L. Common Carotid Artery	3.30×10^{-1}	1.41×10^{-4}	2.41×10^{-3}	2.26×10^{-1}	3.13×10^{-2}	1.15×10^{-2}
L. Internal Carotid Artery	2.23	4.67×10^{-4}	2.46×10^{-3}	5.24×10^{-1}	4.40×10^{-2}	3.99×10^{-3}
L. subclavian artery	1.11×10^{-1}	5.64×10^{-4}	5.74×10^{-4}	1.07×10^{-1}	1.13×10^{-2}	2.47×10^{-3}
Aortic Isthmus	2.35×10^{-2}	1.55×10^{-5}	4.39×10^{-3}	7.17×10^{-3}	1.96×10^{-3}	3.37×10^{-3}
Descending Aorta	2.42×10^{-2}	2.75×10^{-4}	7.50×10^{-2}	6.77×10^{-2}	2.43×10^{-2}	6.03×10^{-2}
	R_p	R_c	C_p	R_p	R_c	C_p
Coronary artery	5.26×10^{1}	–	–	6.88×10^{1}	–	–
Right upper body	3.55×10^{1}	2.31×10^{1}	1.92×10^{-2}	4.64×10^{1}	–	1.21×10^{-2}
Right brain	3.24×10^{1}	4.32×10^{1}	3.44×10^{-3}	3.39×10^{1}	–	1.04×10^{-2}
Left brain	3.24×10^{1}	4.32×10^{1}	3.44×10^{-3}	3.39×10^{1}	–	1.04×10^{-2}
Left upper body	3.55×10^{1}	2.31×10^{1}	1.92×10^{-2}	4.64×10^{1}	–	1.21×10^{-2}
Peripheral	2.15	3.78	5.25×10^{-2}	3.75	–	6.02×10^{-2}

2.3 Model 2: Tilt Test

This model builds upon the steady-state model presented in Section 2.2 by adding regulatory mechanisms and a time course similar to the experimental tilt tests. A time dependent voltage is added at different locations to simulate the gravitational pressure generated by the tilt. The resulting circuit is shown in Figure 2.6.

2.3.1 Outline of the Model

Three independent regulatory mechanisms were added to Model 1 based on works by Olufsen, Tran and Ottesen [123] and Danielsen and Ottesen [138]; one for the brain compartments, one for the other peripheral compartments, and one for HR. Two voltage sources were added, one above and one below the internal carotid artery on each side, each accounting for half the pressure added by gravity during tilt, $P_g/2$. A fifth voltage source was added distal to the descending aorta, adding a full pressure P_g. A voltmeter was added above the lower of the two sources and connected to a low-pass filter with cut-off frequency $0.5\,\mathrm{Hz}$, at the position of *sinus caroticus*.

The pressure added during tilt was implemented as a split function,

$$P_g(t) = \begin{cases} 0, & t < t_\uparrow, \\ P_g(h)[\sin(\pi(t-t_\uparrow)/t_{\text{tilt}} - \pi/2) + 1]/2, & t_\uparrow < t < t_\uparrow + t_{\text{tilt}}, \\ P_g(h), & t_\uparrow + t_{\text{tilt}} < t < t_\downarrow, \\ P_g(h)[\sin(\pi(t-t_\downarrow)/t_{\text{tilt}} - \pi/2) + 1]/2, & t_\downarrow < t < t_\downarrow + t_{\text{tilt}}, \\ 0, & t > t_\downarrow + t_{\text{tilt}}, \end{cases} \tag{2.6}$$

where the child is tilted upwards at time $t = t_\uparrow$ and down again at $t = t_\downarrow$, with a tilt duration t_{tilt} both ways. $P_g(t)$ is illustrated by Figure 2.5. $P_g(h)$ was defined in Eq. (1.4). The tilt duration was assumed to be $t_{\text{tilt}} = 1\,\mathrm{s}$.

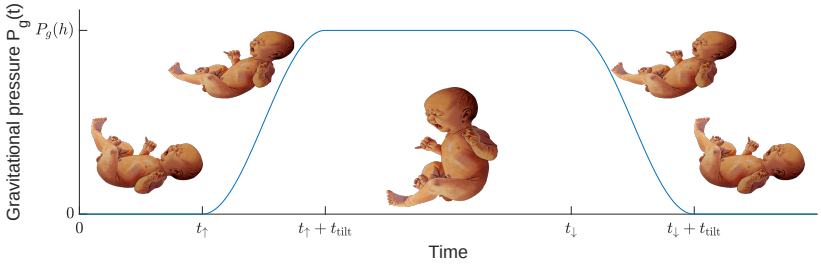

Figure 2.5: As the child is tilted at time $t_\uparrow$, the pressure difference between heart and brain increases as a sine function until upright position is reached after time t_{tilt}. The opposite happens when the child is laid down at time $t_\downarrow$. Eq. (2.6) describes the course of these events.

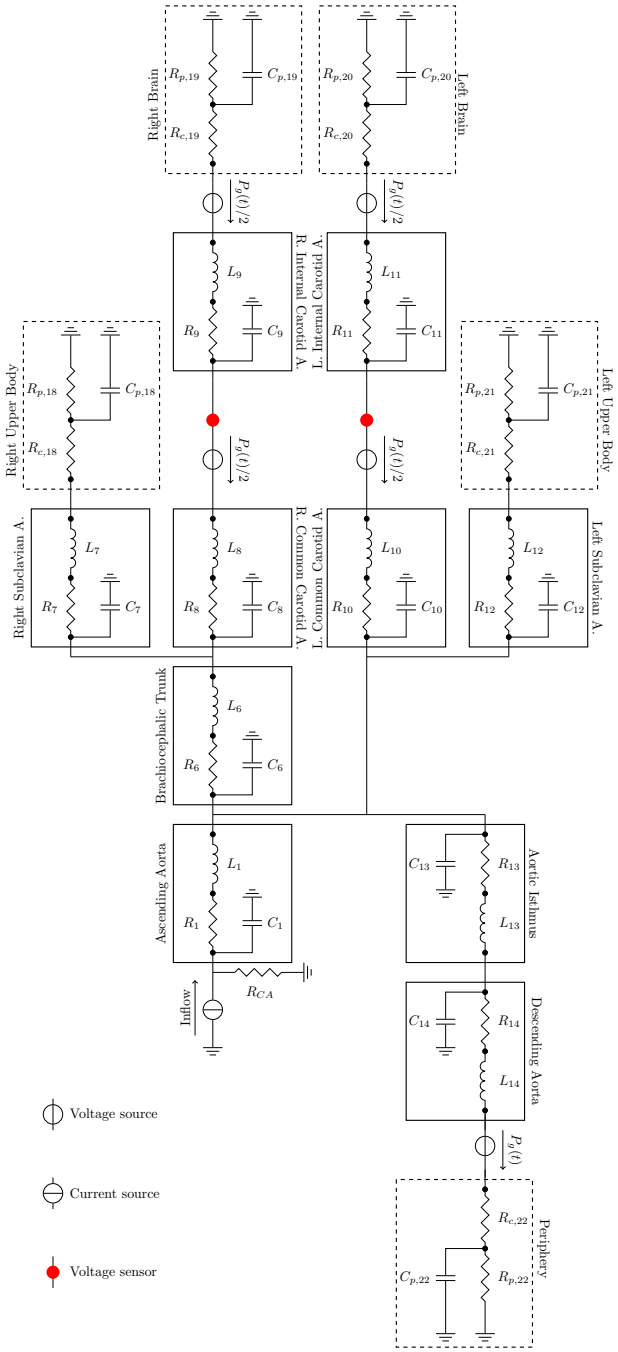

Figure 2.6: The circuit used in Model 1 (Figure 2.3) was modified by adding five voltage sources and two voltage sensors. Also, the resistance and capacitance in each compartment were now time dependent and regulated as described in the text.

Peripheral Regulation

Peripheral and cerebral resistance are regulated by different mechanisms as described in Section 1.5.2. Therefore, they will be treated separately in the model. Less is known about compliance, and the compliance in all peripheral compartments was regulated in parallel with the peripheral resistance but with smaller changes. Hence, peripheral resistance R_p, except for the brain compartments, and peripheral compliance C_p, including the brain compartments, were governed by the differential equation

$$\tau \frac{\mathrm{d}x(t)}{\mathrm{d}t} = -x(t) + (x_{\max} - x_{\min}) \frac{p_0^k}{p(t)^k + p_0^k} + x_{\min}, \tag{2.7}$$

where x is the controlled parameter, p the pressure in the carotid bifurcation, k defines steepness and τ the time needed to obtain full effect. Resistance, compliance and inertia were kept constant in central compartments. $x_{\max}$ and $x_{\min}$ are the limits of the parameter, and p_0 represents the set point pressure at which the parameter has value $(x_{\max} + x_{\min})/2$. If $x_{\max}$ and $x_{\min}$ are expressed in terms of a set point value x_{set}, i.e. $x_{\max} = x_{\text{set}} x_f$ and $x_{\min} = x_{\text{set}}/f$, the parameter x will approach the value $x'_{\text{set}} = x_{\text{set}}(f + 1/f)/2$ at $p = p_0$. p_0 was set to $45\,\mathrm{mmHg}$. Figure 2.7 demonstrates how k and τ both determine to what extent the parameter x is changed. A high k and low τ will give a large and immediate response to a small change in pressure. As τ is increased, a longer time is needed to reach the same value of x. If k is increased, on the other hand, less deviation from $p(t)/p_0 = 1$ is needed for a large change in x to occur. In the simulation, $p(t)$ is affected by the alternation of x, and the behaviour of Eq. (2.7) becomes more complex.

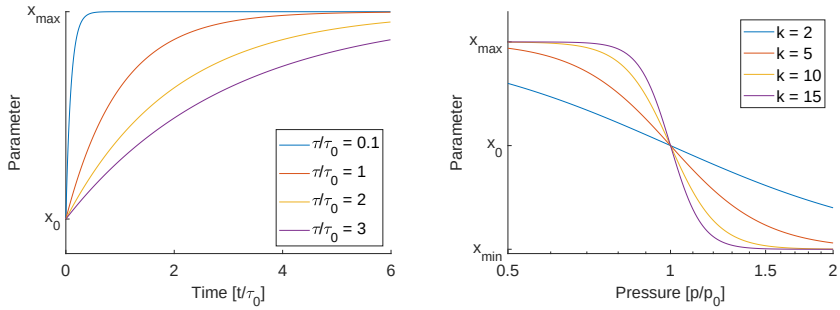

(a) Maximal or minimal effect is reached faster with a lower time constant τ.

(b) With increasing k, less deviation from the reference pressure p_0 is needed provoke maximal or minimal effect.

Figure 2.7: The two parameters k and τ define the steepness of the differential equation governing the peripheral response to pressure drop as function of time, and deviation from the reference pressure.

Cerebral Regulation

An optimisation algorithm was used to assess brain resistance. As this resistance is controlled by both baroreflex and autoregulation, a simple expression such as Eq. (2.7) is not available [123]. The time course of the experiment was divided into n equal segments, and the resistance was estimated for each time segment independently as a time dependent scaling factor $S_R(t)$ so that the resistance in each compartment was $R(t) = S_R(t)R_0$. The difference between the modelled output and the measured data was found by calculating the measured mean flow velocity $\bar{v}_m(t_i, t_{i+1})$ and simulated mean flow rate $\bar{q}_s(t_i, t_{i+1})$ in the time segment spanning from t_i to t_{i+1} and dividing by the average before the tilt,

$$\epsilon = \frac{\bar{v}_m(t_i, t_{i+1})}{\bar{v}_m(0, t_\uparrow)} - \frac{\bar{q}_s(t_i, t_{i+1})}{\bar{q}_s(0, t_\uparrow)}. \tag{2.8}$$

Figure 2.8 demonstrates how the flow velocity data deviates from the pre-tilt mean using $n = 10$ different time segments. If the resistance in the model was too high in the segment,

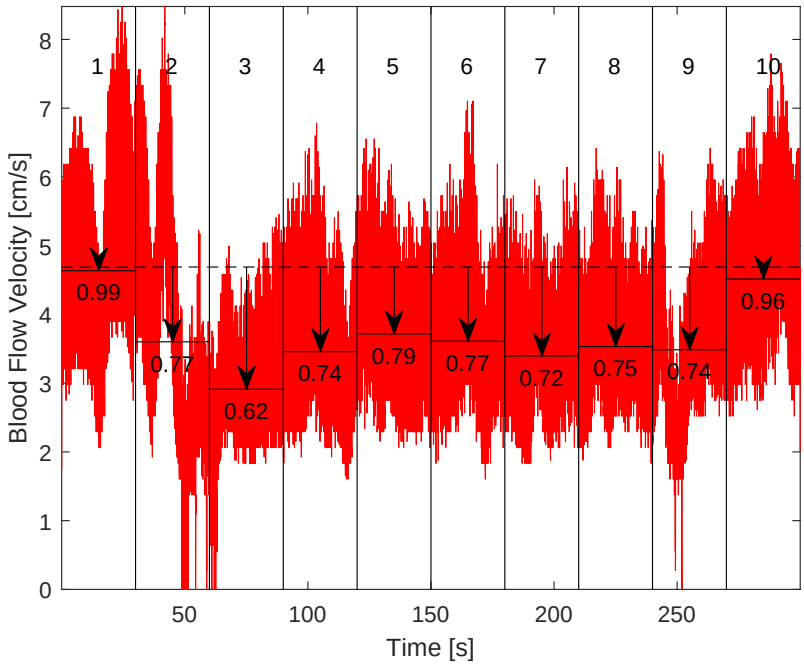

Figure 2.8: A NeoDoppler recording of Joakim is divided into 10 time segments as numbered at the top of the figure. The average velocity before the tilt ($\bar{q}_m(0, t_\uparrow)$) is shown as a dashed line. For each time segment, the average velocity ($\bar{v}_m(t_i, t_{i+1})$) was calculated and plotted as a line spanning the segment and highlighted by arrows. Finally, the ratio between each segment average and the pre-tilt average ($\bar{v}_m(t_i, t_{i+1})/\bar{v}_m(0, t_\uparrow)$) was found. The ratio for each segment is printed as the lower number in each segment.

the relative drop in flow rate would be higher than in the measured data, ϵ would become

negative, and $S_R(t_i, t_{i+1})$ should be reduced to compensate for this. $S_R(t_i, t_{i+1})$ was therefore found by iteration,

$$S_R^{j+1}(t_i, t_{i+1}) = S_R^j(t_i, t_{i+1}) \cdot (1 + \epsilon),\ j \geq 1, \tag{2.9}$$

$$S_R^1(t_i, t_{i+1}) = 1. \tag{2.10}$$

Piecewise cubic hermite interpolating polynomials (implemented in MATLAB as PCHIP) were used to smooth the transition from one time segment to the next. The process is illustrated in Figure 2.9 for the signal and segmentation in Figure 2.8. An interpolated line through $(S_R^j - 1) \cdot 100\%$ for $j \in \{1, 4, 7, 10\}$ is shown in the figures to the left, and the resulting flow rates in the figures on the right. Note how the interpolation provides a continuous, smooth curve connecting the value for each discrete time segment.

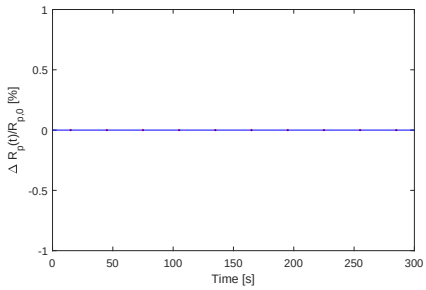

(a) First iteration.

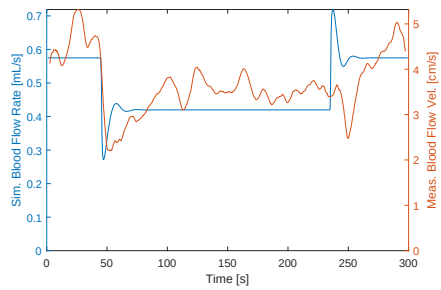

(b) First iteration — resulting flow rate.

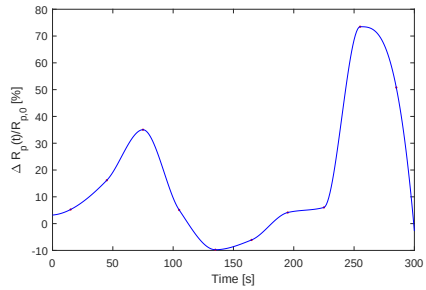

(c) Fourth iteration.

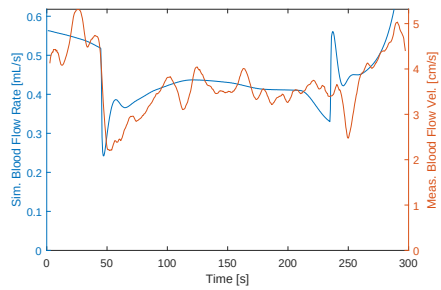

(d) Fourth iteration — resulting flow rate.

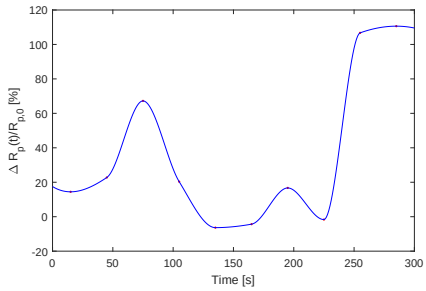

(e) Seventh iteration.

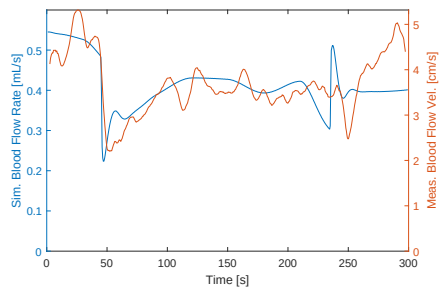

(f) Seventh iteration — resulting flow rate.

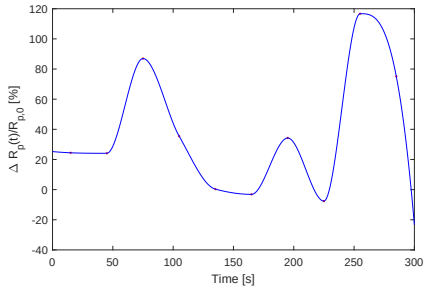

(g) Tenth iteration.

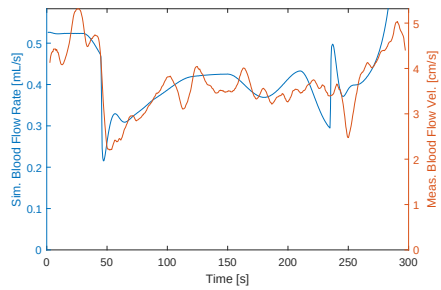

(h) Tenth iteration — resulting flow rate.

Figure 2.9: Cerebral resistance is estimated by iterations as described in the text. The figures to the right shows the resulting flow rate (blue) when cerebral resistance was scaled by the resistance to the left. Red dots shows the middle of each time segment, and the blue line is acquired by interpolation. Recorded NeoDoppler in orange.

Heart Rate Regulation

Danielsen and Ottesen [138] describe a model for baroreflex control incorporating both sympathetic, n_s, and parasympathetic, n_p, activity. The baroreceptors are described in Section 1.5.2. In this model, sympathetic activity is induced mainly when the pressure registered in the baroreceptors, $p(t)$, is low compared to a reference level, p_0. Similarly, the parasympathetic activity increases when the pressure rises above p_0. This can be described by

$$n_s(p(t)) = \frac{1}{1 + \left(\frac{p(t)}{p_0}\right)^{\eta}}, \qquad n_p(p(t)) = \frac{1}{1 + \left(\frac{p(t)}{p_0}\right)^{-\eta}}, \tag{2.11}$$

where $p(t)$ is the level registered by the baroreceptors, p_0 is the reference value of the baroreceptor, and η describes how quickly the activity rises as response to increased or decreased pressure. HR is dependent of both n_s and n_p,

$$\tau_{\text{HR}} \frac{\mathrm{dHR}(t)}{\mathrm{d}t} = -\mathrm{HR}(t) + \alpha_{\text{HR}} n_s(p(t)) - \beta_{\text{HR}} n_p(p(t)) + \gamma_{\text{HR}}, \tag{2.12}$$

where α_{HR} and β_{HR} weights the influence of n_s and n_p, respectively. γ_{HR} equals heart rate in steady-state $\left(\frac{\mathrm{dHR}(t)}{\mathrm{d}t} = 0\right)$, when $\alpha_{\text{HR}} n_s(p(t)) = \beta_{\text{HR}} n_p(p(t))$. τ_{HR} is a time constant affecting how quickly the maximum response is reached. The reference level was set to $p_0 = 45\,\mathrm{mmHg}$.

2.3.2 Tilt with Only Partial Regulation

To explore how failing regulatory mechanisms affect cerebral blood flow, each of the three mechanisms was disabled alone and in combination as shown in Table 2.2. In the absence of regulation, the corresponding variable (peripheral resistance and compliance, cerebral resistance, or heart rate) was kept fixed throughout the simulation.

Table 2.2: Eight cases were simulated with different combinations of regulatory mechanisms present. Cerebral compliance is included in the peripheral regulation, whereas cerebral resistance was regulated by itself.

Case #	1	2	3	4	5	6	7	8
Cerebral regulation	+	+	−	−	+	+	−	−
Peripheral regulation	+	−	+	−	+	−	+	−
HR regulation	+	+	+	+	−	−	−	−

2.3.3 Inputs

The sine-shaped wave with backflow q_b, as defined in Eqs. (2.2) and (2.4), was used as aortic inflow. Eq. (1.3) defined the relative systolic length. Stroke volume was assumed to change with HR according to Eq. (1.2). Figure 2.10 shows input flow for increasing heart rate.

Heart Rate as Input

Since heart rate varied wildly, a simulation was carried out with heart rate as input. Instead of using a set heart rate or subjugate heart rate to the baroreflex, heart rate was abstracted from the NeoDoppler recordings and used to make sine-shaped waves with backflow. Eq. (1.3) still defined the relative length of systole.

2.3.4 Parameter Estimation

As this model builds on Model 1, the parameters listed in Table 2.1 were used as set point values x'_{set}. To allow the model to reach steady-state, an offset $t_{\text{offset}} = 90\,\text{s}$ was added to the beginning of the simulation time and subsequently removed before analysis.

2.3.5 Analysis

Flow rate and pressure were read as in Model 1. When comparing to experimental tilt recordings, were heart beats with duration less than $300\,\text{ms}$ (corresponding to above 200 beats per minute) excluded. Effective flow cross-section was calculated by interpolating the simulated cerebral flow rate at the time points of the NeoDoppler recording, then pointwise dividing the former by the latter, and multiplied by 2. It follows from Eq. (1.21) that the result is the cross-section of a vessel with flow rate q, which is simulated, and peak flow velocity $V_z(0)$ which is measured with Doppler ultrasound. Average and standard deviation were found by considering all the resulting points.

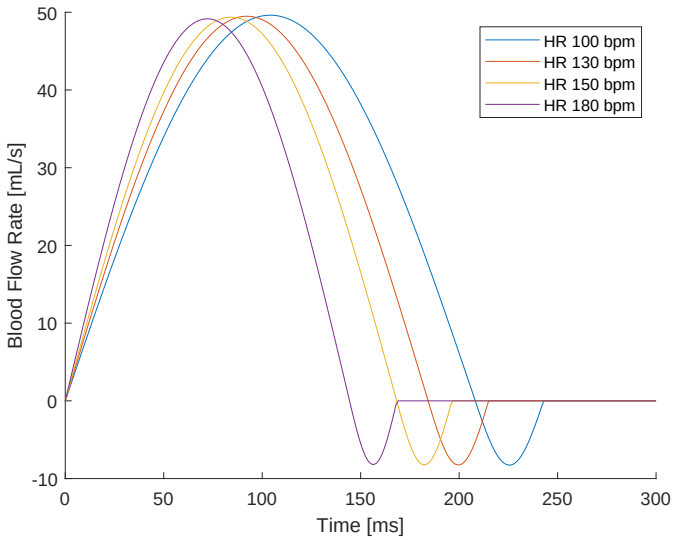

Figure 2.10: Input flow at increasing heart rate for Joakim. Peak flow rate is approximately constant. The diastolic part of the waves is cropped.

Moving average over 10 heart beats was used to smooth beat-to-beat variation for plots showing the time course of the simulations.

2.3.6 Simscape Settings

Simscape settings were kept as for Model 1. Variable capacitors can be governed by to different equations in Simscape, and the equation

$$I = C\frac{\mathrm{d}V}{\mathrm{d}t} + V\frac{\mathrm{d}C}{\mathrm{d}t}$$

was chosen.

2.4 Ethics and Approvals

This project involved analysis of data from underage patients. The measurements and tilt testing were performed by trained personnel as a part of the project 'Neo-Doppler – A new sensor for continuous monitoring of cerebral circulation in neonates,' approved by REK Midt (ref. nr. 2017/314). Informed consent was given by the parents.

Chapter 3

Results

3.1 Experimental Measurements

Seven tilt experiments with NeoDoppler recording were chosen for further analysis. Figure 3.1 shows the course of each experiment in terms of flow velocity, HR and PI, and mean values before (–), during (↑) and after (↓) the tilt are shown in Figure 3.2, in addition to measured BP.

All the children experienced a drop in mean flow velocity within 20 seconds of the tilt. Approximately pre-tilt levels of mean flow velocity were achieved within 20 seconds from the tilt in four of the experiments, and in all but Joakim (Exp. 7) within 30 seconds. Joakim reached pre-tilt levels only a few seconds before the end of the recording, that is about 50 seconds after being laid down.

Anthony, Evans and Levene [24] categorised the tilt responses in cerebral blood flow velocity into four groups as described in Section 1.5.3. In this system, the response of Joakim is likely to be described as uniphasic, whereas Ida showed a biphasic response both days. Also experiment 4 reveals a biphasic response. Exp. 1–3 show a delayed fall in flow velocity.

Exp. 1 was performed early in the study period, and lacked BP measurements. Birth data is given in Table 3.1 for convenience. The recording was also terminated when the child was laid down. MAP decreased from pre-tilt to tilt in three of the experiments, showed a large increase in one experiment, and only minor increase in two experiments.

Table 3.1: Two NeoDoppler recordings were chosen for further analysis, and the neonates involved were named "Ida" and "Joakim." Abbreviations: GA, gestational age; HH, head-heart.

Name	GA at birth	Birth weight	Age at tilt test	HH distance	Sex
Ida	week 39^{+3}	4145 g	10 h at first exp.	18 cm	Female
Joakim	week 40^{+6}	3330 g	33 h	21 cm	Male

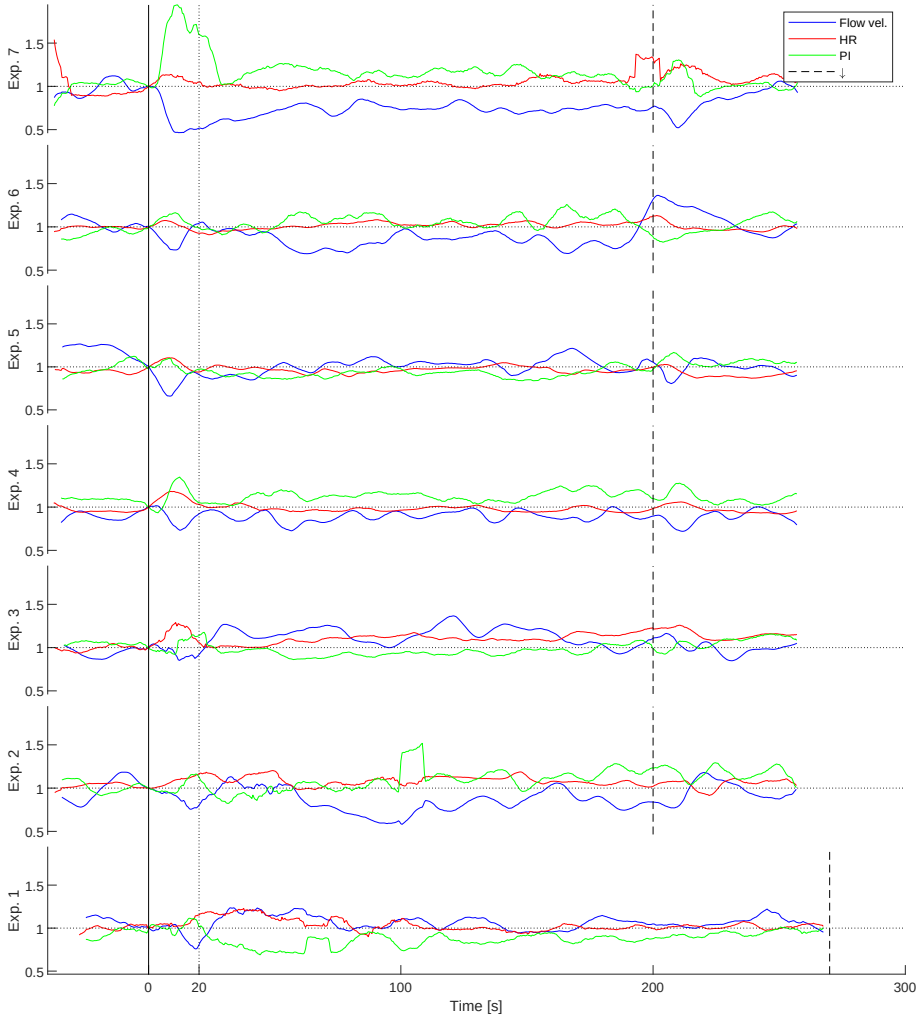

Figure 3.1: Seven tilt experiments are shown, with the tilt occurring at $t = 0$. The dashed lines show when the child is laid down again. Flow velocity (blue), HR (red) and PI (green) have been normalised to 1 at the time of the tilt. Experiment 7 was performed with Joakim, whereas Ida participated in experiment 5 and 6 which were conducted on two successive days. Values averaged over 20 beats.

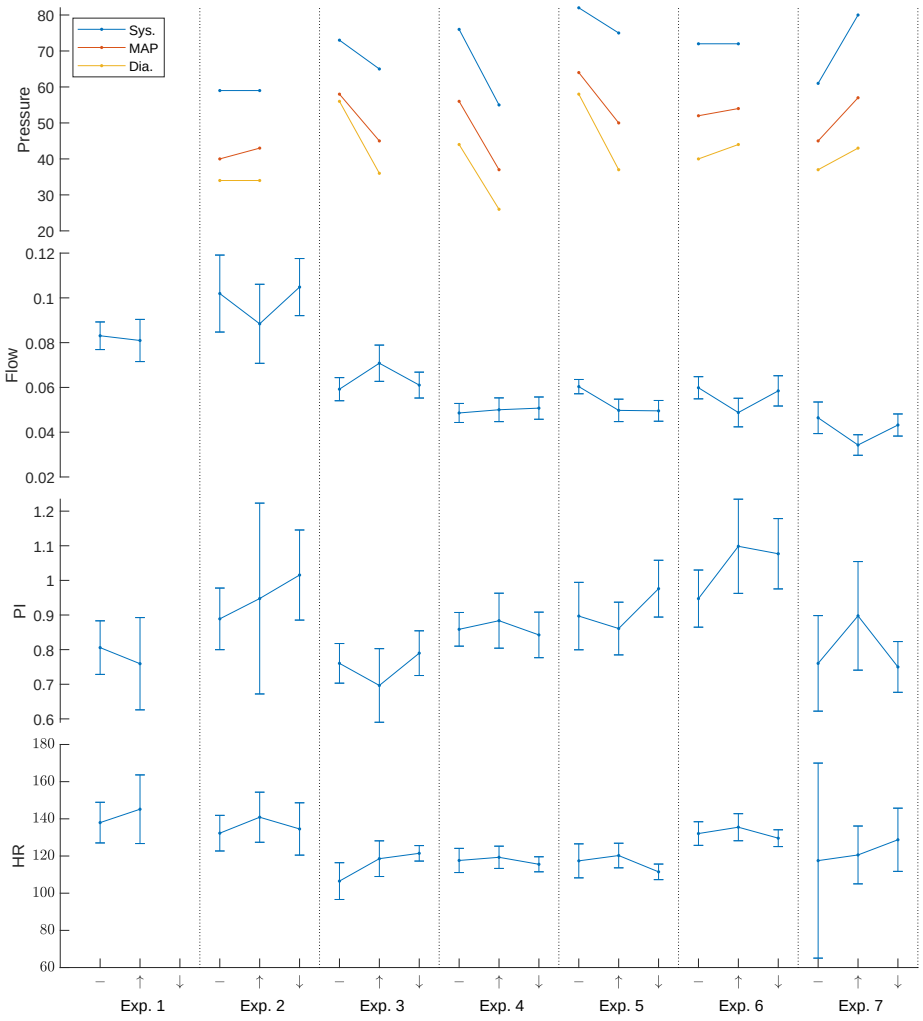

Figure 3.2: Mean values before (–), during (↑) and after (↓) the tilt. The course of each experiment is shown in Figure 3.1. Five seconds prior to, and fifteen seconds following, the tilt and the tilt back were excluded from the calculation. Error bars represents standard deviation. Experiment 7 was performed with Joakim, whereas Ida participated in experiment 5 and 6, which were conducted on two successive days. BP was measured at the beginning of the experiment and after 120 seconds. Exp. 1 lacked BP measurement and post-tilt recording.

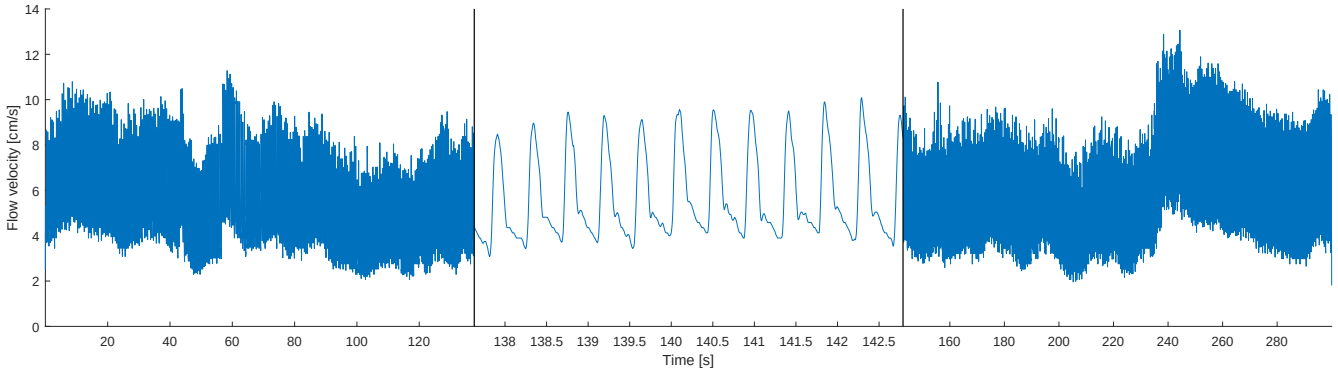

(a) Ida

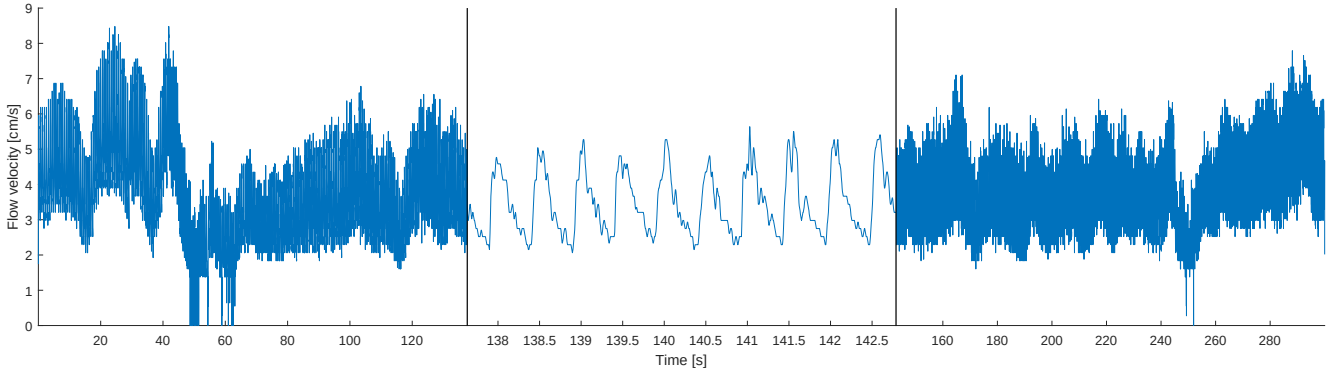

(b) Joakim

Figure 3.3: NeoDoppler recordings of Ida and Joakim during a tilt experiment. They were tilted after approximately 40 seconds ($t = 40\,\mathrm{s}$), and laid down again after approximately 200 seconds ($t = 240\,\mathrm{s}$). Note that the time axes have been stretched to exhibit the wave profiles.

3.2 Model 1: Steady State Blood Flow in a Neonate

The model described in section 2.2 was used to simulate blood flow in an infant using Joakim as template. Three different inflows were used, as shown in Figure 2.2, resulting in three distinct simulated wave shapes as illustrated in Figure 3.4. q_s and q_b produced very similar wave profiles for both pressure and flow, whereas the experimentally derived inflow q_m generated wider and less pulsatile waves. All inflows resulted in non-zero flow during diastole in the ascending aorta.

Figure 3.4 also demonstrates a change in phase from the ascending aorta to the brain compartment. In the ascending aorta, there was a $72\,\mathrm{ms}$ time lag between peak pressure and peak flow rate compared to $15\,\mathrm{ms}$ in the brain compartments for q_b.

In Figure 3.5 the simulated flow using q_b is compared to Doppler and NeoDoppler recordings from Sebastian and Joakim. The change in wave shape between compartments varies. Peak flow rate shrinks from the ascending aorta to the aortic isthmus, whereas the wave shape is preserved. The descending aorta is connected directly to the aortic isthmus, but both wave shape and peak flow rate change significantly.

Table 3.2 shows some important outcomes of the simulations compared to targeted reference values. Heart rate, stroke volume, cardiac output and the amount of blood distributed to the brain, were similar for all inflows. Although all inflows had MAP $48\,\mathrm{mmHg}$, PIs ranged from 0.46 to 0.68, with q_b yielding the highest PI and q_m the lowest. Pulse pressures were $23\,\mathrm{mmHg}$, $24\,\mathrm{mmHg}$ and $17\,\mathrm{mmHg}$ for q_s, q_b and q_m, respectively. 10.3% of the cardiac output was directed to the brain.

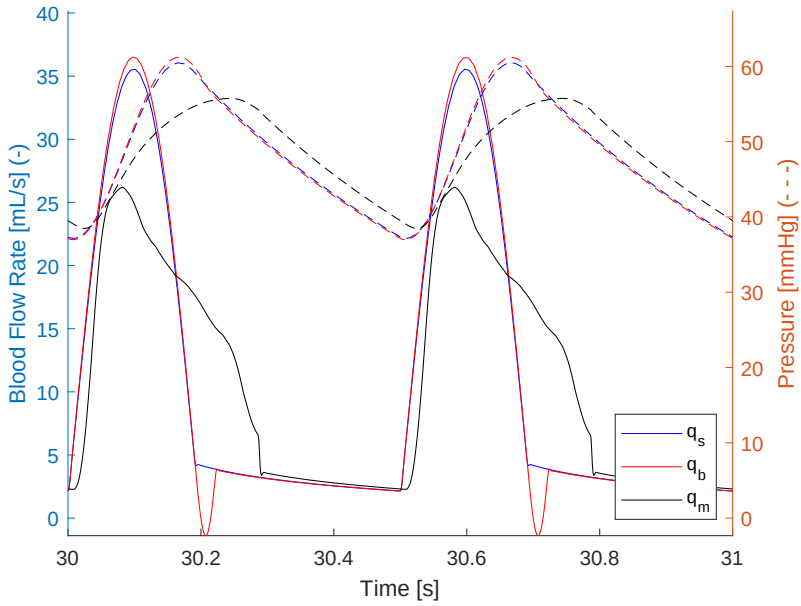

(a) Ascending Aorta.

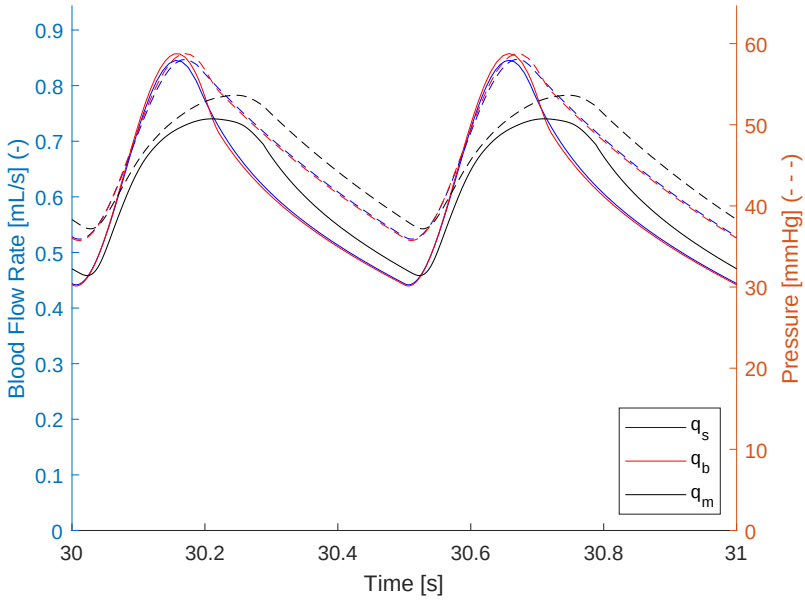

(b) Left brain.

Figure 3.4: Three different inflows were tested, a sine-shaped wave (q_s), a wave with backflow (q_b), and a wave based on US measurements (q_m). The simulated flow (—) and pressure curves (- - -) are shown for two heart beats halfway through the simulation.

Table 3.2: Targeted and achieved variable values for the steady-state model comparing three different inflows Targeted values are either from the literature or acquired experimentally. Abbreviations: R., right; L., left.

	Simulated			Target	
	q_s	q_b	q_m		Ref.
Heart Rate	120.00	120.00	120.00	120.00	Meas.
Stroke Volume $[\mathrm{mL\,s^{-1}}]$	5.89	5.89	5.89	5.89(93)	[53]
Cardiac Output $[\mathrm{mL\,min^{-1}}]$	707.28	707.28	707.29	769(256)	[50]
Systolic BP $[\mathrm{mmHg}]$	60.48	61.23	55.75	61	Meas.
Mean BP $[\mathrm{mmHg}]$	48.12	48.12	48.12	45	Calc.
Diastolic BP $[\mathrm{mmHg}]$	37.17	36.99	38.48	37	Meas.
Blood Flow Rate R./L. Brain $[\mathrm{mL\,s^{-1}}]$	0.61 / 0.61	0.61 / 0.61	0.61 / 0.61	0.64	[139]
Pulsatility Index (PI) R./L. Brain	0.66 / 0.66	0.68 / 0.68	0.46 / 0.46	0.78	Meas.

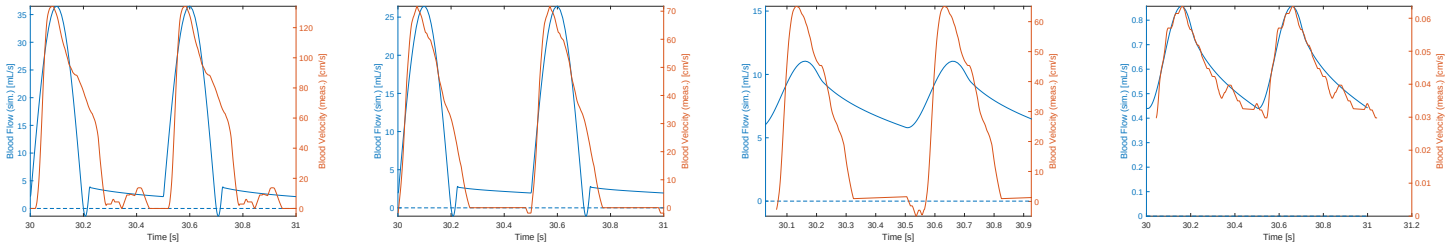

(a) Ascending Aorta.

(b) Aortic Isthmus (blue) and Abdominal Arch (orange).

(c) Descending Aorta (blue) and Abdominal Aorta (orange).

(d) Right brain.

Figure 3.5: Simulated flow (q_b, blue) are compared to measured flow velocity (orange) acquired at different locations in Sebastian, except for the right brain where a NeoDoppler recording of Joakim is used.

3.3 Model 2: Tilt test

Model 2 was described in section 2.3. Here, the results will be presented in three sections, beginning with simulated tilts with regulation. Thereafter, tilts were simulated with some regulatory mechanisms deactivated. Finally, simulations are shown where heart rate were used as input to the model. Many of the results are mainly conveyed through figures, and is discussed in the next chapter.

3.3.1 Tilt with Regulation

Both Joakim and Ida were used as templates for a tilt simulation, and the resulting flow rates can be seen in Figures 3.7a and 3.7c for Joakim and Ida, respectively. The mean effective flow cross-section is shown in Figure 3.6.

Figures 3.10 and 3.12 summarise mean values for BP, HR, flow rate and PI before (–), during (↑) and after (↓) the tilt, for Joakim and Ida, respectively. The full course of the variables can be found in Figures 3.9 and 3.11.

Total peripheral resistance can be calculated from Eq. (1.27), and is plotted in Figure 3.8c. The cerebral resistance is listed in Table 3.3, as is TPR, and plotted in Figure 3.8a. The mean deviations from $R_{p,0}$ were 140% (SD 500%) for Joakim and -13% (31%) for Ida. As $R \propto 1/a^4$ where a is vessel radius, the relative change in radius is $a/a_0 = \sqrt[4]{R_0/R}$. The estimated change in the radius of cerebral arterioles is plotted in Figure 3.8b and listed in Table 3.3. Mean relative radius change was -5% (17%) for Joakim and 6% (11%) for Ida.

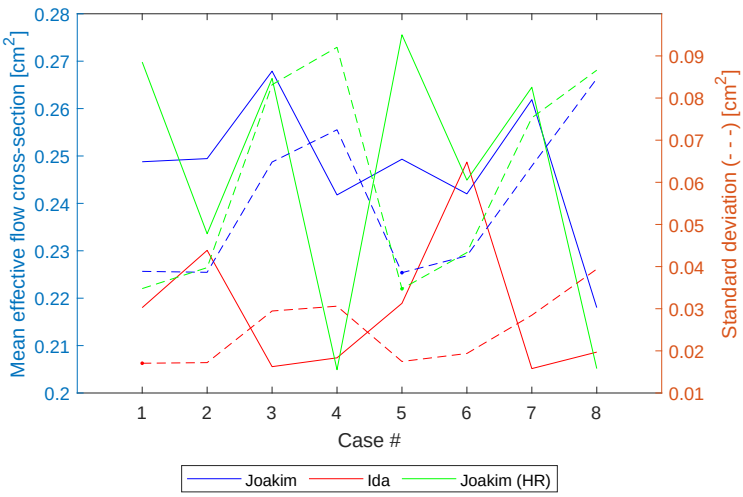

Figure 3.6: Effective flow cross-section (—) and standard deviation (- - -) for Joakim (blue), Ida (red) and Joakim with heart rate as input (green). The minimal standard deviation is indicated for each colour with a bullet (•). The eight cases are as defined in Table 2.2.

Table 3.3: Some values were not experimentally available, but could be extracted from the simulation before (–), during (↑) and after (↓) the tilt. Standard deviation is given in parenthesis.

	Joakim			Ida		
	–	↑	↓	–	↑	↓
TPR $[\mathrm{mmHg\,s\,mL^{-1}}]$	3.81 (0.10)	2.66 (0.28)	3.85 (0.07)	3.27 (0.03)	2.42 (0.07)	3.34 (0.22)
Change in cerebral arteriolar a	2% (12%)	0% (11%)	-19% (21%)	4% (6%)	6% (12%)	1% (6%)
Cerebral BP $[\mathrm{mmHg}]$	44 (1)	33 (3)	45 (0)	46 (0)	36 (1)	46 (1)

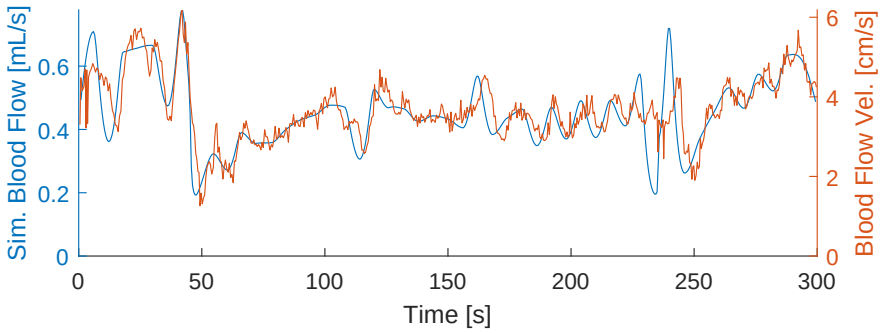

(a) Joakim.

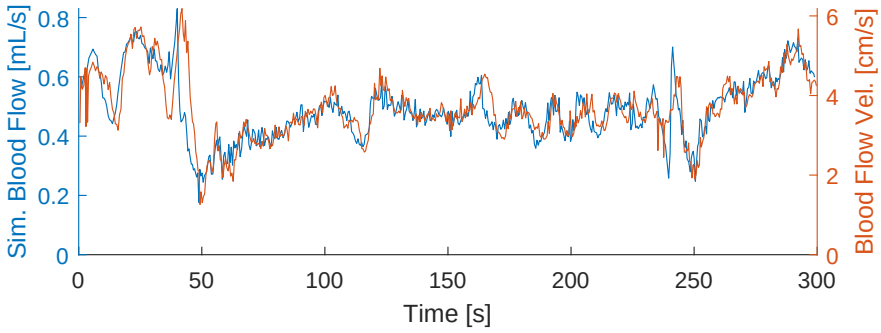

(b) Joakim with HR as input.

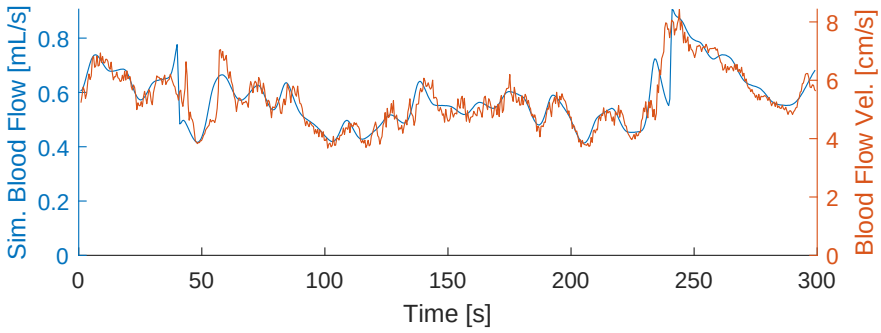

(c) Ida.

Figure 3.7: Simulated blood flow (blue) in the cerebral compartment and NeoDoppler recordings (orange).

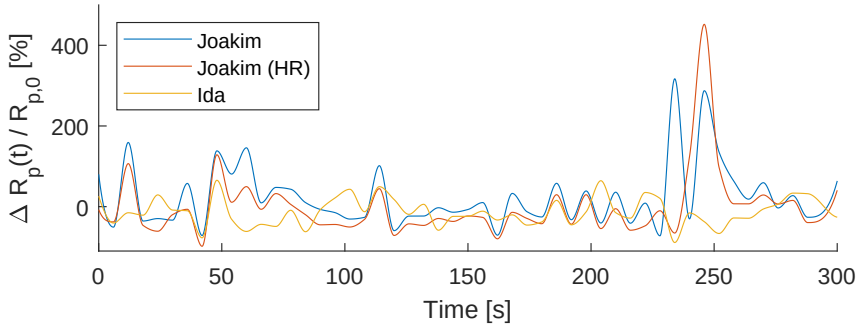

(a) Change in cerebral resistance R_p.

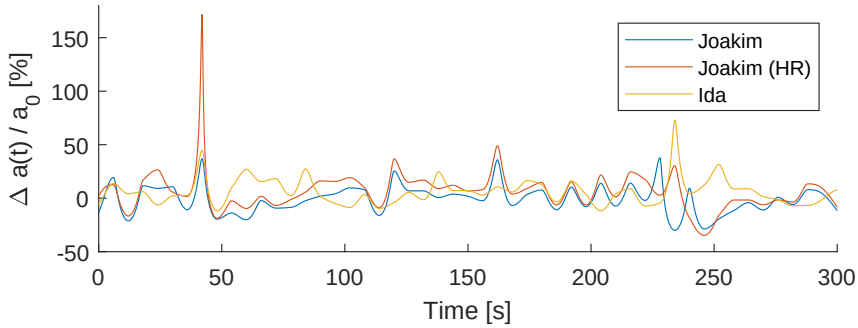

(b) Change in radius, a, of cerebral arterioles.

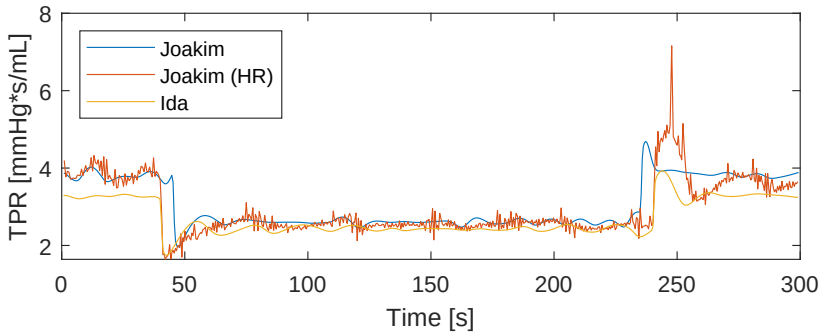

(c) Total Peripheral Resistance estimated from Eq. (1.27).

Figure 3.8: Simulated change in resistances during a tilt experiment.

3.3.2 Tilt with Partial Regulation

To explore the effect of each of the three regulatory mechanisms, simulations were carried out with one, two or all three deactivated. This yields seven cases in addition to the case presented in Section 3.3.1 with all regulatory mechanisms active. The configuration of the eight cases are described in Section 2.3.2 and presented in Table 2.2.

Figure 3.9 shows the time course of the eight simulations and the experimental Neo-Doppler recording for Joakim. The time has been shifted so that the tilt occurs at time $t = 0\,\mathrm{s}$, and a dotted line marks $t = 20\,\mathrm{s}$ to simplify categorisation into R1–R4 response patterns defined by Anthony, Evans and Levene [24] and described in Section 1.5.3. Mean values for blood pressures, flow rate, PI and heart rate before, during and after the tilt, are shown in Figure 3.10 for Joakim. Similarly is the time course of the simulation of Ida found in Figure 3.11, and a summary in Figure 3.12. Detailed plots of the time course of heart rate, PI, cerebral blood flow, and pressure in the aorta and in the brain for the eight cases can be found in Figures A.1 and A.2 for Joakim and Ida, respectively.

For both Joakim and Ida, the initial fall in flow velocity and rise in PI after the tilt were reproduced in all eight cases. The smallest change in PI was observed in case 2 where peripheral regulation was absent. The largest change in flow rate and PI were in case 8 where all regulatory mechanisms were lacking. Table 3.4 summarises how the different combination of regulatory mechanisms affect simulated blood pressure, heart rate and PI. Numerical values can be found in Table A.2. Similar response patterns are seen for case 1 and 3, and case 5 and 7. The difference between the cases in both couples is cerebral autoregulation. In other words, it seems that the presence of well functioning cerebral autoregulation cannot be inferred solely from a qualitative analysis of the change in heart rate, PI and blood pressure after a tilt. The change in PI can distinguish between concurrent absence of both cerebral and peripheral regulation and the absence of only peripheral regulation. PI increases more in the first case, independently of the presence of heart rate regulation.

The relative decrease in cerebral blood flow rate during tilt was about 25–30% in Joakim for all cases except 4, 6 and 8 (see Figure 3.10), and 20–25% in Ida for all cases except 4 and 8 (see Figure 3.12), as listed in Table A.2. The exceptions demonstrate larger drops in flow rate. Ida compensates quickly in terms of flow rate, and clearly shows a biphasic (R4) response as demonstrated in Figure 3.11. This biphasic response is reproduced in all cases except case 8, and to a lower degree in case 4. Joakim seems to exhibit a uniphasic response (R3), reproduced in all eight cases.

Simulating the cases including cerebral autoregulation took about 3–4 hours, whereas the other simulations were completed within 30 minutes.

Mean cerebral blood pressure (MCP) was initially 96% of MAP for Joakim in all cases. During tilt, MCP fell to about 55% of MAP for case 6 and 8, to about 60% of MAP for case 2 and 4, and to about 65% of MAP for the other cases. Pre-tilt levels were established shortly after the tilt was ended for all cases. For Ida, pre- and post-tilt levels were as for Joakim, but all cases yielded MCP at 67-71% of MAP.

The standard deviation of effective flow cross-section is a measure of how well the simulated results fit with the measured flow velocity, as flow rate is assumed to be proportional to flow velocity from Eq. 1.21 as long as the artery does not change its radius. The mean effective cross-section and standard deviation are shown in Figure 3.6.

Table 3.4: Qualitative responses to tilt in the eight cases. Arrows in parenthesis mark a small change. Flow rate decreased in all cases.

	Regulation			Response				
Case #	Cerebral	Peripheral	HR	HR	PI	SBP	MAP	DBP
1	+	+	+	↑	↑	↑	↑	↑
2	+	−	+	↑↑	(↑)	↓	(↓)	—
3	−	+	+	↑	↑	↑	↑	↑
4	−	−	+	↑↑	↑	↓	(↓)	—
5	+	+	−	—	↑	↑	↑	↑
6	+	−	−	—	↑	↓↓	↓↓	↓↓
7	−	+	−	—	↑	↑	↑	↑
8	−	−	−	—	↑↑	↓↓	↓↓	↓↓

3.3.3 Heart Rate as Input

As heart rate varied significantly during the test period, simulations were carried out using heart rate from the NeoDoppler recordings of Joakim as input. Eq. (2.2) was still used to generate a inflow signal, with systolic duration calculated from Eq. (1.3).

The simulated flow rate is shown in Figure 3.7b for case 1. All cases are displayed in Figure 3.13, with a summary in Figure 3.14. The time course of heart rate, PI, cerebral blood flow, and pressure in the aorta and in the brain for the eight cases can be found in Figure A.3.

The qualitative response patterns were as in Table 3.4 with a few exceptions in addition to change heart rate being equal for case 1–4 and case 5–8. PI increased, and MAP and diastolic blood pressure decreased, noticeably in case 2. A significant increase in PI was observed for case 4, and also a drop in MAP and diastolic blood pressure.

Prior to the tilt was MCP about 96% of MAP for all eight cases. MCP in case 1, 3, 5 and 7 was about 63% of MAP, whereas MCP in case 2, 4, 6 and 8 was about 52% of MAP. MCP returned to 96% of MAP after the tilt for all cases. TPR was estimated to be 3.87, 2.54, and 3.82 $\mathrm{mmHg\,s\,mL^{-1}}$ before, during and after the tilt, respectively. Mean effective flow cross-section is shown in Figure 3.6.

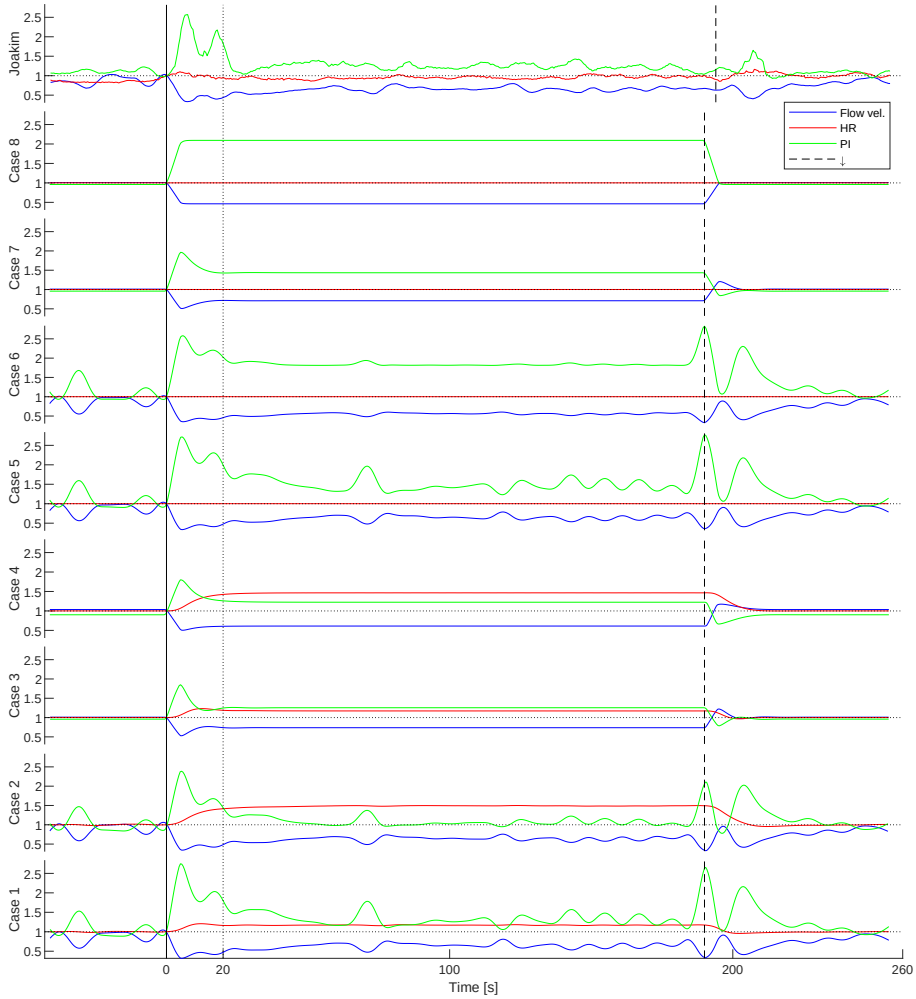

Case #	1	2	3	4	5	6	7	8
Cerebral regulation	+	+	–	–	+	+	–	–
Peripheral regulation	+	–	+	–	+	–	+	–
HR regulation	+	+	+	+	–	–	–	–

Figure 3.9: Time course of flow rate, heart rate (HR), and PI during a tilt simulation of Joakim. The data row contains a NeoDoppler recording, and shows flow velocity instead of flow rate. The table shows which regulatory mechanisms that were active (+) or inactive (–) in each case.

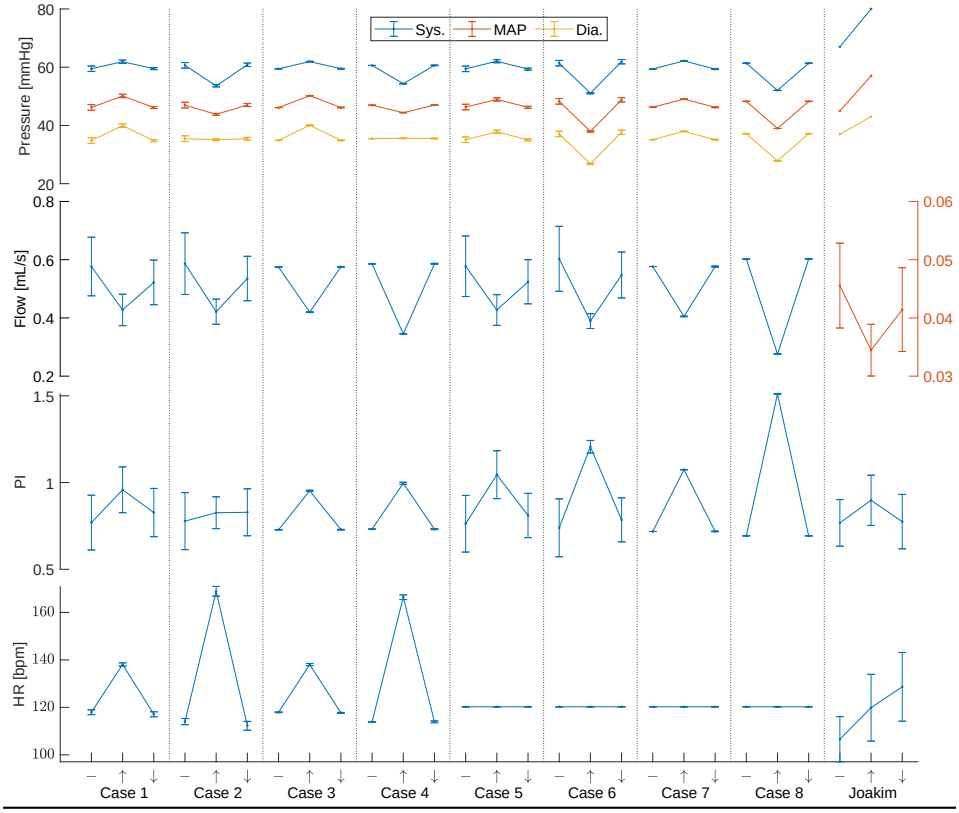

Case #	1	2	3	4	5	6	7	8
Cerebral regulation	+	+	–	–	+	+	–	–
Peripheral regulation	+	–	+	–	+	–	+	–
HR regulation	+	+	+	+	–	–	–	–

Figure 3.10: Summary of blood pressure, heart rate (HR), flow rate and PI before (–), during (↑) and after (↓) the tilt for a simulation of Joakim. Error bars represent standard deviation. The table shows which regulatory mechanisms that were active (+) or inactive (–) in each case.

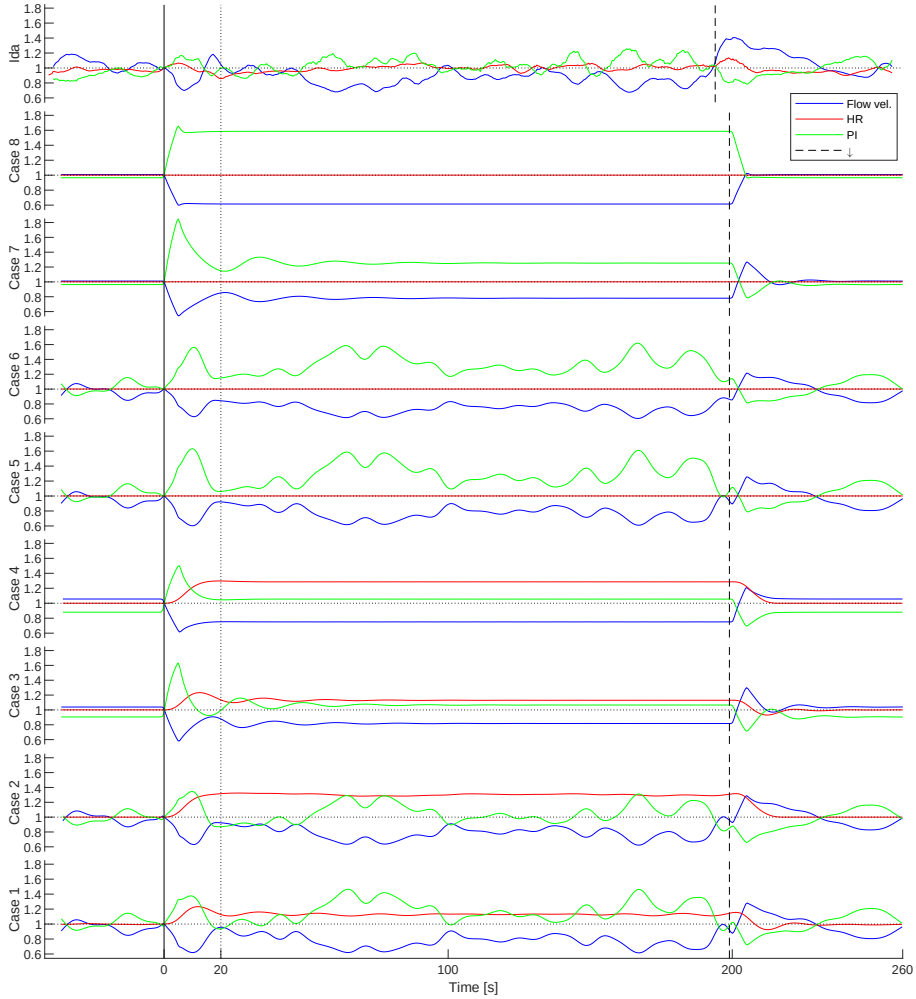

Case #	1	2	3	4	5	6	7	8
Cerebral regulation	+	+	–	–	+	+	–	–
Peripheral regulation	+	–	+	–	+	–	+	–
HR regulation	+	+	+	+	–	–	–	–

Figure 3.11: Time course of flow rate, heart rate (HR), and PI during a tilt simulation of Ida. The data row contains a NeoDoppler recording, and shows flow velocity instead of flow rate. The table shows which regulatory mechanisms that were active (+) or inactive (–) in each case.

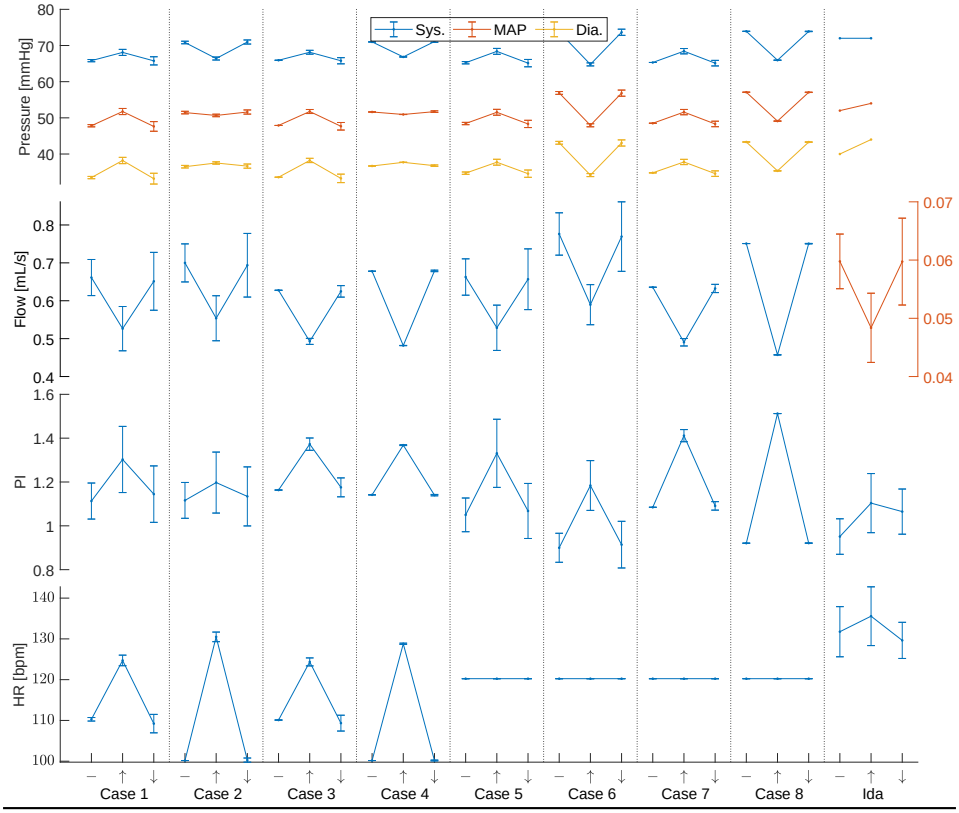

Case #	1	2	3	4	5	6	7	8
Cerebral regulation	+	+	–	–	+	+	–	–
Peripheral regulation	+	–	+	–	+	–	+	–
HR regulation	+	+	+	+	–	–	–	–

Figure 3.12: Summary of blood pressure, heart rate (HR), flow rate and PI before (–), during (↑) and after (↓) the tilt for a simulation of Ida. Error bars represent standard deviation. The data column is based on the NeoDoppler recording, and shows flow velocity [$\mathrm{m\,s^{-1}}$] rather than flow rate. The table shows which regulatory mechanisms that were active (+) or inactive (–) in each case.

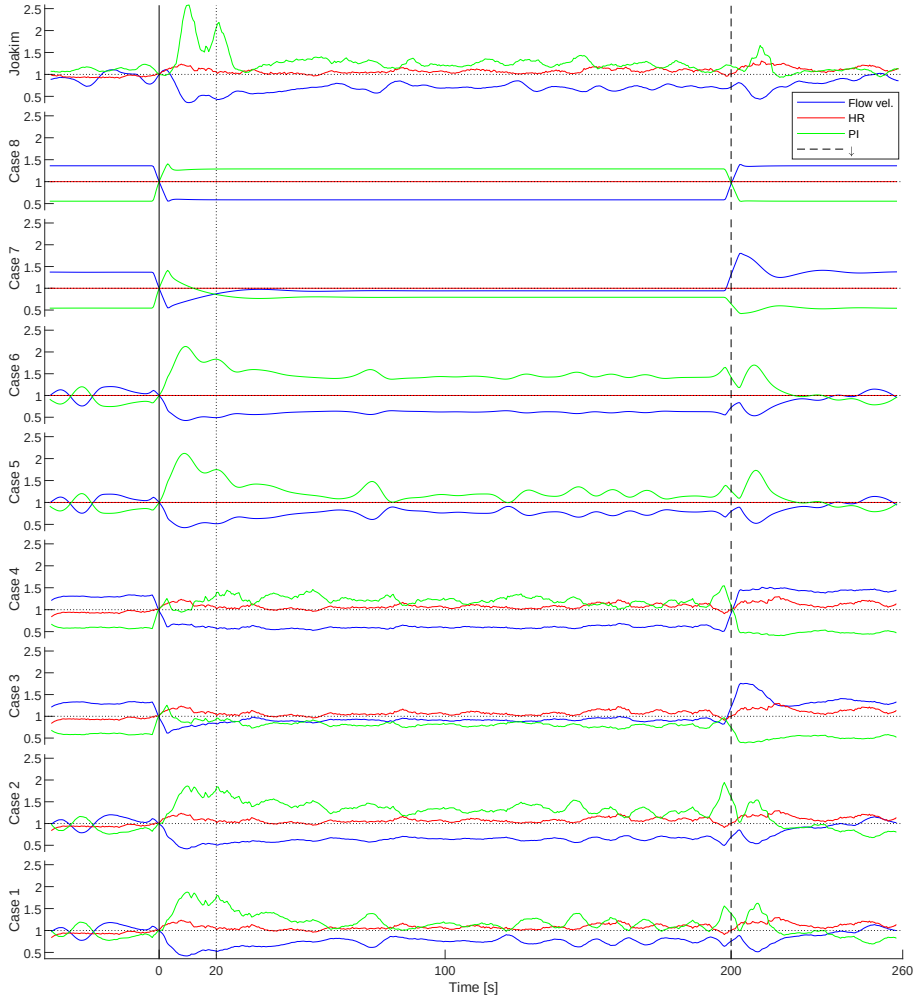

Case #	1	2	3	4	5	6	7	8
Cerebral regulation	+	+	–	–	+	+	–	–
Peripheral regulation	+	–	+	–	+	–	+	–
HR regulation	+	+	+	+	–	–	–	–

Figure 3.13: Time course of flow rate, heart rate (HR), and PI during a tilt simulation of Joakim using heart rate as input. The data row contains a NeoDoppler recording, and shows flow velocity instead of flow rate. The table shows which regulatory mechanisms that were active (+) or inactive (–) in each case.

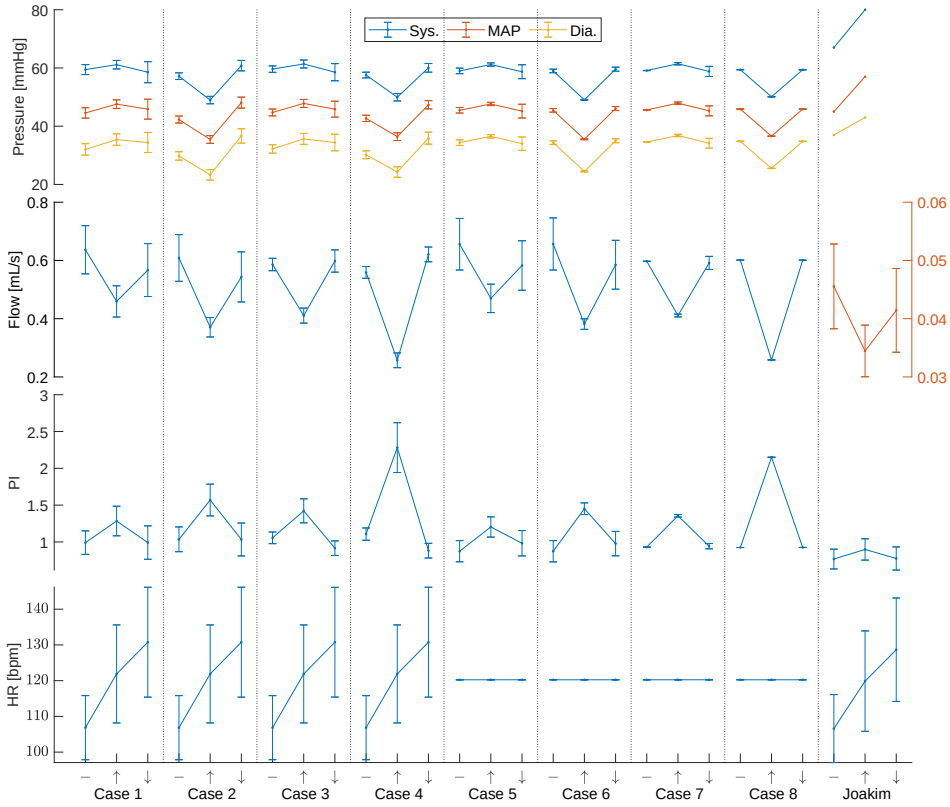

Case #	1	2	3	4	5	6	7	8
Cerebral regulation	+	+	–	–	+	+	–	–
Peripheral regulation	+	–	+	–	+	–	+	–
HR regulation	+	+	+	+	–	–	–	–

Figure 3.14: Summary of blood pressure, heart rate (HR), flow rate and PI before (–), during (↑) and after (↓) the tilt for a simulation of Joakim using heart rate as input. Error bars represent standard deviation. The data column is based on the NeoDoppler recording, and shows flow velocity [$\mathrm{m\,s^{-1}}$] rather than flow rate. The table shows which regulatory mechanisms that were active (+) or inactive (–) in each case.

Chapter 4

Discussion

> There is always a temptation to think too deeply about things.
>
> Phillips [140, p. 79]

The steady-state model with results in section 3.2 was able to reproduce targeted values for systolic and diastolic blood pressure, and distribution of blood flow to the brain as listed in Table 3.2. Matching heart rate, stroke volume and cardiac output were as expected, as these variables are determined by the input flow signal. Cardiac output can be calculated as the product of stroke volume and heart rate, which will give the simulated values. The average heart rate in neonates is often a bit higher than the pre-tilt level in Joakim, typically about 140 bpm when unstimulated [141], which may explain the gap between simulated and targeted cardiac output in Table 3.2.

The pulsatility index (PI) was lower in the steady-state simulation than in the recording. Whereas MAP strongly depends on pressure wave form, is PI dependent of flow wave form. Both wave forms are shown in Figure 3.4 for three different input signals.

Flow wave form in central compartments displayed varying agreement with Doppler recordings, but showed good correspondence with Doppler recordings in the cerebral compartment. Figures 3.5a and 3.5b show a minimal change in wave profile between the compartments for ascending aorta and aortic isthmus. Both display a non-zero flow in diastole and are similar to the simulation output of Garcia-Canadilla et al. [28] for the aortic isthmus as shown in Figure 1.29. Figure 3.5c demonstrates a misfit between simulated and measured wave profile in the descending aorta. From Figure 1.18, the physiological flow wave in the descending aorta of a healthy child seems to be similar to simulated output in the aortic isthmus. The simulated output for the descending aorta is more similar to peripheral flow. This suggests that the compliance in the compartment representing the descending aorta is too high. However, increasing it further more lowers the diastolic flow in the ascending aorta towards zero, and decreasing it increases the diastolic flow in the ascending aorta, demonstrating that the compartments are interacting and great care has to be taken to optimise all compartments simultaneously.

As recordings in general were only collected from the cerebral arteries, the peripheral compartments were not prioritised in this project. In future works, ductus arteriosus should be implemented alongside pulmonary circulation. Model parameters will then have to be re-estimated, and experimental Doppler measurements from the anatomic locations may be gathered to guide the adaption. More attention may be offered non-cerebral compartments as one have experimental data for these locations from the same individual. Also, the non-cerebral Doppler measurements were acquired from Sebastian who was born preterm and had an open ductus arteriosus, whereas the simulation was adapted to an infant born at term an assumed closed ductus arteriosus. Some of the discrepancy may thus be explained by the model trying to describe another condition than the experimental measurements.

MAP changed up to 34% in response to tilt (see Figure 3.2). This is greater than predicted by Figure 1.11. As various tilt responses are seen, with both increase and decrease in blood pressure, the average response of a group tends to be small, and there is likely to exist sub-groups. Analysis of the experimental data falls outside the scope of this thesis and will likely be addressed in an upcoming paper by Siv S. Ødegård.

Experimentally, blood pressures were acquired using an oscillometric technique [142]. Although this is a commonly used method for neonates in the clinical setting, due to its simplicity and low risk, several studies find deviations between oscillometric and invasively measured blood pressure. Lalan and Blowey [143] found MAP to be overestimated by $4.8(98)\,\mathrm{mmHg}$ using oscillometry versus intra-arterial measurement, in line with earlier studies [144]. Equipment from different producers also seem to produce biased measurements, especially for large and small infants [145]. Different manufacturers apply different algorithms to calculate systolic, mean and diastolic blood pressure [146]. Others have found good agreement between oscillometry and intra-arterial measurements in normotensive infants [147, 148], or a similar overestimation in the presence of hypotension [149], or even underestimation of MAP [150, 151]. However, healthy infants are rarely subjected to invasive blood pressure measurements and less is known about its accuracy.

Additionally, blood pressure measurements are complicated by intrinsic and extrinsic motion artefacts [152]. Intrinsic motion artefacts are caused by the motions of the infant, who often cry and struggle as the inflated cuff can be uncomfortable. Extrinsic motion artefacts can arise from the clinician moving the bed or unintentionally compressing the cuff. Stress and arousal tend to falsely rise the blood pressure, concealing some of the true effect of tilt on the hemodynamics. In adults, talking has been found to increase the systolic blood pressure by $17\,\mathrm{mmHg}$ and exposure to cold leads to an increase of $11\,\mathrm{mmHg}$ [153]. Thus, there is some uncertainty associated with the change in blood pressure observed after the tilt, as in Figure 3.2.

Simulation results depend on the shape of the flow waves in the input signal as shown in Figure 3.4. Table 3.2 reveals that the systolic blood pressure was about 10% lower and the PI about 30% lower for simulations using the measured inflow signal (q_m) compared to simulations using the two sine based signals (q_s and q_b). The latter is similar to the relative difference in peak systolic velocity and also PI between the measured and the sine shaped input signals themselves. The sine shaped signal was mainly chosen because Doppler recording of the aortic valve outflow was only available for Sebastian who was

prematurely born and had a large, open ductus, whereas Joakim and Ida were assumed to have closed ductus and were born at term. The input signal used by Garcia-Canadilla et al. [28], shown in Figure 1.29, seems more similar to q_s than q_m, so does the Doppler spectrum from the left ventricular outflow tract shown in Figure 1.18a, although both have a steeper rise in the beginning of systole than q_s. A backflow was added to model the physiological backflow that closes the aortic valve at the end of systole, and several earlier studies have also included this backflow [see eg. 48, 154, 155]. The backflow contributes to a larger pulsatility of q_b compared to q_s as the stroke volume is equal for both. This may explain why q_b has the largest PI and pulse pressure of the three inflow signals.

The steepness of the inflow wave used as input is determined by stroke volume in Eq. (1.2) and systolic duration in Eq. (1.3). Both have been estimated by data from the literature for infants of adequate age. Figure 2.10 shows that despite increasing steepness, the peak value of the inflow wave in Joakim is almost constant at about $50\,\mathrm{mL\,s^{-1}}$, and about $60\,\mathrm{mL\,s^{-1}}$ in Ida. This is expected as peak flow rate from Eq. (2.4) is about $14.75 \cdot$ bw [kg] for high heart rates (HR) when the fractional backflow duration a is $1/6$. bw is birth weight. The aortic valve annulus diameter in neonates with closed ductus arteriosus have been found to be approximately $d[\mathrm{mm}] = 4.3 + 0.9 \cdot$ bw [kg] [156]. In Joakim, this yield a cross-section of $0.42\,\mathrm{cm^2}$ and a peak blood velocity of $240\,\mathrm{cm\,s^{-1}}$, which is significantly higher than the expected peak blood velocity [104, 105]. It is similarly high for Ida, at $237\,\mathrm{cm\,s^{-1}}$. The aortic root in neonates is found to have a diameter $d[\mathrm{mm}] = 5.64 + 1.18 \cdot$ bw [kg] [157]. If the inflow is assumed to be applied at the level of the aortic root, peak velocities are $139\,\mathrm{cm\,s^{-1}}$ in Joakim and $138\,\mathrm{cm\,s^{-1}}$ in Ida. Although both estimates are higher than the reported normal values, small changes in radius will have a great impact on estimated peak velocity due to the quadratic dependence on vessel radius. The actual flow velocity profile inside the vessel are not known, Also, direct comparison may be difficult as the average dimensions are from different study populations than the ones used to design the inflow waves.

Another explanation for the high peak systolic velocity may be that the relative systolic duration is too short. Figure 1.6 shows the relationship between heart rate and relative systolic duration used in this project, and the values are in line with other studies reporting t_s/t_c about 40% at heart 130 bpm [158, 159]. It is possible that the regression line shown in Figure 1.6 is too steep and that the systolic duration is underestimated at heart rates below 130 bpm, but the heart rate is seldom below 120 bpm in the simulation so it seems unlikely that this would have a large effect. An open ductus arteriosus may also affect systolic duration, and a longer left ventricular ejection time has been reported before closure [160]. An open ductus arteriosus is known to be the case for Sebastian, but not for Joakim and Ida, but may account for some of the difference in systolic length between the measurements of Sebastian and the values reported in the literature.

Finally, the high peak systolic velocity may be caused by the stroke volume being too high. However, the value of $5.89\,\mathrm{mL}$ used in the simulation is within the normal ranges reported for term neonates [53, 161, 162], although a lower value, about $4\,\mathrm{mL}$ at the weight of Joakim, has been reported when using three-dimensional echocardiography rather than Doppler and M mode ultrasound [163]. As stroke volume was not measured for Ida and Joakim, it is difficult to make better estimates than reported normal values adjusted for age and weight. In addition, a small difference is observed between the

sexes ($1.236(79)\,\mathrm{mL\,kg^{-1}}$ for boys and $1.199(84)\,\mathrm{mL\,kg^{-1}}$ for girls) and between infants with open and closed ductus ($1.242(79)\,\mathrm{mL\,kg^{-1}}$ for open and $1.217(83)\,\mathrm{mL\,kg^{-1}}$ for closed) [163]. These differences were not considered due to their size.

Effective flow cross-section was estimated as if all cerebral blood was collected in two single arteries, one for each hemisphere. In practise, only 8% of the cerebral blood flow is directed to the anterior cerebral artery in adults with a complete circle of Willis [164]. Correcting the effective flow cross-section this factor, estimated radius of the anterior cerebral artery becomes $0.8\,\mathrm{mm}$ The radius of the middle cerebral artery in fetuses at 37–40 weeks of gestation is reported to be in the range 0.43–$0.80\,\mathrm{mm}$ (mean $0.61\,\mathrm{mm}$, SD $0.11\,\mathrm{mm}$) [165]. The identity of the vessel insonated by the NeoDoppler probe is not known, but its dimension is consistent with the major cerebral arteries such as the anterior cerebral artery.

Cerebral circulation was described using only two compartments in the model, whereas the anatomy of the brain is complex, as illustrated in Section 1.5.1. The configuration of the circle of Willis varies in the population, and the circulatory consequences of these variations, and also pathology, have been subject to investigation by computer modelling [see eg. 166–168]. Implementing the circle of Willis would offer the possibility to observe if and how flow patterns and wave profiles differ between the major cerebral arteries and in different configurations. Figure 1.17, in addition to other studies, demonstrates that differences exist between the anterior and middle cerebral arteries in neonates [107, 169]. Yet an accurate implementation requires data regarding the vessels, adding new sources of error as the number of parameters needed to be estimated in the model increases. Adding more components may also increase the time needed to run a simulation.

The lack of ductus arteriosus is an important limitation of the model. As mentioned in Section 1.5.1, the ductus normally closes about 27 hours after birth in boys and 45 hours after birth in girls [42], suggesting that Joakim has a closed ductus at the time of the tilt experiment, whereas Ida still has an open ductus. A open ductus arteriosus has been found to increase cerebral PI and cerebral peak systolic flow velocity, but the effect depends on the size of the ductus [170–172]. These characteristics are compatible with Ida having an open ductus and Joakim a closed ductus, or that both have an open ductus, but the one of Ida has a larger diameter. The difference in pulsatility is demonstrated in Figure 3.3. Hence is the accuracy of the model likely to increase if the pulmonary circulation is added alongside a compartment representing the ductus arteriosus. On the other hand was simulated relative change in PI closer to the experimental values for Ida than for Joakim (see Table A.2), even though the values of the PI agreed better for Joakim as shown in Figures 3.10 and 3.12.

A more complex representation of the heart may also be a way of improving the model. The current implementation provided inflow to the aorta solely as a function of heart rate, although heart rate was regulated by the blood pressure in the carotid artery. Pooling effects and reduced venous return caused by the tilt were thus ignored. This may be a reasonable simplification as earlier studies suggest that the stroke volume in neonates is not significantly altered by a tilt, as shown in Figure 1.10 [73, 90]. Several studies have employed models of the heart that depend on venous return and venous and atrial pressures [see eg. 70, 132, 173], and although most have focused on adults, some models have also been developed for foetuses and neonates [see eg. 125, 126, 128]. An advantage of

the current implementation of the heart is that each cardiac cycle is independent from the previous ones, which ensures a reliable input signal, and reduces the risk of errors accumulating during the course of the simulation. This is important as the simulation results depend strongly on the inflow signal, as demonstrated in Figure 3.4 and Table 3.2.

Inertia was scaled down to a negligible value to avoid oscillations. The benefits of including inertia in the model is disputed, as mentioned in Section 1.7.3. Master student Nguyen [27] chose another approach. Since resistance, compliance and inertia are proportional to vessel length as seen in Eqs. (1.22), (1.28) and (1.32), the variables will decrease if the vessel compartments are split into shorter segments. When inertia and compliance are decreased in the compartments, the resonant frequency increases rapidly according to Eq. (1.34) until it is no longer sampled. The approach was found to yield more accurate wave forms. However, serious constraints were put on simulation time that was limited to under $15\,\mathrm{s}$, and the system became less stable. Other options may include to low-pass filter the simulated results before further processing, reduce the number of inductors in the circuit and increase their inductance accordingly, or include the inductors in parallel instead of series. The choice of reducing inductance was also made for the original model by Garcia-Canadilla et al. [28] (Patricia Garcia-Cañadilla, personal communication, April 4, 2019). This may have led to less accurate parameter values and wave profiles.

The model contains a large number of parameters to optimise. Although six compartments were removed from the original model by Garcia-Canadilla et al. [28], 15 compartments with three components each and a resistor representing the coronary arteries, remained. The inductors were in practise ignored when the inductance was scaled down as discussed above. Hence, 36 component values had to be adapted, in addition to parameters relating to the regulatory mechanisms. It was prioritised to optimise for the variables where experimental values from Joakim and Ida were available. Thus the brain compartments were offered most attention, and parameters were modified to provide good fit with experimental data. The compartment representing the ascending aorta was modified to yield fitting systolic and diastolic blood pressure, and MAP. Component values in the central compartments were originally estimated from measurements of foetuses Garcia-Canadilla et al. [28]. However, small changes in vessel radius yield large changes in both R and C from Eqs. (1.22) and (1.32), and therefore may relatively large deviations from the original values for central compartments reflect modest variation in vessel size.

Pressure measurements are in general not experimentally available for the brain, and only a handful values have been reported in the literature, suggesting that the blood pressure in the middle cerebral artery is about 75% of MAP [174]. No experimental values have been found for infants, in spite of a thorough search in the literature and consulting several local and foreign clinicians and researchers. In the model, mean cerebral blood pressure was found to be about 95% of MAP in steady-state, dropping to below 70% during the tilt for all eight cases. The non-linear relationship between pressure, resistance and flow becomes important as the cerebral blood pressure decreases as illustrated in Figure 1.23. Tran [29] and Wisløff [30] found that resistance dependent on local pressure yielded more accurate results than pressure independent resistances using Simscape models. However, the inclusion of critical closure pressure may be more relevant in studies of ill or pre-term neonates where low blood pressures and insufficient cerebral blood flow are more commonly seen.

Intracranial, intrathoracic and venous pressures were not implemented in the model. Intracranial pressure affects, and is affected by, the cerebral blood flow and is of great interest in the clinic [175], and it has been found to vary with head position and is likely altered by a tilt [176]. As the intracranial pressure alters transmural pressure, it may change the compliance of the cerebral arteries. The intrathoracic pressure changes as part of breathing, and is likely to have greatest effect on the pulmonary circulation and also venous return. Pulmonary circulation and veins in general were not considered in this project. It is possible that some of the oscillations seen in the recordings in Figure 3.3 reflect respiration. Cerebral venous outflow seems to be redistributed at changes in posture [177]. Implementing these effects may improve the model, but also adds uncertainty and requires additional experimental data.

Total peripheral resistance (TPR), as shown in Figure 3.8c and Table 3.3, was similar to reported values for the neonate [128, 130]. This is expected as TPR was calculated from Eq. (1.27), and both cardiac output and MAP were within normal ranges. Figure 1.27 demonstrates how TPR increases slightly as the ductus arteriosus closes, but the effect is small.

TPR falls during the tilt as indicated in Table 3.3, and MAP is stabilised by an increase in heart rate. The effect of changing peripheral resistance can be illustrated by keeping the TPR constant during a tilt experiment. This is done in the simulated cases 2, 4, 6 and 8, and the consequences are illustrated in Table 3.4. The absence of peripheral regulation makes the systolic blood pressure decrease during the tilt. An increase in heart rate seems to partly or completely compensate the lack of peripheral regulation, keeping MAP and diastolic blood pressure almost unchanged. However, if both TPR and heart rate are kept constant, a significant decrease in MAP, and systolic and diastolic blood pressure is seen. A drop in TPR in response to tilt has been suggested to be part of a healthy response in young adults [178], whereas an increase has been reported in children with vasovagal syncope [89].

The average changes in cerebral arterioles in response to tilt were small, with a peak at the time of the tilt. This peak may be partly explained by the timing of the simulated tilt compared to the experimental tilt. The timings used in the simulations were slightly different for Joakim with and without heart rate as input, as the tilt seems to have happened a bit earlier than $40\,\mathrm{s}$ from the velocity recording and this was accounted for when not using heart rate as input. The peak may also indicate a rapid response to the fall in cerebral blood flow before the peripheral regulation starts to increase the systemic blood pressure.

Figure 1.11 shows that a variety of responses have been reported in the literature, as elaborated in Section 1.5.3. None of the simulated cases yielded decrease in heart rate during tilt. Eq. (1.27) describes the relation between MAP, TPR and heart rate. If MAP is raised by heart rate, the peripheral resistance will stay low, and vice versa. The time constants used to determine how quickly each regulatory mechanism thus also affect how the other mechanisms respond. Further studies are needed to establish how k and τ influences the behaviour of the system.

Evaluating which case that fits the experimental data best can be done in several ways. The standard deviation of effective flow cross-section shown in Figure 3.6 is one measure. The artery observed by the NeoDoppler device can be assumed to have a constant radius throughout the experiment as the peripheral resistance is mainly regulated in the arteri-

oles, not the arteries, and flow rate and flow velocity will then be proportional under the assumptions described in Section 1.7.1. The lowest standard deviation is found for Ida in case 1. This is reasonable from Figure 3.7 where the simulation with Joakim have a mismatch early in the simulation, and also at the back-tilt. The simulation with Joakim and heart rate as input agrees more, but the decrease in flow rate happens before the decrease in flow velocity, leaving a mismatch around the time of the tilt. For the two simulations of Joakim is the lowest standard deviation found for case 5. Case 5 describes a situation with cerebral and peripheral regulation, but constant heart rate. The increase in heart rate observed in the data is thus not accounted for, and the simulated increase in PI is higher than observed experimentally. Case 1 seems to fit better as the difference in standard deviation between case 1 and case 5 is negligible, and case 1 provides a better description of the increase in heart rate, PI, MAP and diastolic pressure than case 5. For Ida increases PI with 17% in case 1 and 27% in case 5, compared to 16% in the recording.

A general challenge in this project is the mixing of values acquired from individuals and from populations. Although normal ranges are often reported, one single value has to be chosen to be used in the model. In this project have gestational age and birth weight been used to acquire as accurate values as possible from the literature. Joakim and Ida were clinically assessed before participating in the tilt experiment, and were found to be healthy. It is thus likely that they are representative for the normal populations found in the literature.

Further Work

The discussion above has highlighted several limitations and shortcomings of the current model. The model can be improved by adding compartments for the ductus arteriosus, pulmonary circulation, the circle of Willis, and the heart, including venous return. Another avenue of improvement is optimised parameter estimation, both for component values and parameters for the regulatory mechanisms (k and τ). Algorithms exist that can be used to optimise the set of parameters for given outcomes. More complex representations of the regulatory mechanisms can also be employed, as they are constituted of several subsystems reacting to chemical and neural signals.

More experimental data is also important to improve the model. Doppler measurements can be acquired from several locations in the same individuals performing the tilt test. This way, each compartment can be adjusted to achieve wave profiles similar to the Doppler recording. A continuous pressure recording in parallel with a NeoDoppler recording would provide a valuable way of validating the pressure wave profile and how it changes during a tilt. Standardised experiments will be important as different tilt responses have been observed in different conditions, such as active versus quiet sleep.

Chapter 5

Conclusion

> Knowing when to stop, whatever else it is, is always guess-work.
>
> Phillips [140, p. 41]

In this project, a simple lumped multi-compartment model is developed to investigate cerebral blood flow during steady- and altered state. The model was based on a published model for foetal circluation and implented in Simscape and MATLAB. The altered state was induced by tilting the neonate $90°$ from supine to upright position, introducing a hydrostatic pressure between heart and brain. Simulated results were compared to NeoDoppler recordings from experimental tilt tests. Three regulatory mechanisms were implemented in the model so that their relative contribution to cerebral blood flow could be assessed.

It was identified a range of studies on neonates and the tilt test. A variety of responses had been described with both increases and decreases in blood pressure and heart rate, and also individuals that did not show any specific response. Individual neonates also displayed different responses from day to day the first month after birth.

The simulations were able to reproduce several features of the experimental data, such as a decrease in flow, an increase in blood pressure, an increase in heart rate and an increase in PI. Specific responses were observed as different combinations of regulatory mechanisms were active. The simulation with all regulatory mechanisms activated showed the best agreement with the NeoDoppler recordings.

The model seems to be a promising point of departure for further studies, but several improvements are suggested, and further development of the model is best guided by more experimental data.

Bibliography

[1] *Applied Physics and Mathematics - Masters Degree Programm (MSc. 5 Years) - NTNU*. URL: https://www.ntnu.edu/studies/mtfyma (visited on 22/06/2019).

[2] *Infant | Origin and Meaning of Infant by Online Etymology Dictionary*. en. URL: https://www.etymonline.com/word/infant (visited on 21/06/2019).

[3] D. W. Winnicott. 'The Theory of the Parent-Infant Relationship'. eng. In: *The International Journal of Psycho-Analysis* 41 (1960 Nov-Dec), pp. 585–595. ISSN: 0020-7578.

[4] Alok Sharma, Simon Ford and Jennifer Calvert. 'Adaptation for Life: A Review of Neonatal Physiology'. en. In: *Anaesthesia & Intensive Care Medicine* 12.3 (Mar. 2011), pp. 85–90. ISSN: 14720299. DOI: 10.1016/j.mpaic.2010.11.003. URL: https://linkinghub.elsevier.com/retrieve/pii/S147202991000295X (visited on 30/12/2018).

[5] Marta Ebbing. 'Fødsler i Norge 1967-2016 – Noen Nøkkeltall'. In: *Norsk Epidemiologi* 27.1-2 (Oct. 2017). ISSN: 0803-2491. DOI: 10.5324/nje.v27i1-2.2396. URL: http://www.ntnu.no/ojs/index.php/norepid/article/view/2396 (visited on 14/06/2019).

[6] Jelka Zupan and Elisabeth Åhman. *Neonatal and Perinatal Mortality: Country, Regional and Global Estimates*. Geneva: World Health Organization, 2006. ISBN: 978-92-4-156320-8.

[7] Liisa Lehtonen et al. 'Early Neonatal Death: A Challenge Worldwide'. In: *Seminars in Fetal and Neonatal Medicine*. STILLBIRTH AND EARLY NEONATAL DEATH 22.3 (June 2017), pp. 153–160. ISSN: 1744-165X. DOI: 10.1016/j.siny.2017.02.006. URL: http://www.sciencedirect.com/science/article/pii/S1744165X17300215 (visited on 14/06/2019).

[8] Jan L. Wallander et al. 'Developmental Trajectories of Children with Birth Asphyxia through 36 Months of Age in Low/Low-Middle Income Countries'. In: *Early human development* 90.7 (July 2014), pp. 343–348. ISSN: 0378-3782. DOI: 10.1016/j.earlhumdev.2014.04.013. URL: https://www.ncbi.nlm.nih.gov/pmc/articles/PMC4097313/ (visited on 24/06/2019).

[9] Ashna D. Mohangoo et al. 'Gestational Age Patterns of Fetal and Neonatal Mortality in Europe: Results from the Euro-Peristat Project'. In: *PLoS ONE* 6.11 (Nov. 2011). ISSN: 1932-6203. DOI: 10.1371/journal.pone.0024727. URL: https://www.ncbi.nlm.nih.gov/pmc/articles/PMC3217927/ (visited on 14/06/2019).

[10] Joy E. Lawn, Simon Cousens and Jelka Zupan. '4 Million Neonatal Deaths: When? Where? Why?' English. In: *The Lancet* 365.9462 (Mar. 2005), pp. 891–900. ISSN: 0140-6736, 1474-547X. DOI: 10.1016/S0140-6736(05)71048-5. URL: https://www.thelancet.com/journals/lancet/article/PIIS0140-6736(05)71048-5/abstract (visited on 15/06/2019).

[11] Sriparna Basu et al. 'Cerebral Blood Flow Velocity in Early-Onset Neonatal Sepsis and Its Clinical Significance'. en. In: *European Journal of Pediatrics* 171.6 (June 2012), pp. 901–909. ISSN: 1432-1076. DOI: 10.1007/s00431-011-1643-y. URL: https://doi.org/10.1007/s00431-011-1643-y (visited on 21/01/2019).

[12] Tai-Wei Wu, Timur Azhibekov and Istvan Seri. 'Transitional Hemodynamics in Preterm Neonates: Clinical Relevance'. In: *Pediatrics & Neonatology* 57.1 (Feb. 2016), pp. 7–18. ISSN: 1875-9572. DOI: 10.1016/j.pedneo.2015.07.002. URL: http://www.sciencedirect.com/science/article/pii/S1875957215001151 (visited on 21/01/2019).

[13] Lancelot J. Millar et al. 'Neonatal Hypoxia Ischaemia: Mechanisms, Models, and Therapeutic Challenges'. In: *Frontiers in Cellular Neuroscience* 11 (May 2017). ISSN: 1662-5102. DOI: 10.3389/fncel.2017.00078. URL: https://www.ncbi.nlm.nih.gov/pmc/articles/PMC5420571/ (visited on 04/06/2019).

[14] Donna M. Ferriero. 'Neonatal Brain Injury'. In: *New England Journal of Medicine* 351.19 (Nov. 2004), pp. 1985–1995. ISSN: 0028-4793. DOI: 10.1056/NEJMra041996. URL: https://doi.org/10.1056/NEJMra041996 (visited on 04/06/2019).

[15] Sigrid Dannheim Vik et al. 'NeoDoppler – New Ultrasound Technology for Continuous Cerebral Circulation Monitoring in Neonates'. In: *Pediatric Research (In review)* ().

[16] NTNU. *NeoDoppler - Department of Circulation and Medical Imaging*. en. URL: https://www.ntnu.edu/isb/neodoppler%5C#/view/about (visited on 19/04/2019).

[17] Gorm Greisen. 'Autoregulation of Cerebral Blood Flow in Newborn Babies'. In: *Early Human Development* 81.5 (May 2005), pp. 423–428. ISSN: 0378-3782. DOI: 10.1016/j.earlhumdev.2005.03.005. URL: http://www.sciencedirect.com/science/article/pii/S0378378205000630 (visited on 16/01/2019).

[18] Christopher J. Rhee et al. 'Neonatal Cerebrovascular Autoregulation'. En. In: *Pediatric Research* 84.5 (Nov. 2018), p. 602. ISSN: 1530-0447. DOI: 10.1038/s41390-018-0141-6. URL: https://www.nature.com/articles/s41390-018-0141-6 (visited on 16/01/2019).

[19] A. Hänninen, T. Peltonen and L. Hirvonen. 'RESPONSE OF BLOOD PRESSURE TO SUCKING AND TILTING IN THE NEWBORN PREMATURE INFANT'. eng. In: *Annales Paediatriae Fenniae* 10 (1964), pp. 92–98. ISSN: 0570-1732.

[20] Marianne Thoresen, Frances Cowan and Lars Walløe. 'Cardiovascular Responses to Tilting in Healthy Newborn Babies'. In: *Early Human Development* 26.3 (Oct. 1991), pp. 213–222. ISSN: 0378-3782. DOI: 10.1016/0378-3782(91)90161-U. URL: http://www.sciencedirect.com/science/article/pii/037837829190161U (visited on 16/04/2019).

[21] Danusa Andrásyová and Eva Kellerová. 'Blood Pressure and Heart Rate Response to Head-up Position in Full-Term Newborns'. In: *Early Human Development* 44.3 (Mar. 1996), pp. 169–178. ISSN: 0378-3782. DOI: 10.1016/0378-3782(95)01706-2. URL: http://www.sciencedirect.com/science/article/pii/0378378295017062 (visited on 16/04/2019).

[22] C.-M. Chen, T.-C. Tsai and M.-C. Lan. 'Effect of Body Tilting on Physiological Functions in Healthy Term Neonates'. en. In: *Acta Paediatrica* 84.5 (1995), pp. 474–477. ISSN: 1651-2227. DOI: 10.1111/j.1651-2227.1995.tb13677.x. URL: https://onlinelibrary.wiley.com/doi/abs/10.1111/j.1651-2227.1995.tb13677.x (visited on 16/04/2019).

[23] Martial M. Massin et al. 'Heart Rate Response Profiles to Tilting in Healthy and Unhealthy Neonates'. eng. In: *Medical Science Monitor: International Medical Journal of Experimental and Clinical Research* 8.5 (May 2002), CR321–325. ISSN: 1234-1010.

[24] M. Y. Anthony, D. H. Evans and M. I. Levene. 'Neonatal Cerebral Blood Flow Velocity Responses to Changes in Posture.' en. In: *Archives of Disease in Childhood* 69.3 Spec No (Sept. 1993), pp. 304–308. ISSN: 0003-9888, 1468-2044. DOI: 10.1136/adc.69.3_Spec_No.304.

URL: https://adc.bmj.com/content/69/3_Spec_No/304 (visited on 16/04/2019).

[25] Isidor Kokalari, Theodhor Karaja and Maria Guerrisi. 'Review on Lumped Parameter Method for Modeling the Blood Flow in Systemic Arteries'. en. In: *Journal of Biomedical Science and Engineering* 06.01 (2013), pp. 92–99. ISSN: 1937-6871, 1937-688X. DOI: 10.4236/jbise.2013.61012. URL: http://www.scirp.org/journal/doi.aspx?DOI=10.4236/jbise.2013.61012 (visited on 30/12/2018).

[26] Patricia Garcia-Canadilla et al. 'Patient-Specific Estimates of Vascular and Placental Properties in Growth-Restricted Fetuses Based on a Model of the Fetal Circulation'. en. In: *Placenta* 36.9 (Sept. 2015), pp. 981–989. ISSN: 01434004. DOI: 10.1016/j.placenta.2015.07.130. URL: https://linkinghub.elsevier.com/retrieve/pii/S0143400415300242 (visited on 12/03/2019).

[27] Thanh Q. Nguyen. 'A Lumped Parameters Model for Cerebral Blood Flow in Neonates and Infants with Patent Ductus Arteriosus'. Master Thesis. Trondheim: Norwegian University of Science and Technology, June 2019.

[28] Patricia Garcia-Canadilla et al. 'A Computational Model of the Fetal Circulation to Quantify Blood Redistribution in Intrauterine Growth Restriction'. In: *PLoS Computational Biology* 10.6 (June 2014). ISSN: 1553-734X. DOI: 10.1371/journal.pcbi.1003667. URL: https://www.ncbi.nlm.nih.gov/pmc/articles/PMC4055406/ (visited on 31/12/2018).

[29] Alex Khiem Dinh Tran. 'Modelling and Monitoring Bloodflow in Premature Infants with Open Ductus Asteriosus Using Ultrasound Doppler Technique'. Master Thesis. Trondheim: NTNU, June 2018.

[30] Anna Karoline Wisløff. 'Modeling of Peripheral Resistance in the Microvasculature for Diabetic Patients with Ultrasound Doppler Technique'. Master Thesis. Trondheim: NTNU, June 2018.

[31] 'The World English Bible'.

[32] Michael Schünke et al. *Thieme Atlas of Anatomy*. English. OCLC: 974551099. 2015. ISBN: 978-1-60406-923-5 978-1-62623-167-2 978-1-62623-169-6.

[33] E. Römmler, G. Leopold and Th. Leisewitz. *An Injected Arterial Vessel System of a 9 Month Old Foetus.* URL: https://commons.wikimedia.org/wiki/File:An_injected_arterial_vessel_system_of_a_9_month_old_foetus._Wellcome_L0043613.jpg (visited on 05/06/2019).

[34] Henry Vandyke Carter, Henry Gray and Start this Book. *English: The Internal Carotid and Vertebral Arteries. Right Side.* before 1858 date QS:P,+1858-00-00T00:00:00Z/7,P1326,+1858-00-00T00:00:00Z/9. URL: https://commons.wikimedia.org/wiki/File:Gray513.png (visited on 05/06/2019).

[35] Dr Johannes Sobotta. *English: An Anatomical Illustration.* 1909. URL: https://commons.wikimedia.org/wiki/File:Sobotta.3.1909.549.png (visited on 05/06/2019).

[36] Dr Johannes Sobotta. *English: Arteries of the Brain, Seen Caudaly*. 21 October 2013, 19:52:37. URL: https://commons.wikimedia.org/wiki/File:Sobo_1909_3_548.png (visited on 05/06/2019).

[37] C. Malamateniou et al. 'The Anatomic Variations of the Circle of Willis in Preterm-at-Term and Term-Born Infants: An MR Angiography Study at 3T'. en. In: *American Journal of Neuroradiology* 30.10 (Nov. 2009), pp. 1955–1962. ISSN: 0195-6108, 1936-959X. DOI: 10.3174/ajnr.A1724. URL: http://www.ajnr.org/lookup/doi/10.3174/ajnr.A1724 (visited on 11/06/2019).

[38] Guy Lazorthes et al. 'Le cercle artériel du cerveau (circulus arteriosus cerebri)'. fr. In: *Anatomia Clinica* 1.3 (Sept. 1979), pp. 241–257. ISSN: 0343-608X, 1279-8517. DOI: 10.1007/BF01654581. URL: http://link.springer.com/10.1007/BF01654581 (visited on 11/06/2019).

[39] M. H. Johnson and M. H. Johnson. *Essential Reproduction*. Seventh edition. Essentials. Chichester, West Sussex: Wiley-Blackwell, 2013. ISBN: 978-1-4443-3575-0.

[40] OpenStax College. *The Fetal Circulatory System Includes Three Shunts to Divert Blood from Undeveloped and Partially Functioning Organs, as Well as Blood Supply to and from the Placenta.* Dec. 2013. URL: https://commons.wikimedia.org/wiki/File:2916_Fetal_Circulatory_System-02.jpg (visited on 05/06/2019).

[41] Torvid Kiserud, Svein Rasmussen and Svein Skulstad. 'Blood Flow and the Degree of Shunting through the Ductus Venosus in the Human Fetus'. English. In: *American Journal of Obstetrics & Gynecology* 182.1 (Jan. 2000), pp. 147–153. ISSN: 0002-9378, 1097-6868. DOI: 10.1016/S0002-9378(00)70504-7. URL: https://www.ajog.org/article/S0002-9378(00)70504-7/abstract (visited on 05/06/2019).

[42] Hiroyuki Nagasawa et al. 'Time to Spontaneous Ductus Arteriosus Closure in Full-Term Neonates'. en. In: *Open Heart* 3.1 (May 2016), e000413. ISSN: 2053-3624. DOI: 10.1136/openhrt-2016-000413. URL: http://openheart.bmj.com/lookup/doi/10.1136/openhrt-2016-000413 (visited on 05/06/2019).

[43] Tom Lissauer and Graham Clayden, eds. *Illustrated Textbook of Paediatrics*. 4th ed. Edinburgh: Mosby, 2012. ISBN: 978-0-7234-3565-5 978-0-7234-3566-2.

[44] Walter F. Boron and Emile L. Boulpaep, eds. *Medical Physiology*. Third edition. Philadelphia, PA: Elsevier, 2017.
ISBN: 978-1-4557-4377-3 978-0-323-42796-8 978-0-323-31973-7.

[45] Kelvinsong. *English: Diagram of Arteries, Veins, and Capillaries. Also Shows Cross-Sectional Area Differences. Aligned to 720 × 496 Px Grid.*
17 March 2013, 18:49:21.
URL: https://commons.wikimedia.org/wiki/File:Blood_vessels-en.svg (visited on 05/06/2019).

[46] Rice University.
20.2 Blood Flow, Blood Pressure, and Resistance – Anatomy and Physiology.
URL: https://opentextbc.ca/anatomyandphysiology/chapter/20-2-blood-flow-blood-pressure-and-resistance/ (visited on 05/06/2019).

[47] Agamemnon Despopoulos and Stefan Silbernagl. *Color Atlas of Physiology*. eng. 5. ed., compl. rev. and expanded. Thieme Flexibook. OCLC: 249073031. Stuttgart: Thieme, 2003. ISBN: 978-3-13-545005-6 978-1-58890-061-6.

[48] María Teresa Politi et al.
'The Dicrotic Notch Analyzed by a Numerical Model'. en.
In: *Computers in Biology and Medicine* 72 (May 2016), pp. 54–64.
ISSN: 00104825. DOI: 10.1016/j.compbiomed.2016.03.005.
URL: https://linkinghub.elsevier.com/retrieve/pii/S0010482516300592 (visited on 14/04/2019).

[49] xavax, adh30 and DanielChangMD. *English: A Wiggers Diagram, Showing the Cardiac Cycle Events Occuring in the Left Ventricle.* July 2016.
URL: https://commons.wikimedia.org/wiki/File:Wiggers_Diagram_2.svg (visited on 05/06/2019).

[50] I. Hudson et al. 'Reproducibility of Measurements of Cardiac Output in Newborn Infants by Doppler Ultrasound.' en.
In: *Archives of Disease in Childhood* 65.1 Spec No (Jan. 1990), p. 15. URL: https://www.ncbi.nlm.nih.gov/pmc/articles/PMC1590175/ (visited on 14/04/2019).

[51] Frans J. Walther et al. 'Pulsed Doppler Determinations of Cardiac Output in Neonates: Normal Standards for Clinical Use'. en.
In: *Pediatrics* 76.5 (Nov. 1985), pp. 829–833. ISSN: 0031-4005, 1098-4275.
URL: https://pediatrics.aappublications.org/content/76/5/829 (visited on 12/06/2019).

[52] Neil Patel, Melissa Dodsworth and John F. Mills.
'Cardiac Output Measurement in Newborn Infants Using the Ultrasonic Cardiac Output Monitor: An Assessment of Agreement with Conventional Echocardiography, Repeatability and New User Experience'. en. In: *Archives of Disease in Childhood - Fetal and Neonatal Edition* 96.3 (May 2011), F206–F211.

ISSN: 1359-2998, 1468-2052. DOI: 10.1136/adc.2009.170704. URL: https://fn.bmj.com/content/96/3/f206 (visited on 12/06/2019).

[53] F. J. Walther, B. Siassi and P. Y. Wu. 'Echocardiographic Measurement of Left Ventricular Stroke Volume in Newborn Infants: A Correlative Study with Pulsed Doppler and M-Mode Echocardiography'. eng.
In: *Journal of clinical ultrasound: JCU* 14.1 (Jan. 1986), pp. 37–41.
ISSN: 0091-2751.

[54] Susannah Fleming et al.
'Normal Ranges of Heart Rate and Respiratory Rate in Children from Birth to 18 Years of Age: A Systematic Review of Observational Studies'.
In: *The Lancet* 377.9770 (Mar. 2011), pp. 1011–1018. ISSN: 0140-6736.
DOI: 10.1016/S0140-6736(10)62226-X.
URL: http://www.sciencedirect.com/science/article/pii/S014067361062226X (visited on 12/06/2019).

[55] Sabine L. Vrancken, Arno F. van Heijst and Willem P. de Boode.
'Neonatal Hemodynamics: From Developmental Physiology to Comprehensive Monitoring'. In: *Frontiers in Pediatrics* 6 (Apr. 2018). ISSN: 2296-2360.
DOI: 10.3389/fped.2018.00087. URL:
https://www.ncbi.nlm.nih.gov/pmc/articles/PMC5895966/ (visited on 16/01/2019).

[56] N. Gullberg, P. Winberg and H. Selldén.
'Changes in Stroke Volume Cause Change in Cardiac Output in Neonates and Infants When Mean Airway Pressure Is Altered'. en.
In: *Acta Anaesthesiologica Scandinavica* 43.10 (1999), pp. 999–1004.
ISSN: 1399-6576. DOI: 10.1034/j.1399-6576.1999.431005.x.
URL: https://onlinelibrary.wiley.com/doi/abs/10.1034/j.1399-6576.1999.431005.x (visited on 19/04/2019).

[57] James F. Kenny et al.
'Effects of Heart Rate on Ventricular Size, Stroke Volume, and Output in the Normal Human Fetus: A Prospective Doppler Echocardiographic Study.'
In: *Circulation* 76.1 (1987), pp. 52–58. DOI: 10.1161/01.CIR.76.1.52.

[58] S. Hassan and P. Turner.
'Systolic Time Intervals: A Review of the Method in the Non-Invasive Investigation of Cardiac Function in Health, Disease and Clinical Pharmacology.'
In: *Postgraduate Medical Journal* 59.693 (July 1983), pp. 423–434.
ISSN: 0032-5473. URL:
https://www.ncbi.nlm.nih.gov/pmc/articles/PMC2417541/ (visited on 14/04/2019).

[59] Wolfgang Lindner et al. 'Heart Rate and Systolic Time Intervals in Healthy Newborn Infants: Longitudinal Study'. en.
In: *Pediatric Cardiology* 6.3 (Sept. 1985), pp. 117–121.
ISSN: 0172-0643, 1432-1971. DOI: 10.1007/BF02336549.

URL: http://link.springer.com/10.1007/BF02336549 (visited on 14/04/2019).

[60] Golde David and Burstin Luis.
'Systolic Phases of the Cardiac Cycle in Children'.
In: *Circulation* 42.6 (Dec. 1970), pp. 1029–1036.
DOI: 10.1161/01.CIR.42.6.1029. URL: https://www.ahajournals.org/doi/abs/10.1161/01.cir.42.6.1029 (visited on 15/04/2019).

[61] Roberto Sarnari et al.
'Doppler Assessment of the Ratio of the Systolic to Diastolic Duration in Normal Children: Relation to Heart Rate, Age and Body Surface Area'. In: *Journal of the American Society of Echocardiography* 22.8 (Aug. 2009), pp. 928–932.
ISSN: 0894-7317. DOI: 10.1016/j.echo.2009.05.004.
URL: http://www.sciencedirect.com/science/article/pii/S0894731709004386 (visited on 15/04/2019).

[62] Vinay Kumar et al., eds. *Robbins Basic Pathology*. Tenth edition.
Philadelphia, Pennsylvania: Elsevier, 2018. ISBN: 978-0-323-35317-5.

[63] Lawrence C. Perlmuter et al. 'A Review of Orthostatic Blood Pressure Regulation and Its Association with Mood and Cognition'. en.
In: *Clinical Autonomic Research* 22.2 (Apr. 2012), pp. 99–107. ISSN: 1619-1560.
DOI: 10.1007/s10286-011-0145-3.
URL: https://doi.org/10.1007/s10286-011-0145-3 (visited on 07/06/2019).

[64] Gang Yuan, Bingxue Qi and Qi Luo.
'Mechanisms of Cerebrovascular Autoregulation and Spreading Depolarization-Induced Autoregulatory Failure: A Literature Review'. en.
In: (), p. 8.

[65] Mogens Fog. 'CEREBRAL CIRCULATION: THE REACTION OF THE PIAL ARTERIES TO A FALL IN BLOOD PRESSURE'. en.
In: *Archives of Neurology & Psychiatry* 37.2 (Feb. 1937), pp. 351–364.
ISSN: 0096-6754.
DOI: 10.1001/archneurpsyc.1937.02260140137007.
URL: https://jamanetwork.com/journals/archneurpsyc/fullarticle/647072 (visited on 17/04/2019).

[66] H. S. Forbes. 'THE CEREBRAL CIRCULATION: I. OBSERVATION AND MEASUREMENT OF PIAL VESSELS'. en.
In: *Archives of Neurology & Psychiatry* 19.5 (May 1928), pp. 751–761.
ISSN: 0096-6754.
DOI: 10.1001/archneurpsyc.1928.02210110003001.
URL: https://jamanetwork.com/journals/archneurpsyc/fullarticle/643964 (visited on 17/04/2019).

[67] Ambler Thompson and Barry N. Taylor.
Guide for the Use of the International System of Units (SI). en.
NIST Special Publication 811. 2008, p. 90.

[68] Yoshio Yamanouchi et al. 'Venous Dysfunction and the Change of Blood Viscosity During Head-Up Tilt'. en.
In: *Pacing and Clinical Electrophysiology* 21.3 (1998), pp. 520–527.
ISSN: 1540-8159. DOI: 10.1111/j.1540-8159.1998.tb00093.x.
URL: https://onlinelibrary.wiley.com/doi/abs/10.1111/j.1540-8159.1998.tb00093.x (visited on 13/06/2019).

[69] John Schutzman et al. 'Head-up Tilt and Hemodynamic Changes during Orthostatic Hypotension in Patients with Supine Hypertension'.
In: *Journal of the American College of Cardiology*. Bethesda Conference: Future Personnel Needs for Cardiovascular Health Care 24.2 (Aug. 1994), pp. 454–461.
ISSN: 0735-1097. DOI: 10.1016/0735-1097(94)90303-4.
URL: http://www.sciencedirect.com/science/article/pii/0735109794903034 (visited on 13/06/2019).

[70] Ana Diaz Artiles, Thomas Heldt and Laurence R. Young. 'Effects of Artificial Gravity on the Cardiovascular System: Computational Approach'. en.
In: *Acta Astronautica* 126 (Sept. 2016), pp. 395–410. ISSN: 00945765.
DOI: 10.1016/j.actaastro.2016.05.005.
URL: https://linkinghub.elsevier.com/retrieve/pii/S009457651530299X (visited on 17/01/2019).

[71] I. Murat et al.
'CONTINUOUS EXTRADURAL ANAESTHESIA IN CHILDREN'. en.
In: *British Journal of Anaesthesia* 59.11 (Nov. 1987), pp. 1441–1450.
ISSN: 00070912. DOI: 10.1093/bja/59.11.1441.
URL: https://linkinghub.elsevier.com/retrieve/pii/S0007091217432478 (visited on 13/06/2019).

[72] Meng Deng et al. 'The Hemodynamic Effects of Newborn Caudal Anesthesia Assessed by Transthoracic Echocardiography: A Randomized, Double-Blind, Controlled Study'. en.
In: *Pediatric Anesthesia* 18.11 (Nov. 2008), pp. 1075–1081.
ISSN: 11555645, 14609592.
DOI: 10.1111/j.1460-9592.2008.02786.x. URL: http://doi.wiley.com/10.1111/j.1460-9592.2008.02786.x (visited on 13/06/2019).

[73] Fabio Magrini et al. 'Cardiac Responses to Head up Tilt during Early Extrauterine Life: Relevance of Active Acquisition of Erect Posture'. en.
In: *Cardiovascular Research* 23.5 (May 1989), pp. 460–464. ISSN: 0008-6363.
DOI: 10.1093/cvr/23.5.460. URL: https://academic.oup.com/cardiovascres/article/23/5/460/436994 (visited on 07/05/2019).

[74] Kókay Szabolcs. *English: Newborn Son*. 2008.
URL: https://commons.wikimedia.org/wiki/File:Newborn_baby.jpg (visited on 16/04/2019).

[75] Roger S. Seymour and Joachim O. Arndt.
'Independent Effects of Heart–Head Distance and Caudal Blood Pooling on Blood Pressure Regulation in Aquatic and Terrestrial Snakes'. en.
In: *Journal of Experimental Biology* 207.8 (Mar. 2004), pp. 1305–1311.
ISSN: 0022-0949, 1477-9145. DOI: 10.1242/jeb.00882.
URL: http://jeb.biologists.org/content/207/8/1305 (visited on 08/06/2019).

[76] R A Wolthuis, S A Bergman and A E Nicogossian.
'Physiological Effects of Locally Applied Reduced Pressure in Man.' en.
In: *Physiological Reviews* 54.3 (July 1974), pp. 566–595.
ISSN: 0031-9333, 1522-1210. DOI: 10.1152/physrev.1974.54.3.566.
URL: http://www.physiology.org/doi/10.1152/physrev.1974.54.3.566 (visited on 08/06/2019).

[77] Anne-Sophie G. T. Bronzwaer et al. 'The Cerebrovascular Response to Lower-Body Negative Pressure vs. Head-up Tilt'.
In: *Journal of Applied Physiology* 122.4 (Jan. 2017), pp. 877–883.
ISSN: 8750-7587. DOI: 10.1152/japplphysiol.00797.2016.
URL: https://www.physiology.org/doi/full/10.1152/japplphysiol.00797.2016 (visited on 08/06/2019).

[78] Suvi Viskari-Lähdeoja et al. 'Acute Cardiovascular Responses in Preterm Infants at 34–39weeks of Gestational Age'.
In: *Early Human Development* 88.11 (Nov. 2012), pp. 871–877.
ISSN: 0378-3782. DOI: 10.1016/j.earlhumdev.2012.07.005.
URL: http://www.sciencedirect.com/science/article/pii/S0378378212001673 (visited on 08/05/2019).

[79] A. Edner et al. 'Heart Rate Response Profiles during Head Upright Tilt Test in Infants with Apparent Life Threatening Events'. en.
In: *Archives of Disease in Childhood* 76.1 (Jan. 1997), pp. 27–30.
ISSN: 0003-9888, 1468-2044. DOI: 10.1136/adc.76.1.27. URL: https://adc.bmj.com/content/76/1/27 (visited on 19/04/2019).

[80] B. C. Galland et al. 'Factors Affecting Heart Rate Variability and Heart Rate Responses to Tilting in Infants Aged 1 and 3 Months'. en.
In: *Pediatric Research* 48.3 (Sept. 2000), pp. 360–368. ISSN: 1530-0447.
DOI: 10.1203/00006450-200009000-00017.
URL: https://www.nature.com/articles/pr2000203 (visited on 13/06/2019).

[81] Jon E. Mazursky et al. 'Development of Baroreflex Influences on Heart Rate Variability in Preterm Infants'.
In: *Early Human Development* 53.1 (Nov. 1998), pp. 37–52. ISSN: 0378-3782.

DOI: 10.1016/S0378-3782(98)00038-3.
URL: http://www.sciencedirect.com/science/article/pii/S0378378298000383 (visited on 07/05/2019).

[82] S Viskari-Lähdeoja et al. 'Heart Rate and Blood Pressure Control in Infants Exposed to Maternal Cigarette Smoking'. en.
In: *Acta Paediatrica* 97.11 (Nov. 2008), pp. 1535–1541.
ISSN: 08035253, 16512227.
DOI: 10.1111/j.1651-2227.2008.00966.x. URL: http://doi.wiley.com/10.1111/j.1651-2227.2008.00966.x (visited on 06/05/2019).

[83] Stephanie R. Yiallourou et al. 'Maturation of Heart Rate and Blood Pressure Variability during Sleep in Term-Born Infants'. en. In: *SLEEP* (Feb. 2012).
ISSN: 0161-8105, 1550-9109. DOI: 10.5665/sleep.1616.
URL: https://academic.oup.com/sleep/article-lookup/doi/10.5665/sleep.1616 (visited on 06/05/2019).

[84] Karin Toska and Lars Walløe. 'Dynamic Time Course of Hemodynamic Responses after Passive Head-up Tilt and Tilt Back to Supine Position'.
In: *Journal of Applied Physiology* 92.4 (Apr. 2002), pp. 1671–1676.
ISSN: 8750-7587. DOI: 10.1152/japplphysiol.00465.2000.
URL: https://www.physiology.org/doi/full/10.1152/japplphysiol.00465.2000 (visited on 12/06/2019).

[85] Mark P. M. Harms et al. 'Postural Effects on Cardiac Output and Mixed Venous Oxygen Saturation in Humans'. en.
In: *Experimental Physiology* 88.5 (Sept. 2003), pp. 611–616. ISSN: 09580670.
DOI: 10.1113/eph8802580.
URL: http://doi.wiley.com/10.1113/eph8802580 (visited on 12/06/2019).

[86] L. A. H. Critchley et al.
'Non-Invasive Continuous Arterial Pressure, Heart Rate and Stroke Volume Measurements during Graded Head-up Tilt in Normal Man'. en.
In: *Clinical Autonomic Research* 7.2 (Apr. 1997), pp. 97–101.
ISSN: 0959-9851, 1619-1560. DOI: 10.1007/BF02267754.
URL: http://link.springer.com/10.1007/BF02267754 (visited on 12/06/2019).

[87] J Tuckman and J Shillingford. 'Effect of Different Degrees of Tilt on Cardiac Output, Heart Rate, and Blood Pressure in Normal Man.'
In: *British Heart Journal* 28.1 (Jan. 1966), pp. 32–39. ISSN: 0007-0769. URL: https://www.ncbi.nlm.nih.gov/pmc/articles/PMC459038/ (visited on 12/06/2019).

[88] Fl Abel and Ja Waldhausen. 'Influence of Posture and Passive Tilting on Venous Return and Cardiac Output'. en. In: *American Journal of Physiology-Legacy Content* 215.5 (Nov. 1968), pp. 1058–1066. ISSN: 0002-9513.
DOI: 10.1152/ajplegacy.1968.215.5.1058.

URL: http://www.physiology.org/doi/10.1152/ajplegacy.1968.215.5.1058 (visited on 12/06/2019).

[89] Hongxia Li et al.
'Head-up Tilt Test Provokes Dynamic Alterations in Total Peripheral Resistance and Cardiac Output in Children with Vasovagal Syncope'. en.
In: *Acta Paediatrica* 107.10 (2018), pp. 1786–1791. ISSN: 1651-2227.
DOI: 10.1111/apa.14342. URL: https://onlinelibrary.wiley.com/doi/abs/10.1111/apa.14342 (visited on 17/04/2019).

[90] P.S. Shekhawat, P. Sasidharan and D.A. Lewis.
'Myocardial Performance and Baroreceptor Reflexes in Preterm Neonates: An Echocardiographic Evaluation Using the Tilt-Table Test'. en.
In: *Pediatric Cardiology* 22.6 (Nov. 2001), pp. 465–470.
ISSN: 0172-0643, 1432-1971. DOI: 10.1007/s002460010276.
URL: http://link.springer.com/10.1007/s002460010276 (visited on 06/05/2019).

[91] G. Paviotti, S. Todero and S. Demarini.
'Cardiac Output Decreases and Systemic Vascular Resistance Increases in Newborns Placed in the Left-Lateral Position'. en.
In: *Journal of Perinatology* 37.5 (May 2017), pp. 563–565. ISSN: 1476-5543.
DOI: 10.1038/jp.2016.251.
URL: https://www.nature.com/articles/jp2016251 (visited on 07/05/2019).

[92] Gerhard Pichler et al.
'Effect of Tilting on Cerebral Hemodynamics in Preterm and Term Infants'.
In: *Neonatology* 80.3 (2001), pp. 179–185. ISSN: 1661-7800, 1661-7819.
DOI: 10.1159/000047140.
URL: https://www.karger.com/Article/FullText/47140 (visited on 16/04/2019).

[93] Iosif Aleksandrovič Brodskij. *Less than One: Selected Essays*. English.
OCLC: 751189455. New York: Farrar, Straus, Giroux, 1998.
ISBN: 978-0-374-52055-7.

[94] S. Campbell. 'A Short History of Sonography in Obstetrics and Gynaecology'.
In: *Facts, Views & Vision in ObGyn* 5.3 (2013), pp. 213–229. ISSN: 2032-0418.
URL:
https://www.ncbi.nlm.nih.gov/pmc/articles/PMC3987368/ (visited on 20/04/2019).

[95] Ian Donald, J. Macvicar and T. G. Brown. 'INVESTIGATION OF ABDOMINAL MASSES BY PULSED ULTRASOUND'. English.
In: *The Lancet* 271.7032 (June 1958), pp. 1188–1195.
ISSN: 0140-6736, 1474-547X. DOI: 10.1016/S0140-6736(58)91905-6.
URL: https://www.thelancet.com/journals/lancet/article/PIIS0140-6736(58)91905-6/abstract (visited on 20/04/2019).

[96] Dev Maulik. ‘Doppler Sonography: A Brief History’. en.
In: *Doppler Ultrasound in Obstetrics and Gynecology*. Ed. by Dev Maulik.
Berlin/Heidelberg: Springer-Verlag, 2005, pp. 1–7. ISBN: 978-3-540-23088-5.
DOI: 10.1007/3-540-28903-8_1.
URL: http://link.springer.com/10.1007/3-540-28903-8_1
(visited on 20/04/2019).

[97] M I Levene. ‘Is Neonatal Cerebral Ultrasound Just for the Voyeur?’
In: *Archives of Disease in Childhood* 63.1 (Jan. 1988), pp. 1–2. ISSN: 0003-9888.
URL:
https://www.ncbi.nlm.nih.gov/pmc/articles/PMC1779334/
(visited on 20/04/2019).

[98] Bjørn A. J. Angelsen. *Propagation and Scattering in Heterogeneous, Nonlinear Tissue with Contrast Agent Imaging and Doppler Measurements*. eng. Ultrasound Imaging waves, signals, and signal processing / Bjørn A. J. Angelsen ; Vol. 2.
OCLC: 249721883. Trondheim: Emantec AS, 2000. ISBN: 978-82-995811-2-7.

[99] Steve Webb and M. A. Flower, eds. *Webb’s Physics of Medical Imaging*. 2nd ed.
Series in Medical Physics and Biomedical Engineering.
Boca Raton: Taylor & Francis, 2012. ISBN: 978-0-7503-0573-0.

[100] Christian Doppler and Frantisek Josef Studnicka.
Ueber das farbige Licht der Doppelsterne und einiger anderer gestirne des Himmels. Versuch einer das Bradley’sche Aberrationstheorem als integrirenden Theil in sich schliessenden allgemeineren Theorie. Zur Feier seines hundertsten Geburtstages als erste Veröffentlichung des nach ihm benannten physikalischen Princips. Neu hrsg. von F.J. Studnicka. ger. Prag K. Böhm, 1903. URL:
http://archive.org/details/ueberdasfarbigel00doppuoft
(visited on 20/04/2019).

[101] Paul G. Newman and Grace S. Rozycki.
‘THE HISTORY OF ULTRASOUND’. en.
In: *Surgical Clinics of North America* 78.2 (Apr. 1998), pp. 179–195.
ISSN: 00396109. DOI: 10.1016/S0039-6109(05)70308-X.
URL: https://linkinghub.elsevier.com/retrieve/pii/
S003961090570308X (visited on 11/06/2019).

[102] H. Torp and L. Løvstakken. ‘Doppler Ultrasound’. en.
In: *Comprehensive Biomedical Physics*. Elsevier, 2014, pp. 343–360.
ISBN: 978-0-444-53633-4.
DOI: 10.1016/B978-0-444-53632-7.00216-1.
URL: https://linkinghub.elsevier.com/retrieve/pii/
B9780444536327002161 (visited on 20/04/2019).

[103] Jan M. Sohns et al. ‘Peak Flow Velocities in the Ascending Aorta—Real-Time Phase-Contrast Magnetic Resonance Imaging vs. Cine Magnetic Resonance Imaging and Echocardiography’.
In: *Quantitative Imaging in Medicine and Surgery* 5.5 (Oct. 2015), pp. 685–690.
ISSN: 2223-4292. DOI: 10.3978/j.issn.2223-4292.2015.08.08.

URL:
https://www.ncbi.nlm.nih.gov/pmc/articles/PMC4671970/
(visited on 10/06/2019).

[104] Ehud Grenadier et al. 'Normal Intracardiac and Great Vessel Doppler Flow Velocities in Infants and Children'.
In: *Journal of the American College of Cardiology* 4.2 (Aug. 1984), pp. 343–350.
ISSN: 0735-1097. DOI: 10.1016/S0735-1097(84)80224-7.
URL: http://www.sciencedirect.com/science/article/pii/S0735109784802247 (visited on 10/06/2019).

[105] Michael Hofbeck, Karl-Heinz Deeg and Thomas Rupprecht.
Doppler Echocardiography in Infancy and Childhood. en.
Cham: Springer International Publishing, 2017.
ISBN: 978-3-319-42917-5 978-3-319-42919-9.
DOI: 10.1007/978-3-319-42919-9.
URL: http://link.springer.com/10.1007/978-3-319-42919-9 (visited on 01/05/2019).

[106] Kieran R. O'Brien et al.
'MRI Phase Contrast Velocity and Flow Errors in Turbulent Stenotic Jets'. en.
In: *Journal of Magnetic Resonance Imaging* 28.1 (July 2008), pp. 210–218.
ISSN: 10531807, 15222586. DOI: 10.1002/jmri.21395.
URL: http://doi.wiley.com/10.1002/jmri.21395 (visited on 10/06/2019).

[107] Marco Pezzati et al. 'Early Postnatal Doppler Assessment of Cerebral Blood Flow Velocity in Healthy Preterm and Term Infants'. en.
In: *Developmental Medicine & Child Neurology* 44.11 (Feb. 2007), pp. 745–752.
ISSN: 00121622, 14698749.
DOI: 10.1111/j.1469-8749.2002.tb00281.x.
URL: http://doi.wiley.com/10.1111/j.1469-8749.2002.tb00281.x (visited on 23/06/2019).

[108] A C Fenton, D H Evans and M I Levene. 'On Line Cerebral Blood Flow Velocity and Blood Pressure Measurement in Neonates: A New Method.'
In: *Archives of Disease in Childhood* 65.1 Spec No (Jan. 1990), pp. 11–14.
ISSN: 0003-9888. URL:
https://www.ncbi.nlm.nih.gov/pmc/articles/PMC1590161/
(visited on 16/04/2019).

[109] T. Hergum. *Investigators Brochure EarlyBird*.
Investigators Brochure [Unpublished].
Trondheim: Kirurgisk klinikk ved St. Olavs Hospital HF, May 2017.

[110] NTNU TTO. *Neodoppler*.
URL: https://www.youtube.com/watch?v=U7Mva76yfnk (visited on 19/04/2019).

[111] Frank M. White. *Fluid Mechanics*. eng. 7. ed. in SI units. OCLC: 732182454.
Singapore: McGraw-Hill, 2011. ISBN: 978-0-07-131121-2.

[112] Mair Zamir. *Hemo-Dynamics*. English. OCLC: 1049995765.
Cham: Springer International Publishing, 2016. ISBN: 978-3-319-24103-6.
URL: https://doi.org/10.1007/978-3-319-24103-6 (visited on 04/06/2019).

[113] Karl Rottmann. *Matematisk formelsamling*. Norwegian. OCLC: 1028319192.
Oslo: Bracan forl., 2003. ISBN: 978-82-7822-005-4.

[114] Jaiyoung Ryu, Xiao Hu and Shawn C. Shadden. 'A Coupled Lumped-Parameter and Distributed Network Model for Cerebral Pulse-Wave Hemodynamics'.
In: *Journal of Biomechanical Engineering* 137.10 (Oct. 2015),
pp. 1010091–10100913. ISSN: 0148-0731. DOI: 10.1115/1.4031331. URL:
https://www.ncbi.nlm.nih.gov/pmc/articles/PMC4844230/
(visited on 08/03/2019).

[115] Francesco Costanzo and James G. Brasseur.
'The Invalidity of the Laplace Law for Biological Vessels and of Estimating Elastic Modulus from Total Stress vs. Strain: A New Practical Method'. en.
In: *Mathematical Medicine and Biology: A Journal of the IMA* 32.1 (Mar. 2015),
pp. 1–37. ISSN: 1477-8599. DOI: 10.1093/imammb/dqt020. URL:
https://academic.oup.com/imammb/article/32/1/1/661585
(visited on 14/06/2019).

[116] V. C. Rideout and D. E. Dick.
'Difference-Differential Equations for Fluid Flow in Distensible Tubes'. In: *IEEE Transactions on Biomedical Engineering* BME-14.3 (July 1967), pp. 171–177.
ISSN: 0018-9294. DOI: 10.1109/TBME.1967.4502495.
URL: http://ieeexplore.ieee.org/document/4502495/ (visited on 13/06/2019).

[117] Neil Storey. *Electronics: A Systems Approach*. 4th ed.
Harlow, England ; New York: Pearson/Prentice Hall, 2009.
ISBN: 978-0-273-71918-2.

[118] Kevin D. Lau and C. Alberto Figueroa.
'Simulation of Short-Term Pressure Regulation during the Tilt Test in a Coupled 3D–0D Closed-Loop Model of the Circulation'.
In: *Biomechanics and Modeling in Mechanobiology* 14.4 (2015), pp. 915–929.
ISSN: 1617-7959. DOI: 10.1007/s10237-014-0645-x. URL:
https://www.ncbi.nlm.nih.gov/pmc/articles/PMC4490186/
(visited on 17/01/2019).

[119] Kim H. Parker. 'A Brief History of Arterial Wave Mechanics'. In: *Medical & Biological Engineering & Computing* 47.2 (Feb. 2009), pp. 111–118.
ISSN: 0140-0118. DOI: 10.1007/s11517-009-0440-5. URL:
https://www.ncbi.nlm.nih.gov/pmc/articles/PMC2644374/
(visited on 14/06/2019).

[120] Nico Westerhof, Jan-Willem Lankhaar and Berend E. Westerhof. 'The Arterial Windkessel'. en. In: *Medical & Biological Engineering & Computing* 47.2 (Feb. 2009), pp. 131–141. ISSN: 1741-0444. DOI: 10.1007/s11517-008-0359-2. URL: https://doi.org/10.1007/s11517-008-0359-2 (visited on 15/06/2019).

[121] Greg Mader, Mette Olufsen and Adam Mahdi. 'Modeling Cerebral Blood Flow Velocity During Orthostatic Stress'. en. In: *Annals of Biomedical Engineering* 43.8 (Aug. 2015), pp. 1748–1758. ISSN: 0090-6964, 1573-9686. DOI: 10.1007/s10439-014-1220-4. URL: http://link.springer.com/10.1007/s10439-014-1220-4 (visited on 21/01/2019).

[122] Mette S. Olufsen, Ali Nadim and Lewis A. Lipsitz. 'Dynamics of Cerebral Blood Flow Regulation Explained Using a Lumped Parameter Model'. en. In: *American Journal of Physiology-Regulatory, Integrative and Comparative Physiology* (Feb. 2002). DOI: 10.1152/ajpregu.00285.2001. URL: https://www.physiology.org/doi/abs/10.1152/ajpregu.00285.2001 (visited on 29/01/2019).

[123] Mette Olufsen, Hien Tran and Johnny Ottesen. 'Modeling Cerebral Blood Flow Control During Posture Change from Sitting to Standing'. en. In: *Cardiovascular Engineering* 4.1 (Mar. 2004), pp. 47–58. ISSN: 1567-8822. DOI: 10.1023/B:CARE.0000025122.46013.1a. URL: http://link.springer.com/10.1023/B:CARE.0000025122.46013.1a (visited on 23/04/2019).

[124] Einly Lim et al. 'A Cardiovascular Mathematical Model of Graded Head-Up Tilt'. In: *PLoS ONE* 8.10 (Oct. 2013). ISSN: 1932-6203. DOI: 10.1371/journal.pone.0077357. URL: https://www.ncbi.nlm.nih.gov/pmc/articles/PMC3812216/ (visited on 15/06/2019).

[125] G. Pennati, M. Bellotti and R. Fumero. 'Mathematical Modelling of the Human Foetal Cardiovascular System Based on Doppler Ultrasound Data'. en. In: *Medical Engineering & Physics* 19.4 (June 1997), pp. 327–335. ISSN: 13504533. DOI: 10.1016/S1350-4533(97)84634-6. URL: https://linkinghub.elsevier.com/retrieve/pii/S1350453397846346 (visited on 15/06/2019).

[126] Carla D. Sá Couto et al. 'A Model for Educational Simulation of Neonatal Cardiovascular Pathophysiology'. en-US. In: *Simulation in Healthcare* 1.Inaugural (Jan. 2006), p. 4. ISSN: 1559-2332. URL: https://journals.lww.com/simulationinhealthcare/Fulltext/2006/00010/A_Model_for_Educational_Simulation_of_Neonatal.3.aspx (visited on 24/01/2019).

[127] Mariken Zijlmans et al. ‘Corrected and Improved Model for Educational Simulation of Neonatal Cardiovascular Pathophysiology’. eng.
In: *Simulation in Healthcare: Journal of the Society for Simulation in Healthcare* 4.1 (2009), pp. 49–53. ISSN: 1559-2332.
DOI: 10.1097/SIH.0b013e31818b27a8.

[128] Carla D Sá-Couto et al.
‘A Model for Educational Simulation of Hemodynamic Transitions at Birth’. en.
In: *Pediatric Research* 67.2 (Feb. 2010), pp. 158–165.
ISSN: 0031-3998, 1530-0447. DOI: 10.1203/PDR.0b013e3181c2def3.
URL: http://www.nature.com/doifinder/10.1203/PDR.0b013e3181c2def3 (visited on 07/02/2019).

[129] Juliana Sanchez-Posada, Alberto Garcıa Torres and Juan Carlos Briceno Triana. ‘Mathematical Model of the Human Fetal and Neonatal Circulation with Pulmonary Atresia’. en. In: (), p. 8.

[130] S. Soleymani et al. ‘Modeling of Neonatal Hemodynamics during PDA Closure’.
In: *2015 37th Annual International Conference of the IEEE Engineering in Medicine and Biology Society (EMBC)*. Aug. 2015, pp. 1886–1889.
DOI: 10.1109/EMBC.2015.7318750.

[131] W. Jennekens et al. ‘Validation of a Preterm Infant Cardiovascular System Model under Baroreflex Control with Heart Rate and Blood Pressure Data’.
In: *2011 Annual International Conference of the IEEE Engineering in Medicine and Biology Society*. Aug. 2011, pp. 896–899.
DOI: 10.1109/IEMBS.2011.6090200.

[132] Mauro Ursino. ‘Interaction between Carotid Baroregulation and the Pulsating Heart: A Mathematical Model’. In: *American Journal of Physiology-Heart and Circulatory Physiology* 275.5 (Nov. 1998), H1733–H1747. ISSN: 0363-6135.
DOI: 10.1152/ajpheart.1998.275.5.H1733.
URL: https://www.physiology.org/doi/full/10.1152/ajpheart.1998.275.5.H1733 (visited on 06/03/2019).

[133] Renée Lampe et al. ‘Mathematical Modelling of Cerebral Blood Circulation and Cerebral Autoregulation: Towards Preventing Intracranial Hemorrhages in Preterm Newborns’. en.
In: *Computational and Mathematical Methods in Medicine* 2014 (2014), pp. 1–9.
ISSN: 1748-670X, 1748-6718. DOI: 10.1155/2014/965275.
URL: http://www.hindawi.com/journals/cmmm/2014/965275/ (visited on 21/01/2019).

[134] *System Modeling and Simulation - MATLAB & Simulink Solutions*. en.
URL: https://se.mathworks.com/solutions/system-design-simulation.html (visited on 16/06/2019).

[135] *Physical Systems Simulation - Simscape*. en.
URL: https://se.mathworks.com/products/simscape.html (visited on 16/06/2019).

[136] *How Simscape Simulation Works - MATLAB & Simulink - MathWorks Nordic*. URL: https://se.mathworks.com/help/physmod/simscape/ug/how-simscape-simulation-works.html (visited on 16/06/2019).

[137] Martin Ystgaard and Henrik Holmstrøm. *Pediatriveiledere fra Norsk barnelegeforening*. no. URL: https://www.helsebiblioteket.no/pediatriveiledere?key=144572%5C&menuitemkeylev1=5962%5C&menuitemkeylev2=5970 (visited on 07/06/2019).

[138] M. Danielsen and J. T. Ottesen. '7. A Baroreceptor Model'. en. In: *Applied Mathematical Models in Human Physiology*. Society for Industrial and Applied Mathematics, Jan. 2004, pp. 157–196. ISBN: 978-0-89871-539-2 978-0-89871-828-7. DOI: 10.1137/1.9780898718287.ch7. URL: http://epubs.siam.org/doi/10.1137/1.9780898718287.ch7 (visited on 19/04/2019).

[139] T Kusaka. 'Cerebral Distribution of Cardiac Output in Newborn Infants'. en. In: *Archives of Disease in Childhood - Fetal and Neonatal Edition* 90.1 (Jan. 2005), F77–F78. ISSN: 1359-2998, 1468-2052. DOI: 10.1136/adc.2004.058487. URL: http://fn.bmj.com/cgi/doi/10.1136/adc.2004.058487 (visited on 14/04/2019).

[140] Adam Phillips. *Side Effects*. OCLC: ocm77573793. New York: Harper Perennial, 2007. ISBN: 978-0-00-715538-5.

[141] Wagner H. Bridger, Beverly M. Birns and Marion Blank. 'A Comparison of Behavioral Ratings and Heart Rate Measurements in Human Neonates:' en. In: *Psychosomatic Medicine* 27.2 (Mar. 1965), pp. 123–134. ISSN: 0033-3174. DOI: 10.1097/00006842-196503000-00005. URL: https://insights.ovid.com/crossref?an=00006842-196503000-00005 (visited on 22/06/2019).

[142] Phillips. *IntelliVue Patient Monitor MP20/30, MP40/50, MP60/70/80/90*. Instructions for Use. URL: https://umanitoba.ca/faculties/health_sciences/medicine/units/anesthesia/media/Philips_MP20-90.pdf (visited on 20/06/2019).

[143] Shwetal Lalan and Douglas Blowey. 'Comparison between Oscillometric and Intra-Arterial Blood Pressure Measurements in Ill Preterm and Full-Term Neonates'. English. In: *Journal of the American Society of Hypertension* 8.1 (Jan. 2014), pp. 36–44. ISSN: 1933-1711, 1878-7436. DOI: 10.1016/j.jash.2013.10.003. URL: https://www.ashjournal.com/article/S1933-1711(13)00173-3/abstract (visited on 20/06/2019).

[144] J. A. Low et al. ‘Validity of Newborn Oscillometric Blood Pressure’. eng. In: *Clinical and Investigative Medicine. Medecine Clinique Et Experimentale* 18.3 (June 1995), pp. 163–167. ISSN: 0147-958X.

[145] Ingrid Dannevig et al. ‘Blood Pressure in the Neonate: Three Non-Invasive Oscillometric Pressure Monitors Compared with Invasively Measured Blood Pressure’. en. In: *Acta Paediatrica* 94.2 (2005), pp. 191–196. ISSN: 1651-2227. DOI: 10.1111/j.1651-2227.2005.tb01889.x. URL: https://onlinelibrary.wiley.com/doi/abs/10.1111/j.1651-2227.2005.tb01889.x (visited on 20/06/2019).

[146] Bruce S. Alpert, David Quinn and David Gallick. ‘Oscillometric Blood Pressure: A Review for Clinicians’. In: *Journal of the American Society of Hypertension* 8.12 (Dec. 2014), pp. 930–938. ISSN: 1933-1711. DOI: 10.1016/j.jash.2014.08.014. URL: http://www.sciencedirect.com/science/article/pii/S1933171114007487 (visited on 20/06/2019).

[147] Sascha Meyer et al. ‘Agreement of Invasive versus Non-Invasive Blood Pressure in Preterm Neonates Is Not Dependent on Birth Weight or Gestational Age’. en. In: *Journal of Paediatrics and Child Health* 46.5 (2010), pp. 249–254. ISSN: 1440-1754. DOI: 10.1111/j.1440-1754.2009.01679.x. URL: https://onlinelibrary.wiley.com/doi/abs/10.1111/j.1440-1754.2009.01679.x (visited on 20/06/2019).

[148] Tomoyuki Shimokaze, Kazuhiro Akaba and Emi Saito. ‘Oscillometric and Intra-Arterial Blood Pressure in Preterm and Term Infants: Extent of Discrepancy and Factors Associated with Inaccuracy’. en. In: *American Journal of Perinatology* 32.3 (Feb. 2015), pp. 277–282. ISSN: 0735-1631, 1098-8785. DOI: 10.1055/s-0034-1383851. URL: http://www.thieme-connect.de/DOI/DOI?10.1055/s-0034-1383851 (visited on 20/06/2019).

[149] Sahin Takci et al. ‘Comparison between Oscillometric and Invasive Blood Pressure Measurements in Critically Ill Premature Infants’. en. In: *Acta Paediatrica* 101.2 (2012), pp. 132–135. ISSN: 1651-2227. DOI: 10.1111/j.1651-2227.2011.02458.x. URL: https://onlinelibrary.wiley.com/doi/abs/10.1111/j.1651-2227.2011.02458.x (visited on 20/06/2019).

[150] Zhe-Zhe Peng et al. ‘The Agreement between Oscillometric and Intra-Arterial Technique for Blood Pressure Monitoring in the Lower Extremities for Infants and Toddlers Undergoing Aortic Coarctation Repair’. en. In: *Pediatric Anesthesia* 26.11 (2016), pp. 1091–1096. ISSN: 1460-9592. DOI: 10.1111/pan.12989. URL: https://onlinelibrary.wiley.com/doi/abs/10.1111/pan.12989 (visited on 20/06/2019).

[151] J. Zhou, O. Elkhateeb and K.-S. Lee. ‘Comparison of Non-Invasive vs Invasive Blood Pressure Measurement in Neonates Undergoing Therapeutic Hypothermia for Hypoxic Ischemic Encephalopathy’. en.
In: *Journal of Perinatology* 36.5 (May 2016), pp. 381–385. ISSN: 1476-5543. DOI: 10.1038/jp.2015.198.
URL: https://www.nature.com/articles/jp2015198 (visited on 20/06/2019).

[152] Andrea Stebor. ‘BASIC PRINCIPLES OF NONINVASIVE BLOOD PRESSURE MEASUREMENT IN INFANTS’. ENGLISH.
In: *Advances in Neonatal Care* 5.5 (Oct. 2005), pp. 252–261. ISSN: 1536-0903. DOI: 10.1016/j.adnc.2005.06.005.
URL: insights.ovid.com (visited on 21/06/2019).

[153] Finlay A McAlister and Sharon E Straus.
‘Measurement of Blood Presssure: An Evidence Based Review’.
In: *BMJ : British Medical Journal* 322.7291 (Apr. 2001), pp. 908–911.
ISSN: 0959-8138. URL:
https://www.ncbi.nlm.nih.gov/pmc/articles/PMC1120072/
(visited on 21/06/2019).

[154] J. Alastruey et al. ‘Reduced Modelling of Blood Flow in the Cerebral Circulation: Coupling 1-D, 0-D and Cerebral Auto-Regulation Models’. en. In: *International Journal for Numerical Methods in Fluids* 56.8 (2008), pp. 1061–1067.
ISSN: 1097-0363. DOI: 10.1002/fld.1606. URL: https://onlinelibrary.wiley.com/doi/abs/10.1002/fld.1606
(visited on 16/01/2019).

[155] Lisa Prahl Wittberg et al. ‘Effects of Aortic Irregularities on Blood Flow’.
In: *Biomechanics and Modeling in Mechanobiology* 15 (2016), pp. 345–360.
ISSN: 1617-7959. DOI: 10.1007/s10237-015-0692-y. URL:
https://www.ncbi.nlm.nih.gov/pmc/articles/PMC4792364/
(visited on 21/06/2019).

[156] Theresa A. Tacy, Roger P. Vermilion and Achi Ludomirsky.
‘Range of Normal Valve Annulus Size in Neonates’. en.
In: *The American Journal of Cardiology* 75.7 (Mar. 1995), pp. 541–543.
ISSN: 00029149. DOI: 10.1016/S0002-9149(99)80605-5.
URL: https://linkinghub.elsevier.com/retrieve/pii/S0002914999806055 (visited on 14/04/2019).

[157] Frans J. Walther et al.
‘Normal Values of Aortic Root Measurements in Neonates’. en.
In: *Pediatric Cardiology* 6.2 (June 1985), pp. 61–63. ISSN: 1432-1971.
DOI: 10.1007/BF02282739.
URL: https://doi.org/10.1007/BF02282739 (visited on 16/06/2019).

[158] Henry Halliday et al. ‘Echographic Ventricular Systolic Time Intervals in Normal Term and Preterm Neonates’. en. In: *Pediatrics* 62.3 (Sept. 1978), pp. 317–321.
ISSN: 0031-4005, 1098-4275. URL: https:

//pediatrics.aappublications.org/content/62/3/317 (visited on 23/06/2019).

[159] H. P. Gutgesell et al. ‘Left and Right Ventricular Systolic Time Intervals in the Newborn. Usefulness and Limitation in Distinguishing Respiratory Disease from Transposition of the Great Arteries’. eng.
In: *British Heart Journal* 42.1 (July 1979), pp. 27–34. ISSN: 0007-0769.
DOI: 10.1136/hrt.42.1.27.

[160] Shahab Noori et al. ‘Changes in Myocardial Function and Hemodynamics after Ligation of the Ductus Arteriosus in Preterm Infants’.
In: *The Journal of Pediatrics* 150.6 (June 2007), pp. 597–602. ISSN: 0022-3476.
DOI: 10.1016/j.jpeds.2007.01.035.
URL: http://www.sciencedirect.com/science/article/pii/S0022347607001060 (visited on 06/03/2019).

[161] P. B. Tsivyan and A. D. Vasenina. ‘Left Ventricular Systolic and Diastolic Function in Term Neonates after Mild Perinatal Asphyxia’. eng.
In: *European Journal of Obstetrics, Gynecology, and Reproductive Biology* 40.2 (July 1991), pp. 105–110. ISSN: 0301-2115.

[162] Youtaro Agata et al.
‘Changes in Left Ventricular Output from Fetal to Early Neonatal Life’. English.
In: *The Journal of Pediatrics* 119.3 (Sept. 1991), pp. 441–445.
ISSN: 0022-3476, 1090-123X. DOI: 10.1016/S0022-3476(05)82060-8.
URL: https://www.jpeds.com/article/S0022-3476(05)82060-8/abstract (visited on 23/06/2019).

[163] Hiroyuki Nagasawa. ‘Evaluation of Left Ventricular Volumes in the Early Neonatal Period Using Three-Dimensional Echocardiography’. en.
In: *Cardiology in the Young* 24.4 (Aug. 2014), pp. 685–693.
ISSN: 1047-9511, 1467-1107. DOI: 10.1017/S1047951113000954.
URL: https://www.cambridge.org/core/journals/cardiology-in-the-young/article/evaluation-of-left-ventricular-volumes-in-the-early-neonatal-period-using-threedimensional-echocardiography/8B20EC5F276ED22AF8E9C0D0DC31224A (visited on 23/06/2019).

[164] Laleh Zarrinkoob et al. ‘Blood Flow Distribution in Cerebral Arteries’.
In: *Journal of Cerebral Blood Flow & Metabolism* 35.4 (Apr. 2015), pp. 648–654.
ISSN: 0271-678X. DOI: 10.1038/jcbfm.2014.241. URL:
https://www.ncbi.nlm.nih.gov/pmc/articles/PMC4420884/ (visited on 02/05/2019).

[165] Jerzy Gielecki et al. ‘Morphometric and Volumetric Analysis of the Middle Cerebral Artery in Human Fetuses’. eng.
In: *Acta Neurobiologiae Experimentalis* 69.1 (2009), pp. 129–137.
ISSN: 0065-1400.

[166] Kristen DeVault et al.
‘Blood Flow in the Circle of Willis: Modeling and Calibration’. en.
In: *Multiscale Modeling & Simulation* 7.2 (Jan. 2008), pp. 888–909.
ISSN: 1540-3459, 1540-3467. DOI: 10.1137/07070231X.
URL: http://epubs.siam.org/doi/10.1137/07070231X (visited on 31/01/2019).

[167] Chi Zhang et al.
‘Modeling the Circle of Willis to Assess the Effect of Anatomical Variations on the Development of Unilateral Internal Carotid Artery Stenosis’. en.
In: *Bio-Medical Materials and Engineering* 24.1 (Jan. 2014), pp. 491–499.
ISSN: 0959-2989. DOI: 10.3233/BME-130835.
URL: https://content.iospress.com/articles/bio-medical-materials-and-engineering/bme835 (visited on 23/06/2019).

[168] Ilija D. Šutalo et al. ‘Modeling of Flow Through The Circle of Willis and Cerebral Vasculature to Assess The Effects of Changes In The Peripheral Small Cerebral Vasculature on The Inflows’. en. In: *Engineering Applications of Computational Fluid Mechanics* 8.4 (Jan. 2014), pp. 609–622.
ISSN: 1994-2060, 1997-003X. DOI: 10.1080/19942060.2014.11083311.
URL: http://www.tandfonline.com/doi/abs/10.1080/19942060.2014.11083311 (visited on 23/06/2019).

[169] Costantino Romagnoli et al. ‘Neonatal Color Doppler US Study: Normal Values of Cerebral Blood Flow Velocities in Preterm Infants in the First Month of Life’.
In: *Ultrasound in Medicine & Biology* 32.3 (Mar. 2006), pp. 321–331.
ISSN: 0301-5629. DOI: 10.1016/j.ultrasmedbio.2005.12.007.
URL: http://www.sciencedirect.com/science/article/pii/S0301562905004862 (visited on 09/04/2019).

[170] Richard E. Behrman et al. ‘Abnormal Cerebral Blood Flow Patterns in Preterm Infants with a Large Patent Ductus Arteriosus’. en.
In: *The Journal of Pediatrics* 101.4 (Oct. 1982), pp. 587–593. ISSN: 00223476.
DOI: 10.1016/S0022-3476(82)80715-4.
URL: https://linkinghub.elsevier.com/retrieve/pii/S0022347682807154 (visited on 22/06/2019).

[171] Myung Su Lee, Young Mi Hong and Kyung Hee Kim.
‘Changes of Cerebral Blood Flow Velocity before and after Closure of Ductus Arteriosus Using Doppler Ultrasound in Normal Full-Term Newborns’.
In: *Journal of the Korean Pediatric Society* 38.12 (Dec. 1995), pp. 1620–1628.
URL: https://www.kjp.or.kr/journal/view.php?number=1995381204 (visited on 22/06/2019).

[172] Frank van Bel et al.
‘Blood Velocity Wave Form Characteristics of Superior Mesenteric Artery and Anterior Cerebral Artery before and after Ductus Arteriosus Closure’. en.
In: *European Journal of Ultrasound* 2.3 (July 1995), pp. 183–189.
ISSN: 09298266. DOI: 10.1016/0929-8266(95)00098-C.

URL: https://linkinghub.elsevier.com/retrieve/pii/092982669500098C (visited on 22/06/2019).

[173] N. Stergiopulos, J. J. Meister and N. Westerhof. 'Determinants of Stroke Volume and Systolic and Diastolic Aortic Pressure'. en. In: *American Journal of Physiology-Heart and Circulatory Physiology* 270.6 (June 1996), H2050–H2059. ISSN: 0363-6135, 1522-1539. DOI: 10.1152/ajpheart.1996.270.6.H2050. URL: http://www.physiology.org/doi/10.1152/ajpheart.1996.270.6.H2050 (visited on 09/02/2019).

[174] Pablo J Blanco, Lucas O Müller and J David Spence. 'Blood Pressure Gradients in Cerebral Arteries: A Clue to Pathogenesis of Cerebral Small Vessel Disease'. In: *Stroke and Vascular Neurology* 2.3 (June 2017), pp. 108–117. ISSN: 2059-8696. DOI: 10.1136/svn-2017-000087. URL: https://www.ncbi.nlm.nih.gov/pmc/articles/PMC5628379/ (visited on 02/05/2019).

[175] Mark E Wagshul, Per K Eide and Joseph R Madsen. 'The Pulsating Brain: A Review of Experimental and Clinical Studies of Intracranial Pulsatility'. In: *Fluids and Barriers of the CNS* 8 (Jan. 2011), p. 5. ISSN: 2045-8118. DOI: 10.1186/2045-8118-8-5. URL: https://www.ncbi.nlm.nih.gov/pmc/articles/PMC3042979/ (visited on 16/01/2019).

[176] Janet R. Emery and Joyce L. Peabody. 'Head Position Affects Intracranial Pressure in Newborn Infants'. en. In: *The Journal of Pediatrics* 103.6 (Dec. 1983), pp. 950–953. ISSN: 00223476. DOI: 10.1016/S0022-3476(83)80728-8. URL: https://linkinghub.elsevier.com/retrieve/pii/S0022347683807288 (visited on 10/04/2019).

[177] J Gisolf et al. 'Human Cerebral Venous Outflow Pathway Depends on Posture and Central Venous Pressure'. In: *The Journal of Physiology* 560.Pt 1 (Oct. 2004), pp. 317–327. ISSN: 0022-3751. DOI: 10.1113/jphysiol.2004.070409. URL: https://www.ncbi.nlm.nih.gov/pmc/articles/PMC1665206/ (visited on 24/06/2019).

[178] D. A. Cunningham et al. 'Comparison of Cardiovascular Response to Passive Tilt in Young and Elderly Men'. eng. In: *Canadian Journal of Physiology and Pharmacology* 66.11 (Nov. 1988), pp. 1425–1432. ISSN: 0008-4212.

[179] William P. Fifer et al. 'Cardiorespiratory Responses to Bidirectional Tilts in Infants'. In: *Early Human Development* 55.3 (July 1999), pp. 265–279. ISSN: 0378-3782. DOI: 10.1016/S0378-3782(99)00026-2. URL: http://www.sciencedirect.com/science/article/pii/S0378378299000262 (visited on 07/05/2019).

[180] Lothar Schrod and Julia Walter. ‘Effect of Head-Up Body Tilt Position on Autonomic Function and Cerebral Oxygenation in Preterm Infants’.
In: *Neonatology* 81.4 (2002), pp. 255–259. ISSN: 1661-7800, 1661-7819.
DOI: 10.1159/000056756.
URL: https://www.karger.com/Article/FullText/56756 (visited on 16/04/2019).

[181] H D Dellagrammaticas et al. ‘Effect of Body Tilting on Physiological Functions in Stable Very Low Birthweight Neonates.’
In: *Archives of Disease in Childhood* 66.4 Spec No (Apr. 1991), pp. 429–432.
ISSN: 0003-9888. URL:
https://www.ncbi.nlm.nih.gov/pmc/articles/PMC1590292/
(visited on 07/05/2019).

[182] C. Harrington et al. ‘Cardiovascular Responses to Three Simple, Provocative Tests of Autonomic Activity in Sleeping Infants’. en.
In: *Journal of Applied Physiology* 91.2 (Aug. 2001), pp. 561–568.
ISSN: 8750-7587, 1522-1601. DOI: 10.1152/jappl.2001.91.2.561.
URL: http:
//www.physiology.org/doi/10.1152/jappl.2001.91.2.561
(visited on 06/05/2019).

[183] Carmel Harrington et al. ‘Altered Autonomic Function and Reduced Arousability in Apparent Life-Threatening Event Infants with Obstructive Sleep Apnea’. en.
In: *American Journal of Respiratory and Critical Care Medicine* 165.8 (Apr. 2002), pp. 1048–1054. ISSN: 1073-449X, 1535-4970.
DOI: 10.1164/ajrccm.165.8.2102059.
URL: http://www.atsjournals.org/doi/abs/10.1164/ajrccm.165.8.2102059 (visited on 06/05/2019).

[184] Cohen Gary et al. ‘Long-Term Reprogramming of Cardiovascular Function in Infants of Active Smokers’. In: *Hypertension* 55.3 (Mar. 2010), pp. 722–728.
DOI: 10.1161/HYPERTENSIONAHA.109.142695.
URL: https://www.ahajournals.org/doi/full/10.1161/HYPERTENSIONAHA.109.142695 (visited on 07/05/2019).

[185] Jing Lin et al. ‘Tilt Angles and Positive Response of Head-up Tilt Test in Children with Orthostatic Intolerance’. en.
In: *Cardiology in the Young* 25.1 (Jan. 2015), pp. 76–80.
ISSN: 1047-9511, 1467-1107. DOI: 10.1017/S1047951113001601.
URL: https://www.cambridge.org/core/product/identifier/S1047951113001601/type/journal_article (visited on 06/05/2019).

Appendix A

Additional Data

Table A.1: Summary of baseline values and tilt responses reported for different ages and tilt angles for healthy participants. Results in squared brackets indicate post-tilt values. Statistical significance indicated when stated in the reference.

Age	Tilt	HR	ΔHR [%]	SBP	ΔSBP [%]	MAP	ΔMAP [%]	DBP	ΔDBP [%]	Ref.
2 hours	30°	131.0(33)	0.2	55.0(14)	−3.3	38.6	−5.4	30.4(11)	−7.6	[22]
24 hours	30°	125.3(28)	4.2	57.9(13)	−1.6	41.2	−3.6	32.9(12)	−5.5	[22]
24–68 hours	30°	123.4(19)	2.2	–	–	–	–	–	–	[179]
8 days†	30°	141 [140]	−0.7	–	–	40 [45]	2.5	–	–	[180]
18(12) days†	30°	162.0(105)	0.0	73.0(110)	−0.7	51	5.9	40(79)	12.5	[90]
2.0(3) months	30°	133.8(12)	−0.5	–	–	–	–	–	–	[179]
4.0(3) months	30°	129.7(11)	−0.2	–	–	–	–	–	–	[179]
1 day	45°	115(3)	6.1 *	59(2)	3.4	42	2.4	33(1)	3.0	[21]
2 days	45°	121(2)	−0.8	64(1)	1.6	46	0.0	37(1)	0.0	[21]
3 days	45°	122(3)	5.7 *	67(2)	9.0 *	48	8.3	39(1)	5.1	[21]
4–7 days	45°	122(4)	2.5	68(2)	2.9	49	0.0	40(1)	−2.5	[21]
Neonate†	45°	149.2(47)	−2.8	63.7(36)	−0.6	43.9	−1.6	34.0(42)	−2.4	[181]
18(2) days†	45°	155(2)	−0.3	–	–	–	–	–	–	[81]
∼10 weeks†	45°	152(4)	1.2 *	–	–	–	–	–	–	[81]
3 months††	45°	–	0.8(24)	–	−1.2(30)	–	–	–	1.1(27)	[182]
3 months†††	45°	–	1.8(27)	–	0.2(25)	–	–	–	−0.2(24)	[182]
13(2) weeks††	45°	–	0.8(21)	–	−1.2(30)	–	–	–	–	[183]
13(2) weeks†††	45°	–	1.8(22)	–	0.1(25)	–	–	–	–	[183]
4(1) days	60°	113	7.9(7)	93	1.1(4)	77	1.9	69	2.4(4)	[184]
18(12) days†	60°	162.0(105)	1.2	73.0(110)	6.8	51	11.8	40(79)	17.5	[90]
19(3) days	60°	137	4.4(6)	107	2.9(12)	87	4.4	77	5.4(10)	[184]
91(5) days	60°	120	4.5(7)	90	3.5(13)	68	5.7	57	7.5(15)	[184]
375(8) days	60°	110	8.7(6)	89	7.0(14)	63	10.8	50	14.2(20)	[184]
11.0(23) years	80°	72(12)	−2.8	100(9)	5.0	68	5.9	52(9)	5.8	[185]

Continued on next page

Age	Tilt	HR	ΔHR [%]	SBP	ΔSBP [%]	MAP	ΔMAP [%]	DBP	ΔDBP [%]	Ref.
1 day	90°	115(3)	4.3	59(2)	1.7	42	2.4	33(1)	3.0	[21]
2 days	90°	121(2)	5.8	64(1)	7.8 *	46	4.3	37(1)	2.7	[21]
3 days	90°	122(3)	4.9	67(2)	6.0	48	4.2	39(1)	5.1	[21]
4–7 days	90°	122(4)	5.0 *	68(2)	10.3 **	49	8.2	40(1)	5.0 *	[21]
6 months	90°	–	–	–	–	74(6)	−1.4	–	–	[73]
18 months	90°	112(7)	13	–	–	80(6)	−1.3	–	–	[73]

† Born premature. †† Slow-Wave Sleep. ††† REM Sleep. $^{*}P < .05$. $^{**}P < .01$.

Table A.2: Relative change (%) in response to a 90° tilt. Case 1–8 are simulated results, whereas data is acquired experimentally from two neonates referred to as Joakim and Ida. For Joakim, a simulation was carried out with measured heart rate as input. These results are reported to the right of the slash (/). Details in sections 3.3.2 and 3.3.3. Abbreviations: C, cerebral; P, peripheral; HR, heart rate; q, flow rate; PI, pulsatility index; SBP, systolic blood pressure; MAP, mean arterial blood pressure; DBP, diastolic blood pressure.

Case	Regulation			Response in Joakim [%]						Response in Ida [%]					
#	C	P	HR	HR	q	PI	SBP	MAP	DBP	HR	q	PI	SBP	MAP	DBP
1	+	+	+	17/14	−26/−28	25/30	4/3	9/7	15/10	13	−20	17	3	8	14
2	+	−	+	48/14	−28/−39	6/52	−12/−14	−7/−16	−1/−22	30	−21	7	−6	−2	3
3	−	+	+	17/14	−27/−30	31/35	4/3	9/7	15/11	13	−21	18	3	8	14
4	−	−	+	46/14	−41/−54	36/106	−10/−13	−5/−15	0/−20	29	−29	20	−6	−1	3
5	+	+	−	0/0	−26/−28	37/38	4/4	6/5	8/6	0	−20	27	5	6	9
6	+	−	−	0/0	−35/−42	63/66	−17/−17	−21/−22	−28/−29	0	−24	32	−12	−16	−21
7	−	+	−	0/0	−30/−31	50/46	5/4	6/5	8/7	0	−23	30	5	6	9
8	−	−	−	0/0	−54/−57	118/133	−15/−16	−19/−20	−25/−27	0	−39	64	−11	−14	−18
Data				12	−24	17	19	27	16	3	−19	16	0	4	10

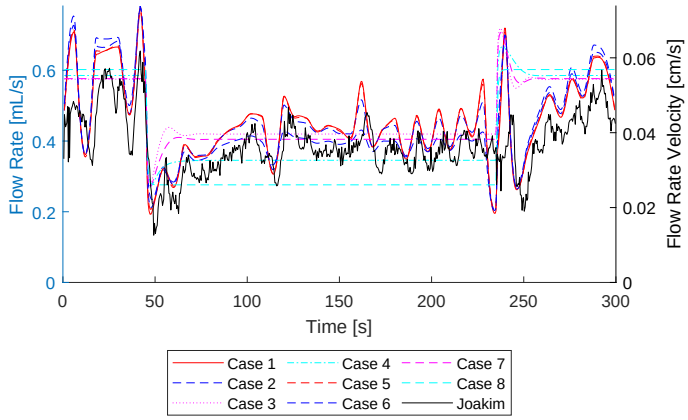

(a) Flow rate and flow velocity (black).

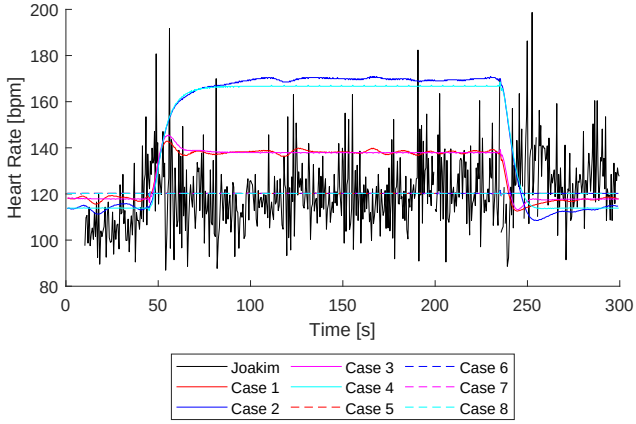

(b) Heart rate.

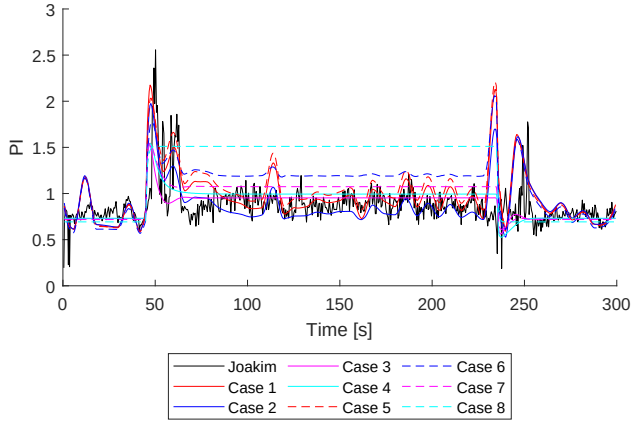

(c) Pulsatility Index (PI).

Figure A.1: Simulation of Joakim (cont. on next page).

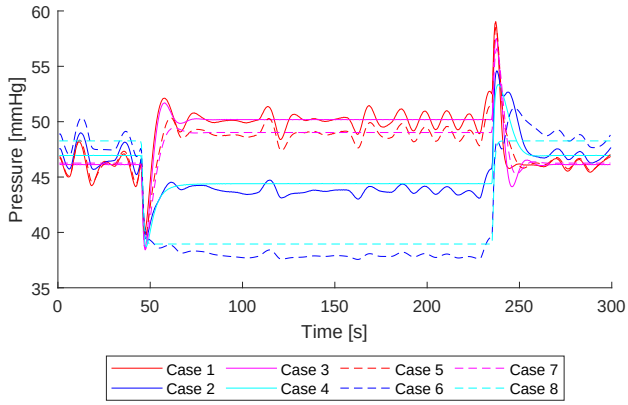

(d) Arterial Blood Pressure.

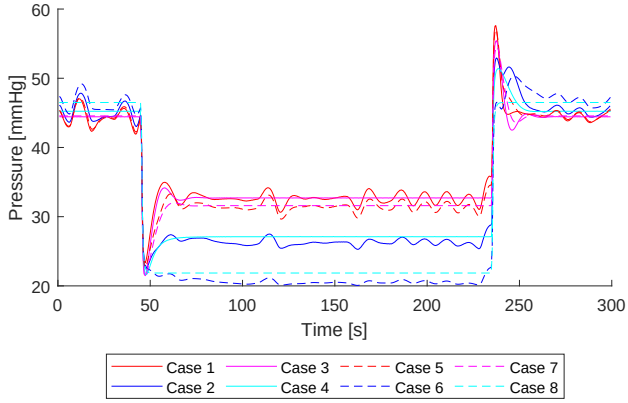

(e) Cerebral Blood Pressure.

Case #	1	2	3	4	5	6	7	8
Cerebral regulation	+	+	−	−	+	+	−	−
Peripheral regulation	+	−	+	−	+	−	+	−
HR regulation	+	+	+	+	−	−	−	−

Figure A.1: Simulation of Joakim. The table describes which regulatory mechanisms that are activate in each case.

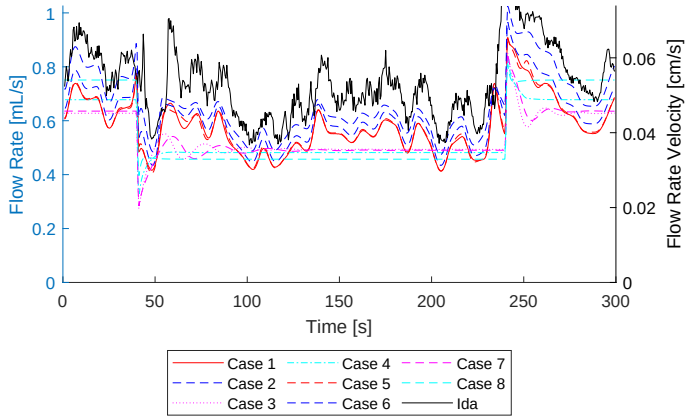

(a) Flow rate and flow velocity (black).

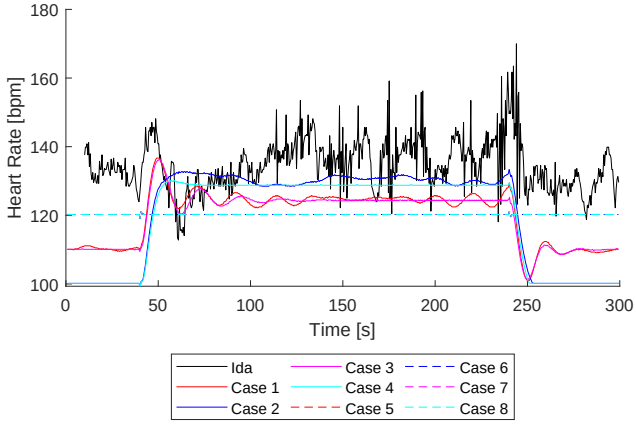

(b) Heart rate.

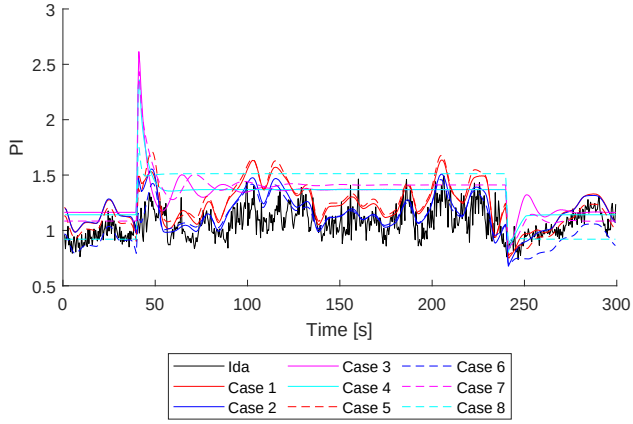

(c) Pulsatility Index (PI).

Figure A.2: Simulation of Ida (cont. on next page).

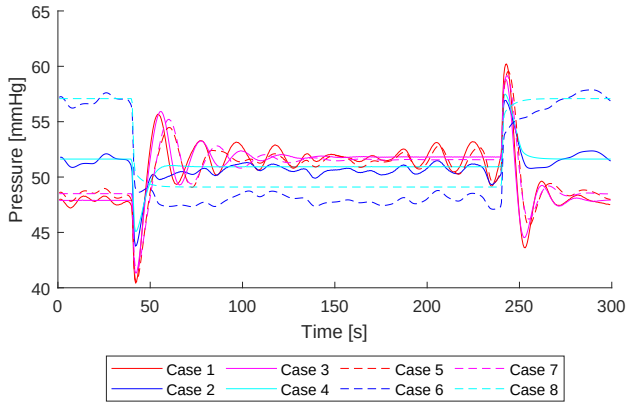

(d) Arterial Blood Pressure.

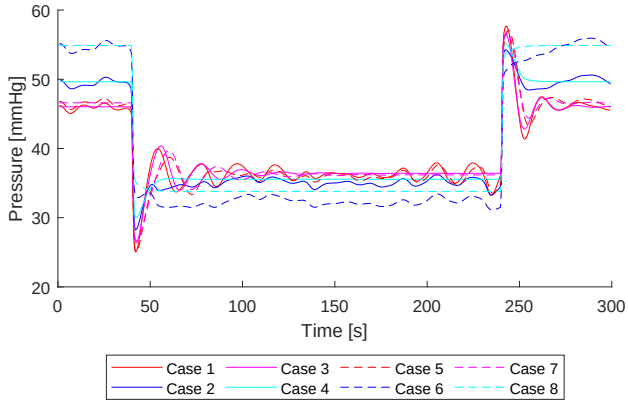

(e) Cerebral Blood Pressure.

Case #	1	2	3	4	5	6	7	8
Cerebral regulation	+	+	−	−	+	+	−	−
Peripheral regulation	+	−	+	−	+	−	+	−
HR regulation	+	+	+	+	−	−	−	−

Figure A.2: Simulation of Ida. The table describes which regulatory mechanisms that are activate in each case.

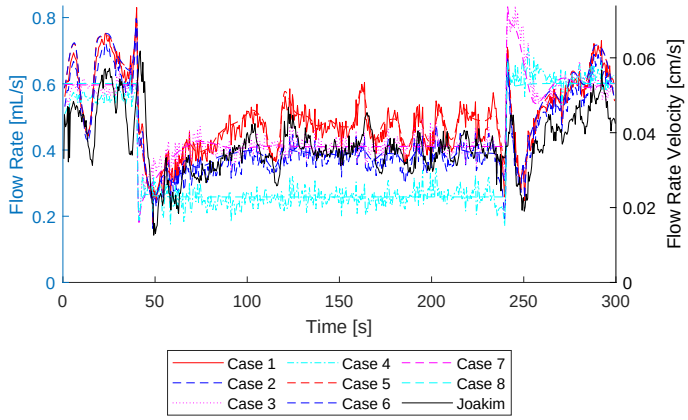

(a) Flow rate and flow velocity (black).

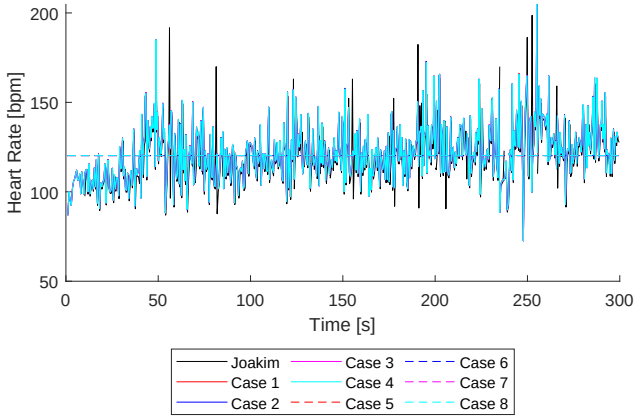

(b) Heart rate.

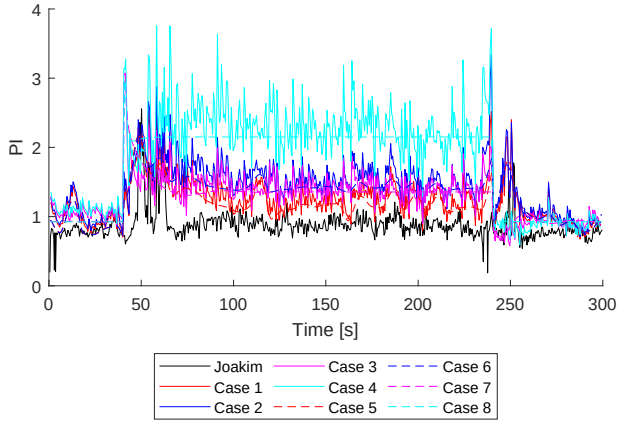

(c) Pulsatility Index (PI).

Figure A.3: Simulation of Joakim using heart rate as input (cont. on next page).

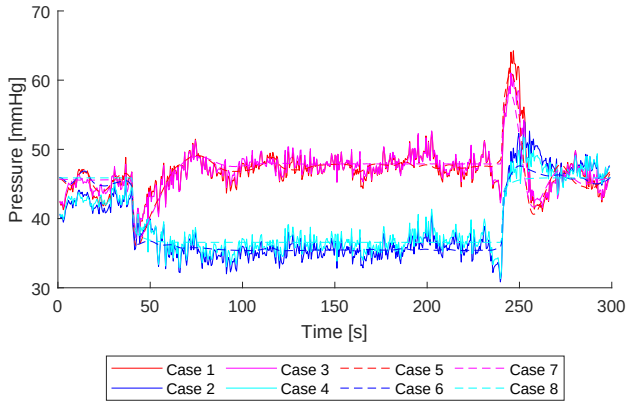

(d) Arterial Blood Pressure.

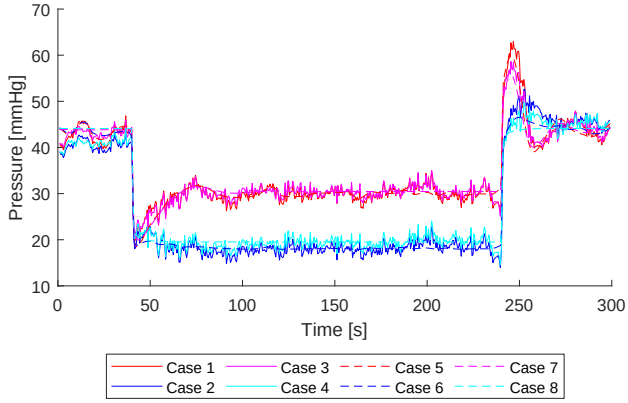

(e) Cerebral Blood Pressure.

Case #	1	2	3	4	5	6	7	8
Cerebral regulation	+	+	−	−	+	+	−	−
Peripheral regulation	+	−	+	−	+	−	+	−
HR regulation	+	+	+	+	−	−	−	−

Figure A.3: Simulation of Joakim using heart rate as input. The table describes which regulatory mechanisms that are activate in each case.

Appendix B

Source Code

B.1 Generation of Input

```
1  function [y, HR_out, t_start_out, t_out] = fcn(mP, t, HRin,
       HR0, mp0, t_start_in, t_in, regBool, bw)
2
3  % This function creates an input signal to the model.
4  % Heart rate is kept constant the first 20 seconds of the
       simulation to ensure that the model reaches steady-state
       .
5  % A new heart rate is only calculated when the previous
       cardiac cycle is finished.
6  %
7  %
8  %
9  % Inputs:
10 % mP          - measured pressure
11 % t           - current simulation time
12 % HRin        - current heart rate
13 % HR0         - baseline heart rate
14 % mp0         - reference pressure
15 % t_start_in - the time of the beginning of the current
       cardiac cycle
16 % t_in        - the time of the previous calculation
17 % regBool     - 0/1 depending on whether the heart rate
       should be dynamic or kept constant (boolean constant)
18 % bw          - body weight (constant)
19 %
20 %
21 % Outputs:
```

```
% y              - flow output q(t)
% HR_out         - new heart rate
% t_start_out    - the time of the beginning of the current
    cardiac cycle
% t_out          - the time of calculated output
%
```

```
maxHR = 200; % maximal HR
minHR = 100; % minimal HR
t_out = t;

if t < 20 || ~regBool
    HR = HR0;
else
    HR = HRin;
end

t_corr = t - t_start_in;

if t_corr < 60/HR
    t_start_out = t_start_in;
else
    t_corr = t_corr - 60/HR;
    t_start_out = t - t_corr;
    v = 5;
    delta = mP/mp0;
    ns = 1/(1+delta^v);
    np = 1/(1+delta^-v);
    tau = 10; alpha = 1.75; beta = -0.25; % tau = 3;
    dt = t-t_in;
    oHR = HR/HR0;
    nHR = oHR + (60/HR)*(alpha*ns-beta*np-oHR)/tau;
    if t > 20 && regBool
        HR = HR0 * nHR;
    end
end

if HR > maxHR
    HR = maxHR;
elseif HR < minHR
```

```
    HR = minHR;
end

t_c = 60/HR;
t_s = (286 - 0.80*HR)/1000;
a = 1/6;
sv = (-0.02*HR+7.11)* 1.77*(bw/1000)/ (-0.02*120+7.11);
sc = sv*pi/(2*(1-a^2)*t_s);
if t_corr < t_s
    y = sc*sin((pi/t_s)*t_corr);
elseif t_corr < (t_s + t_s*a)
    y = -sc*(a/cos(pi/a))*sin((pi/(a*t_s))*t_corr);
else
    y = 0;
end
HR_out = HR;
end
```

B.2 Regulation of Peripheral Resistance

```
function y = fcn(xmax, xmin, t, dt, x, k, tau, p0, p, r0)

% This function sets the peripheral resistance for one
   compartment.
% Resistance is kept constant the first 20 seconds of the
   simulation to ensure that the model reaches steady-state
   .
%
%
% Inputs:
% xmax - maximal resistance
% xmin - minimum resistance
% t    - simulation time
% dt   - time since the existing resistance was calculated
% x    - existing resistance
% k    - steepness/sensitivity constant
% tau  - time constant
% p0   - reference pressure
% p    - measured pressure
% r0   - baseline resistance
%
%
% Outputs:
% y - new resistance
```

```
22 %
23
24 if t > 20
25     xctr = (xmax - xmin)* p0^k / (p^k + p0^k) + xmin;
26     dx = (-x + xctr)/tau;
27     y = x + dx*dt;
28 else
29     y = r0;
30 end
31 end
```

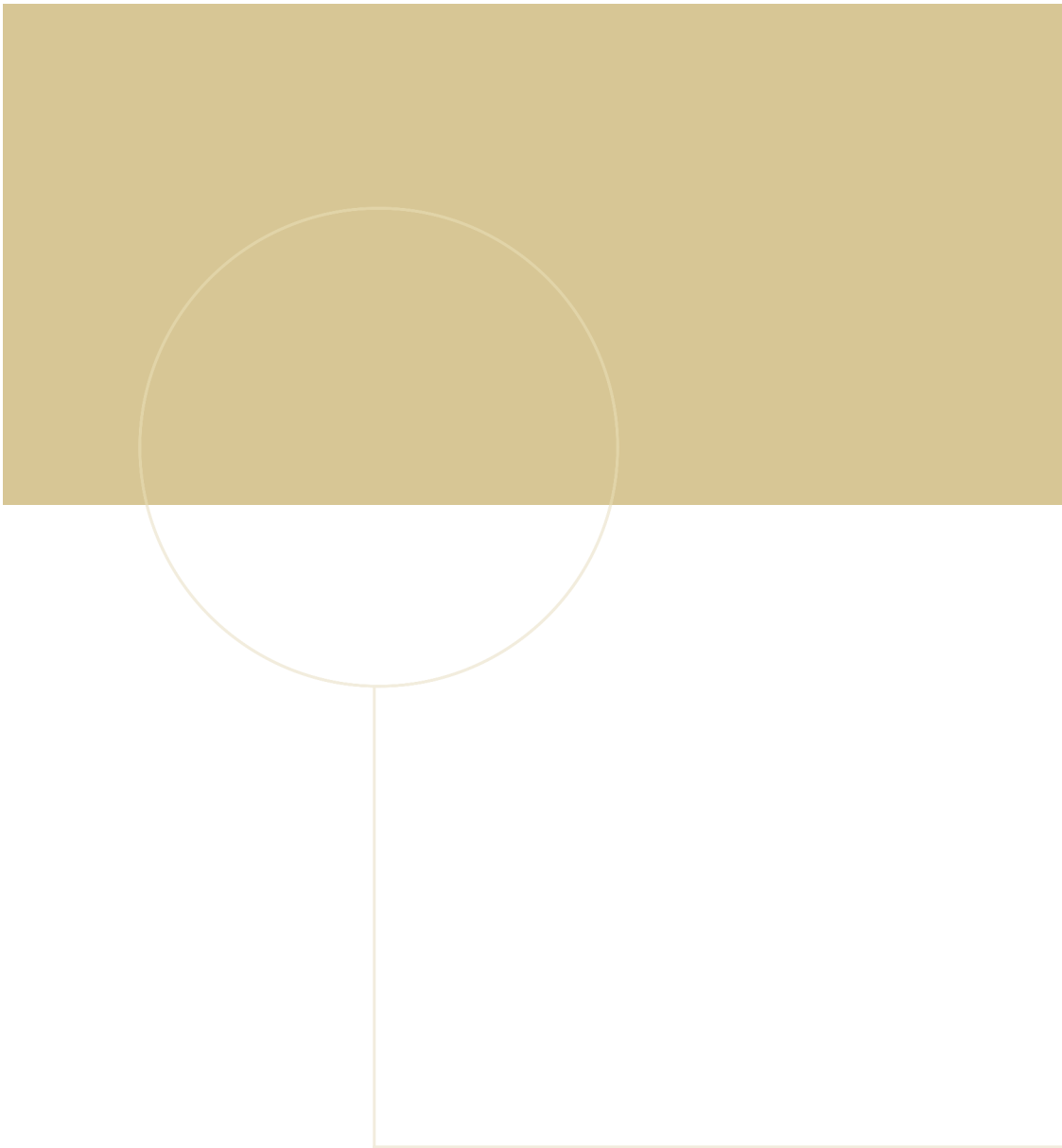

NTNU
Norwegian University of
Science and Technology